Growth and Characterization of Diamonds for Use in High Pressure Sensing

Michael Tokiyoshi Hamel

A thesis submitted in partial fulfillment of the
requirements for the Master's degree in Physics

Department of Physics
Faculty of Science
University of Ottawa

Abstract

Diamond possesses unique physical properties which give it great potential as a solid state framework for quantum sensors. Despite a worldwide research and development effort, the primary factors limiting its wider implementation are the technical difficulties related to high quality synthesis and device manufacture. In this work, as a first objective, laboratory diamond synthesis is explored with the aim to achieve single crystal diamond of high quality. A suite of characterization methods is implemented to evaluate and understand the physical qualities of synthesized diamond. Through a measurement process, a procedure for improving diamond growth is presented. As a secondary objective, a diamond-based defect which can be functionalized as a quantum sensor is investigated. The negatively charged silicon vacancy defect (SiV^-) in diamond is explored for its potential use as a quantum high pressure/low temperature sensor. This SiV^- defect is optically accessible by photoluminescence. This optical emission arising from the SiV^- defect is studied under high pressures (up to 17 GPa) and low temperatures (down to 11 K). More specifically, the emission corresponding to SiV^- zero phonon line and local vibrational mode and their respective change as a function of pressure and temperature are recorded. This work indicates a promising potential for the SiV^- defect as a useful quantum sensor, especially in the context of extreme conditions research.

Acknowledgements

I want to deeply thank those who have helped me through my years at the University of Ottawa. It is said we stand on the shoulders of giants and I feel that more profoundly over time. The bibliography at the end of the thesis recognizes some of the scientific giants who aided me through the degree and here at the beginning are my personal giants.

Serge Desgreniers - A tireless mentor and a true inspiration.

Amy Kuang - My joy and spirit.

My parents - Ever supportive, ever caring.
Ronan - My best friend and deepest ally.

Spencer Sterling - A good friend in the lab and a great sounding board.

Those who took part in CIN 336 - For their excellent (pixelated) company and taste in movies.

Those who kept society afloat - Somehow still under-appreciated.

I would also like to thank Benoit Denis, whose help with the experimental work laid the foundation for the low temperature, high pressure study.
I am also grateful to NeoCoat SA for their assistance in optimizing the growth and operating the reactor. Specifically, I would like to thank Benoit Baudrillart and David Rats whose assistance were essential for this work.
It is also important to acknowledge the shared laboratory space and those who work in them, specifically CRPuO, NMR and NanoFab at the University of Ottawa. In particular, I would like to thank Professor Adina Luican-Mayer who provided me access to the NanoFab facilities.

Contents

List of Figures

List of Tables

Abbreviations

BI	Birefringence Imaging
CVD	Chemical Vapour Deposition
DAC	Diamond Anvil Cell
EDF	Extended Depth of Field
EPR	Electron Paramagnetic Resonance
FTIR	Fourier Transform Infrared Spectroscopy
FWHM	Full Width at Half Maximum
GPa	GigaPascal
HPHT	High-Pressure, High-Temperature
IR	Infrared
LPSD	Laboratoire de physique des solides denses
LT	Low Temperature
LVM	Local Vibrational Mode
MWCVD	Microwave-enhanced Chemical Vapour Deposition
NV	Nitrogen Vacancy
ODMR	Optically Detected Magnetic Resonance
OES	Optical Emission Spectroscopy
PCD	Polycrystalline Diamond
PCD-α	Thin polycrystalline sample, see Appendix A
PCD-β	Thick PCD sample, see Appendix A
PCD-$S1$	Thin PCD, heavily Si doped, see Appendix A
PCD-$S2$	Thin PCD, lightly Si doped, see Appendix A
PID	Proportional–Integral–Derivative
PL	Photoluminescence
ppb	parts per billion
ppm	parts per million
PSB	Phonon Side Band
PTM	Pressure Transmitting Medium

RS	Raman Spectroscopy
RT	Room Temperature
SCD	Single Crystal Diamond
SCD-α	High Quality CVD sample, see Chapter 3
SCD-β	High Quality CVD sample, see Chapter 3
SEM	Scanning Electron Microscopy
SiV	Silicon Vacancy
SNR	Signal to Noise Ratio
ZPL	Zero Phonon Line

Chapter 1

General Background

1.1 Motivation

Diamond is an undeniably remarkable material. The jewellery industry has forged its mythos, with its story based upon a set of truly extraordinary properties. Concepts of eternity, brilliance, and purity can be linked back to physical properties: "eternity" from its inability to be damaged (as it has the highest hardness of any material); "brilliance/sparkle" due to a high index of refraction; and "purity/clarity" from its remarkable optical transparency (ultraviolet, infrared, visible, and RF transparency, with absorption only from 2–7 μm). While these physical properties are interesting, they only scratch the surface of the extreme physical characteristics that diamond inherently possesses.

To those who work with materials under extreme conditions, diamond has always been a useful tool to push other materials to their extremes. Specifically, diamond's yield strength, highest of any natural material, is used to pressurize samples to conditions that are six orders of magnitude (>100 GPa) above those found on the crust of Earth. Additionally, the chemical inertness of diamond means that it generally does not react with the samples under study, while the optical transparency allows for diamonds to act as ideal windows throughout the experiment.

While extreme conditions research has used diamond for nearly 60 years, it has not been utilized in many other scientific endeavours. Within the past decade, this fact has rapidly been changing. One driving force of this shift is the improvement in synthetic growth methods, specifically the progress in microwave plasma-enhanced chemical vapour deposition (MWCVD/PECVD) which allows for the production of suitable diamond samples.

Synthetic diamond manufacture, however, is not a novel concept as High Pressure, High Temperature (HPHT) and detonation synthesis methods have been commercially creating man-made diamonds since 1954 [1] and 1963 [2], respectively. The major progress, therefore, comes from the improvement in purity which can be achieved with Chemical Vapour Deposition (CVD) growth as compared to other methods. Diamonds used as modern scientific tools often require ultra-high purities below 1 part per million (ppm). These can be commercially designated as "quantum" (<50 parts per billion (ppb) [3]) or "electronic" (<5 ppb [4]) grade.

From the world's recent history with silicon as a basis for modern microelectronics, it can be understood that controlled doping of an ultra-high-purity semiconductor (of which diamond can be considered) can lead to highly interesting device design. As diamond has nearly ideal electrical properties (Table 1.1 - See [5] for further discussion), using it as a substrate has been a topic of

Property	**Value**	**Comparison**	**Note**
Hardness (Mohs)	10	9 (Al_2O_3) [11]	Defining material
Yield Strength (GPa)	130-140 [12]	21 (cubic SiC) [13]	Highest yield strength (bulk)
Optical Transparency range (nm)	>225 [14]	150-5500 (Al_2O_3)	Weak absorption between 2 - 7μm
Refractive Index	2.4 [15]	2.6-2.75 (SiC) [16]	Second-highest index of refraction
Thermal Conductivity ($\frac{W}{cm \cdot K}$)	24 [5]	3.86 [17] (copper)	Highest thermal conductivity
Bandgap (eV)	5.47 [5]	3.44 (GaN)	Ultra-wide allows High Temps
Breakdown Field ($\frac{MV}{cm}$)	10 [5]	5 (GaN)	High voltage
Carrier Mobility ($\frac{cm^2}{Vs}$)	4500 [5]	1450 (Si)	Highest of any semiconductor

Table 1.1: List of extreme properties that diamond possesses, which can be useful in various fields

interest for many researchers. Due to difficulties in doping effectiveness and physical fabrication, these efforts are still in an exploration phase, however, it has been found that by deviating from the typical semiconductor doping paradigm and instead using specialized dopants as quantum systems, easy pathways for the development of quantum technologies can be found.

The "star" of these quantum dopants in diamond is the NV^- centre, allowing access to a quantum system with only common laboratory tools (*i.e.*, 532 nm laser, photodiode and microwave antennas) and without the need for cryogenic systems. The technology has found significant successes in a short period of time (initial publications start in 2008 [6]) and has led to multiple high-profile achievements in quantum communication [7], sensing [8], and information processing. The technology has also achieved enough success that it expected to move outside of the research laboratory environment soon. This is as evidenced by its significant inclusion in the Institute of Electrical and Electronics Engineers' plan for the future 15 years of electronics devices [9, 10].

For these reasons, we are interested in further exploring lab-grown high quality diamonds for sensing applications, tailored to the study of materials at extreme conditions which is the field of research of my group, the Laboratoire de physique des solides denses (LPSD) at the University of Ottawa. Additionally, it allows us to better understand these intriguing and useful quantum systems, specifically their behaviour under extreme pressure and temperature conditions.

1.1.1 Extreme Conditions Research

The thermodynamic conditions we experience on the surface of Earth are highly abnormal within the universe, nonetheless under these particular conditions, a vast array of remarkable phenomena allow for life as we know it to exist. Shifting into another zone of pressure/temperature, the elements we know become remarkably different. For instance, hydrogen becomes metallic [18], water shifts phase 19 times [19] and some materials become superconducting, even near room temperatures ($\sim$ 15 °C) [20].

In order to explore this vastness of the universe's conditions and search for materials with 'extreme' properties, scientists have relied extensively on creating high pressures using a device called the Diamond Anvil Cell (DAC). It achieves ultrahigh compression by squeezing a sample between two diamond anvils (Figure 1.1). As the pressure is inversely proportional to the sample's area, small samples can be studied at pressures in excess of hundreds of GPa (six orders of magnitude above atmospheric pressure).

As this technique requires the sample to be essentially enclosed between two diamond anvils,

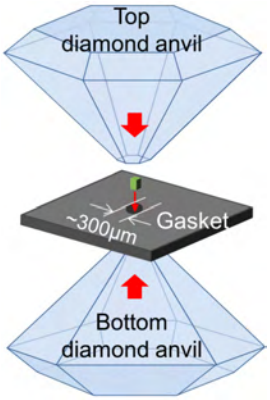

Figure 1.1: Typical diamond anvil cell, which works through compressing the sample on the diamond anvil's small faces. The sample is shown in green, while the gasket is grey. Adapted from [21] with permission.

the measurements and interaction with the samples are generally completed optically. This has proved to be successful, but it inherently makes certain properties difficult to witness. For example, superconductivity is a property best determined through electrical resistivity or magnetic susceptibility measurements which represent a genuine challenge to the experimentalist.

1.1.2 Nitrogen Vacancy NV^-

One promising possibility for sensing in extreme conditions research is to functionalize the diamond anvils. Recent efforts have focused upon utilizing a defect system known as the negative nitrogen vacancy (NV^-), as its spin system is sensitive to several properties and can be accurately initialized and read out. These properties make the spin system stand out as a high-quality candidate for sensing.

This defect comprises a single substitutional nitrogen atom adjacent to a vacant lattice site (Figure 1.2a), which is negatively charged. This defect has gained significant interest in the scientific community as the defect has a spin-dependent photoluminescence signal, which allows significant contrast (30%) [22] between states, with long lifetimes (ms) [6] at room temperature. The fluorescent signal is also observed conveniently at a wavelength of 637 nm, allowing excitation and detection with commonly available laboratory equipment.

It is also important to note that since the nitrogen and vacancy are both replacing one carbon, the defect itself will be aligned along the bond to one of the four $\langle 111 \rangle$ crystallographic directions. This is illustrated in Figure 1.2a. The defect's spin energy levels are sensitive to magnetic fields, electric fields, stress, and temperature changes [23].

Naturally, the defect will be in a spin zero state, but can be excited into a spin ± 1 state. The photoluminescence is spin dependent and therefore the defect's spin state can be determined by monitoring its emission at 637 nm.

The scheme of Optically Detected Magnetic Resonance (ODMR) utilizes these properties by scanning through the excitation frequencies with microwaves around 2.87 GHz, and monitoring the photoluminescence signal concurrently. This allows determination of the microwave resonance frequency with an uncomplicated laboratory setup.

The interaction of the spins with the external environment allows for splitting to be resolved and optical sensing of the previously mentioned properties. Importantly, both magnitude and direction of the field can be resolved.

As the spin state of the NV^- centre is long-lived and easily controllable and measurable through

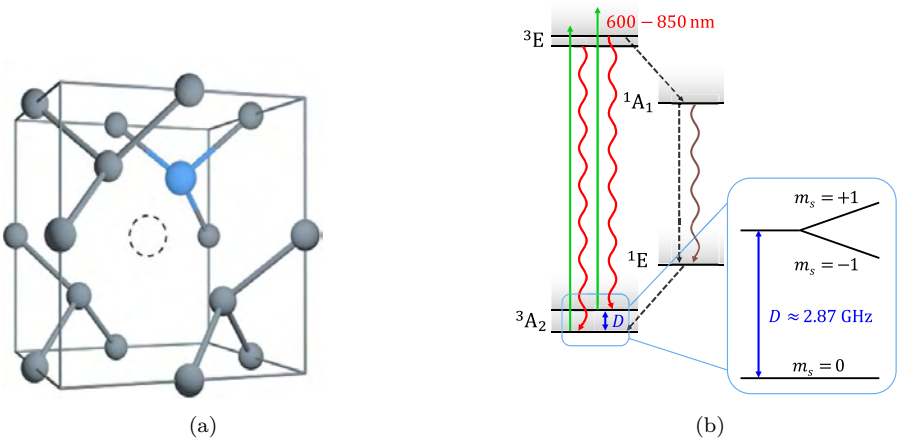

(a) (b)

Figure 1.2: The NV defect, shown in both in terms of physical makeup and electronic levels. a) Structure of the NV defect in the diamond lattice. Blue represents nitrogen, grey the native carbon, and the dotted outline represents a vacancy. Reproduced with permission from Ashfold *et al.* [22]. Copyright 2020 American Chemical Society. b) Level diagram of the negative NV^- centre, inset with the zero field split, and the Zeeman shift. Reproduced from Barry *et al.* [6] with permission.

an all-optical scheme, it can serve as an easily accessible qubit. Additionally, individual NV^- spins are able easily interface with other nearby spins. This has lead to significant successes, especially in the area of quantum communications [7].

As diamonds are often used in extreme conditions research, where the determination of novel properties require accurate metrology, the development and application of NV^- sensors are a natural fit and it is not surprising that this field has shown an accelerating growth. Experimental protocols using NV^- have enabled pressure measurements [23], along with measurements of the magnetic field and stress at unprecedented sensitivities [24, 25]. These experiments are either accomplished with an ensemble of defects embedded in the surface of the diamond [26] or using diamond particles mixed into the sample [27].

Unfortunately, since the photoluminescence of the NV^- centres blueshifts with pressure, the typical excitation with a 532 nm laser can only enable measurements up to 60 GPa [23]. While this limitation is surmountable, to our knowledge the NV^- centre has not been studied past that pressure limit.

1.1.3 Silicon Vacancy (SiV) Defect

The usefulness of the NV^- centre in sensing and communication has created interest in other suitable defects in diamond. Despite the successes described, NV^- centres also show inherent limitations, specifically due to their non-ideal optical properties. The first of these deficiencies is the significant intensity of the phonon side band, meaning a minimal number of photons will be emitted at the sharp, main peak known as the Zero Phonon Line (ZPL). The second deficiency is the large spectral diffusion, caused by a sensitivity to local environment. This sensitivity causes significant issues in extreme conditions research, where the peak can be over broadened and 'washed out' with the application of high pressures.

Other defects which occur within diamond have thus been explored. The silicon divacancy

defect (SiV) has been the leading alternative, as it inherently has the ideal optical properties (narrow linewidth, high conversion efficiency, low spectral diffusion and insensitivity to proximate charges) which the NV^- centre lacks. On the other hand, it lacks some other useful properties which the NV^- centre has, such as the simple two-level system and the long coherence times at room temperature. Over the past several years, the SiV defect system has emerged as a field of intensive research. A thorough discussion of its properties and uses will be found in chapter 4.

1.2 Types of Diamond

There are three major methods of diamond creation: Natural; High-Pressure, High-Temperature (HPHT) synthesis; and chemical vapour deposition (CVD).

Regardless of their creation method, diamonds are classified into "types". This grading scheme was originally created to segment natural diamonds and is primarily based upon nitrogen defects, as nitrogen is easily incorporated into the diamond lattice and serves as its most common defect. One classification references boron (IIb), which is uncommonly incorporated into natural diamond.

The classifications are shown in Figure 1.3, and are relatively simple: segmenting the high (Type II) and low quality (Type I) diamonds based upon their nitrogen quantity; and then subdividing these groups based upon which types of nitrogen defects are most common. These common defects are N_4V^0(A), N_4V^0(B), and N_s(C). They are explored in section 3.3.

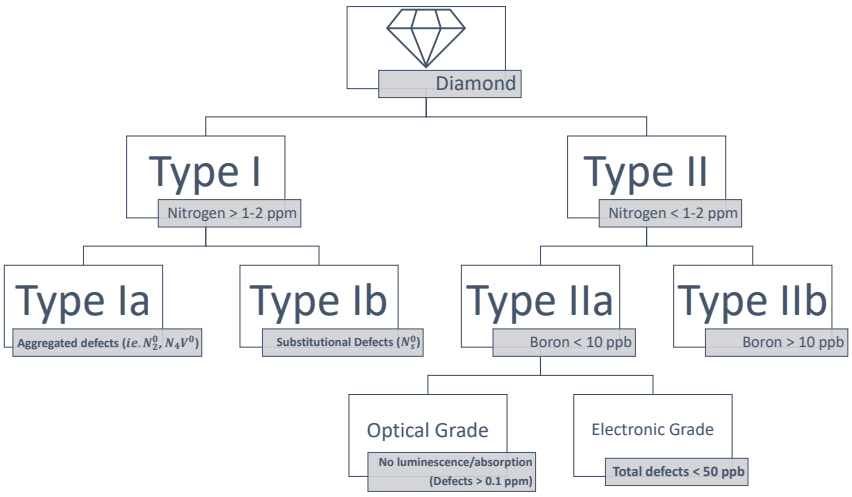

Figure 1.3: Classification hierarchy of the different diamonds types — based on defect nature and quantity. The defects are referenced and described in section 3.3. Note: One can also add a letter to indicate the method of synthetic creation: 's' indicates HPHT while 'c' indicates CVD.

1.2.1 Natural

The natural category of diamonds is diverse due to the wide variety of geological conditions the diamond can undergo during creation. Since diamonds are created at higher temperatures and higher pressures than any other method, the defects become mobile and tend to aggregate. Therefore, single substitutional nitrogen is uncommon, while the N_4V^0 (B) defect (aggregate of four nitrogen atoms) is very common.

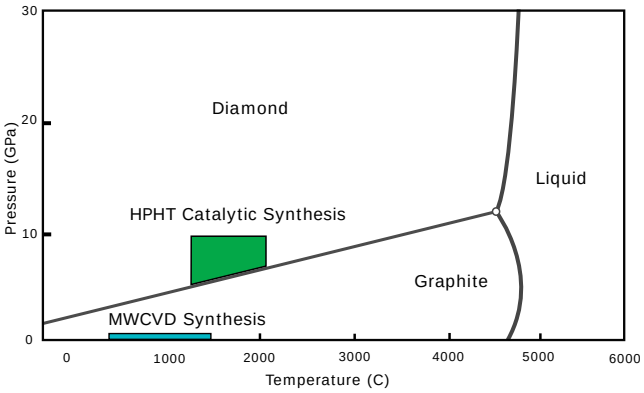

(a)

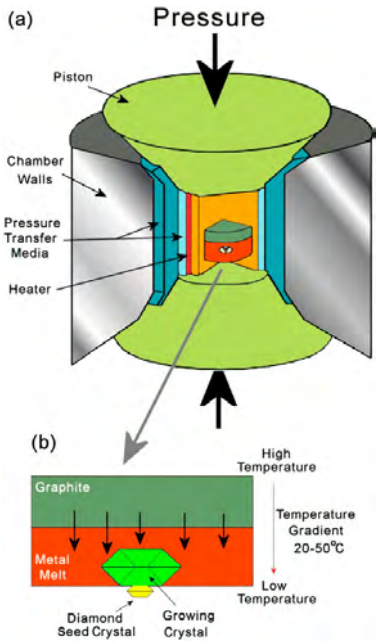

(b)

Figure 1.4: a) Phase diagram of carbon and the differing conditions used to synthesize diamond. b) Schematic diagram of the HPHT press. Diagram reproduced with permission from Ashfold *et al.* [22]. Copyright 2020 American Chemical Society.

1.2.2 High Pressure, High Temperature (HPHT)

The task of creating diamonds on the surface of the Earth rather than hundreds of kilometres below the crust is no simple matter. The first synthetic technique developed nearly 70 years ago [1] is now known as the High Pressure, High Temperature (HPHT) method. This method attempts to recreate conditions found under the earth in order to transform graphite into diamond, employing a device similar to a large diamond anvil cell (Figure 1.4b).

For technical reasons, synthesis tends to operate at lower pressures and temperatures than would be practical for natural growth, this can be seen in Figure 1.4a. However, it is possible to accelerate the natural process using two major techniques: the first is the use of seeds, which are small diamonds that act as nucleation points for the transformed graphite; the second is the introduction of a metal solvent/catalyst which can lower the temperatures needed and promote growth. These two techniques are shown in Figure 1.4b.

Graphite is melted into the metal mixture, which then crystallizes onto the diamond seed through use of temperature gradients (typically), allowing for the formation of the desired crystalline phase. This means that the growth is formed by building up layers which inevitably leads to residual stresses, although the magnitude of these stresses depends on the growth rate. Early in development, HPHT diamonds were coloured due to large concentrations of dopants. More recently, colourless crystals with low defect concentrations have been created. [22]

1.2.3 Chemical Vapour Deposition (CVD)

The newest method of diamond synthesis is known as Chemical Vapour Deposition (CVD), it is now the preferred method to create large and high-quality diamonds. In modern research/industry settings, the microwave plasma (or plasma-enhanced) growth technique has gained prominence due

to its ability to produce high quality diamond at a relatively high growth rate. This work will focus solely upon this Microwave-enhanced Chemical Vapour Deposition (MWCVD) process, a schematic of this process is shown in Figure 1.5.

The technique itself relies on the use of a high-purity and carbon-rich gas (typically methane, CH_4) along with a gas that will etch away the non-diamond carbon deposition. The etching gas is typically hydrogen, as it contributes significantly to the process of creating diamond precursors. In the CVD process, diamond is formed layer by layer onto the substrate through epitaxial growth and the control of synthesis parameters can be optimized in order to achieve high growth rates [28] or high-purity samples [29].

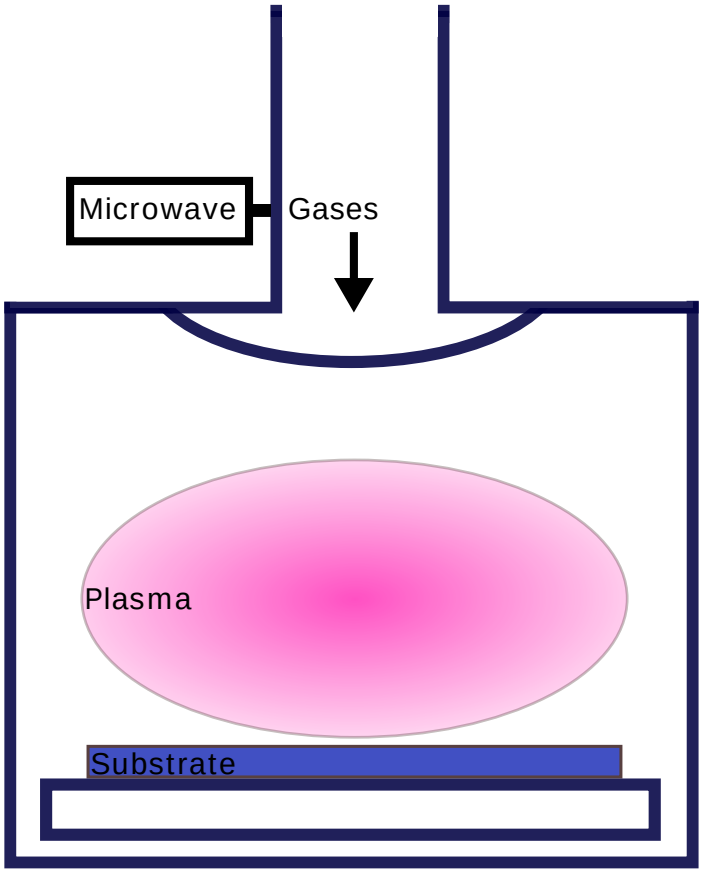

Figure 1.5: Simplified schematic of the MWCVD reactor used in this work. Gases and microwave radiation enter from the top of the chamber and create a plasma. This plasma interacts with the substrate to create the deposition product.

For the CVD process, the deposition conditions are much more flexible and versatile than the other synthetic fabrication methods, which has enabled novel research possibilities [30–34]. One key variable is the choice of substrate, which can result in either homoepitaxial or heteroepitaxial growth. Attaining single crystal conditions under heteroepitaxy has been largely unsuccessful, except with the use of a multilayer structure of iridium and yttria-stabilized zirconia (Ir/YSZ/Si) [35]. Therefore, for the majority of cases, it is generally accepted that heteroepitaxial growth will create only polycrystalline diamond (PCD) and homoepitaxial depositions are needed to create single-crystal diamond (SCD). The following discussions will focus on SCD conditions which result in higher quality diamond.

1.3 CVD Growth Mechanisms

The process of MWCVD typically involves the mixing of methane and hydrogen with a ratio of <5% methane and the coupling of microwave radiation with this gas mixture to create a plasma. This is typically completed at subatmospheric gas pressures (100–300 mbar) and high substrate temperatures (800-1500°C). However, referring to the carbon phase diagram (Figure 1.4a), this region should only allow for the formation of graphite. This incongruence between the phase diagram and growth conditions can be explained by chemical reactions which occur in the plasma and on the surface of the diamond seed. This section provides a general description of the current understanding of these reactions.

Hydrogen Radicals The simplest reaction which occurs in the plasma is also one of the most significant. This is the creation of hydrogen radicals through electron impact as enabled by the microwaves:

$$H_2 + e^- \longrightarrow 2\,H + e^- \tag{1.1}$$

The hydrogen radical (H) has two main functions, first as a component of many chemical reactions and second as an etching species. This etching occurs on every solid within the plasma, but it is key to note that graphite is etched at a significantly higher rate than diamond. Therefore, though both graphite and diamond are formed, graphite is preferentially etched as compared to the diamond, leading to a growth of only diamond, when conditions are tuned properly.

The initial chemical reaction between the hydrogen radical and methane is the creation of the methyl radicals:

$$H + CH_4 \longrightarrow H_2 + CH_3 \tag{1.2}$$

Multiple similar reactions with the methyl radical will produce other species (CH_x, C_2H_x) which are considered the important precursors for growth. [14].

1.3.1 Surface Dynamics

Several processes are essential for diamond growth to occur. Since the diamond surface is in a hydrogen-rich environment, the surface carbon atoms are generally hydrogen terminated. This chemical termination does not allow for the methyl groups to bind to the diamond surface (C_d−H), so an activation must occur. This will be achieved by the hydrogen radical removing the dangling hydrogen bonds in the forward reaction:

$$C_d{-}H + H \longrightarrow C_d + H_2 \tag{1.3}$$

Concurrently, active sites (C_d) are filled: $C_d + H \longrightarrow C_d - H$. These competing reactions mean that only a fraction of the possible sites are available for reaction at any given time. The surface activation rate is the primary limiting factor for growth for the "low" temperature regime ($\sim$ 1000°C). This aspect will be discussed further in section 2.2.1.

These active sites will adsorb methyl radicals ($C_d + CH_x \longrightarrow C{-}CH_x$) and the remaining hydrogen atoms are then etched off by the hydrogen radicals, making them new possible sites for growth to occur.

In broad terms, the overall diamond growth can be considered as a slow addition of carbon atoms to the existing lattice, catalyzed by atomic hydrogen. The process described here was

established by the work of Goodwin [36] and has been reaffirmed by further work in the field [37]. This work also established the importance of CH_3 as the major methyl group acting upon the growth.

1.3.2 Internal Plasma Dynamics

In-situ measurements within the plasma are difficult as any contact probes will be etched away. All-optical measurement techniques would be limited to plasma emissions and by the resolution achievable through a small quartz window placed at tens of cm away from the dense plasma region. For these reasons, there is only a limited understanding of the chemical mechanisms which enable growth.

Alternatively, further insights can be found through simulations. While the full details of possible simulations will not be discussed here, it should be mentioned that the strong coupling of thermal, chemical, electromagnetic, and transport phenomena take place during the CVD process, meaning that a complete modelling of the reactor and process can become complex. Consequently, simplified models are often used [38].

Parameter gradients lead to differing reactions occurring at different regions of the plasma. Local conditions are influenced by a multitude of factors, most of which can be altered directly or indirectly by the operator of a given reactor. These complicated interactions make it difficult to tune plasma growth parameters and has encouraged efforts in simulation to define optimal parameters. Although actual simulations were beyond the scope of the present work, it is nonetheless important to understand the main ingredients for full understanding of the CVD dynamics. Simulations usually apply to two main components: The plasma itself and the chemical reactions.

1.3.2.1 Plasma

The hydrocarbon reactions are generally simulated separately from the more general plasma reactions. Therefore, for the majority of parameters, a pure hydrogen plasma is considered. This mirrors the experimental methodology of MWCVD growth, where a pure hydrogen plasma is ignited and tuned before the methane is introduced. As the large molar fraction of the hydrogen to methane means that the hydrogen will have an outsized effect upon the plasma conditions (common ratio range is 95:5 – 98:2), it has generally been deemed as acceptable. The same simplification is also used for judging the plasma volume, as shown in section 2.4.1.1.

The plasma is mainly defined by the input microwave (frequency commonly set at 2.45 GHz) and the local geometry of the plasma. The microwave is able to couple directly with the gas, therefore a model which assumes that all power is absorbed (resistive mode) matches well with reality. The major variables which determine the properties of the plasma will be: the electron density (n_e), electric field, and the gas temperature. Each of these properties will affect the other. A quick description of each is as follows.

Electron Density (n_e) Electrons are created through the ionization of the hydrogen gas by way of electron impact ionization processes. High electron densities therefore tend to correlate with higher temperatures due to resistive heating. As the chemical processes are either chemically or electron driven, the determination of the extent of high electron density can allow us to find the area where diamond precursors occur. Experimentally, this can and will be found by measuring the spatial extent of the hydrogen plasma, typically completed by observing H_α emission [39] (see section 2.4.1.1 for further discussion).

Temperature Gas temperatures will enable different chemical processes to occur, and while related to the electron density, the temperature will vary differently. In typical conditions, the maximum temperature will occur above the region of the peak in electron density as it is less coupled to the substrate. This distribution is also notably smooth except in the near field where substrate interactions can form thin films.

Electric Field The electric field depends primarily on the microwave power, microwave impedance/tuning, and the geometry/materials it interacts with. However, as the plasma/gases heat up they gain more electrons and the permittivity and permeability will be affected. This leads to increased concentration of the field near the plasma centre, allowing more energy intensive reactions to occur in an enhanced zone.

1.3.2.2 Hydrocarbon Chemical Reactions

The chemical reactions which occur when hydrocarbons are added will depend on the plasma parameters above and will feed back into them. However, since hydrocarbon percentages are low in the plasma, the chemical reactions are typically considered to be solely dependent on the plasma conditions. This has been shown to be true at low methane concentrations, as confirmed by optical excitation spectroscopy, [38], but is a difficult statement to verify definitively due to the wide variation in reactors and the limited in-situ measurements.

While only methane is introduced into the chamber to grow diamond, two neutral species will dominate: methane (CH_4) and acetylene (C_2H_2). From these two neutral species, electron impact reactions, ion interactions, and heavy species interactions will lead to a family of hydrocarbons which exist based on local conditions.

It is generally considered that CH_3 is the major diamond precursor within the hydrocarbon family. However, its distribution in the plasma is not always simple. With higher temperature plasmas, CH_3 will often occur near the substrate boundary. In particular, it often occurs in the temperature range of 1200K to 2200K. An example of this distribution is shown in Figure 1.6, this figure shows CH_3 in the rightmost pane, and shows the strong difference in atomic concentrations throughout the plasma.

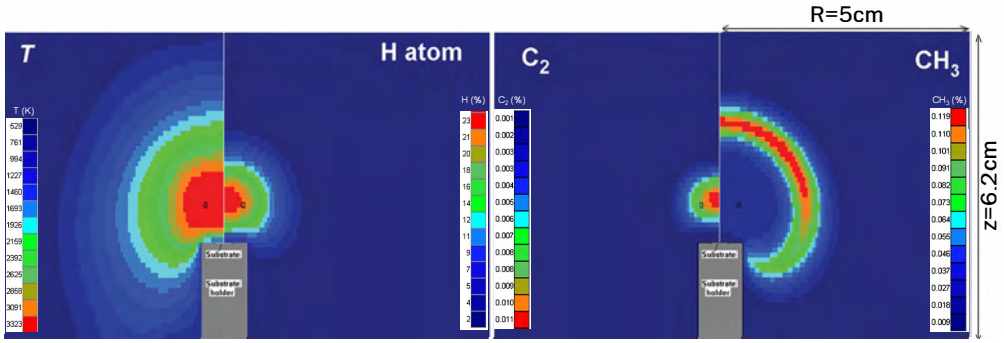

Figure 1.6: Simulation results of a single plasma, showing the differing distributions of various parameters. The plasma is focused onto a substrate embedded in a substrate holder - shown in grey. These parameters are temperature, H atoms (which maps well to n_e), C_2, and CH_3. Units of the chemical species are represented in terms of mole fraction. Adapted from Mankelevich and May [40] with permission.

The CH_3 concentration is an input into the Harris-Goodwin model [36, 41] often used for modelling diamond growth. While simple, the model has shown great usefulness in predicting the

operating conditions of diamond growth as will be seen in Figure 2.4. However, precise tuning, especially with regard to specialized reactor geometry, should be aided by precise simulation work [38].

1.4 Objectives

With the general principles of MWCVD for diamond growth described, we will now define the two major goals of the project:

- High quality diamond growth and characterization
- Study of the SiV^- defect under extreme conditions

As this work is the first in our group to explore diamond as a substrate, the initial objective is to fabricate high quality diamond in accordance with the literature. This thesis will first explore the known adjustable plasma parameters in chapter 2. Chapter 2 then proceeds to describe the suite of characterization methodologies developed to determine quality of grown diamond in section 3.2 and a particular high quality growth is described in greater detail in chapter 3.

The second aim, distinct from the first, is to study the Silicon Vacancy (SiV) defect under extreme conditions. This research utilizes our growth, thin film samples (appendix A) to study the defect under high pressures and low temperatures, as presented in chapter 4. This study allows exploration of the defect and its possible use as a sensor for extreme conditions research.

Chapter 2

Chemical Vapour Deposition for Diamond Growth

2.1 CVD Growth Morphologies

Since the 1950s, diamond has been grown through the use of the chemical vapour deposition technique and, in 1983 [42], microwave plasma-enhanced methods were pioneered. In the following two decades, many avenues were explored, but by the mid 2000s a range of suitable parameters was identified to allow high-quality growth at reasonably high rates [29, 43, 44]. These high quality growths inspired many groups to further explore the parameter space, resulting in many novel techniques to optimize the growth. Progress has been rapid and impressive [33, 45, 46].

However, before we can consider the optimization of growth parameters, we must review how diamond grows, either in its bulk form or epitaxially.

2.1.1 Crystalline Growth Morphologies

The different crystallographic faces of diamond will grow at different rates depending on conditions used. This means that there are a limited number of crystal growth morphologies which can exist. Modelling this is known as geometric modelling and was first introduced by Wild *et al.* [47] and further expanded by Silva *et al.* [48], with a complete model of the competing crystallographic {100} {111} {110} {113} faces. Note: {} brackets will note the family of planes, while ⟨⟩ will note the family of directions which would grow upon that plane.

Modelling allows for a projection of future growth morphologies, as each parameter affects the final bulk morphology. To achieve this objective, Silva *et al.* [49] define three growth-related parameters:

$$\alpha = \sqrt{3}\frac{V_{\{100\}}}{V_{\{111\}}} \qquad \beta = \sqrt{2}\frac{V_{\{100\}}}{V_{\{110\}}} \qquad \gamma = \sqrt{11}\frac{V_{\{100\}}}{V_{\{113\}}} \tag{2.1}$$

These represent the relative growth rate of planes ($V_{\{XXX\}}$). These parameters prove useful in qualifying the way each of the growth parameters will eventually affect the final morphology. Rates are scaled to that of the {100} plane. Specifically, scaling constants are the sum of squares of the Miller indices of the respective planes.

Note that if one face grows significantly faster than another it will prohibit its growth, meaning that the existence of faces will depend on these rates, specifically the slowest. This leads to parameters with convenient values for each crystal face's 'existential' limit. (Some important

Known Event	Condition	Note
{111} faces appear	$\boldsymbol{\alpha > 1}$	{111} faces are defect prone [47]
{110} faces appear	$\boldsymbol{\beta > 1}$	
{113} faces appear	$\boldsymbol{\gamma > \frac{11\alpha}{3+2\alpha}}$	
{113} overtakes {111}	$\boldsymbol{\gamma > \frac{11}{5}\alpha}$	
Twinning occurs	$\boldsymbol{1 < \alpha < 1.5}^{\dagger}$	Pyramidal surface morphology [47, 51]

Table 2.1: **Common $\boldsymbol{\alpha}$, $\boldsymbol{\beta}$, and $\boldsymbol{\gamma}$ limits** [49]. Note that the appearance of any face is considered 'undesirable' (assuming a preference for {100} growth). This list is specific to common CVD related boundaries. For an exhaustive list of all 22 geometric boundaries, see the work of Silva *et al.* [48].
† Some early reports state this region is bounded by 2 on the upper limit, but this is debated. [48, 50].

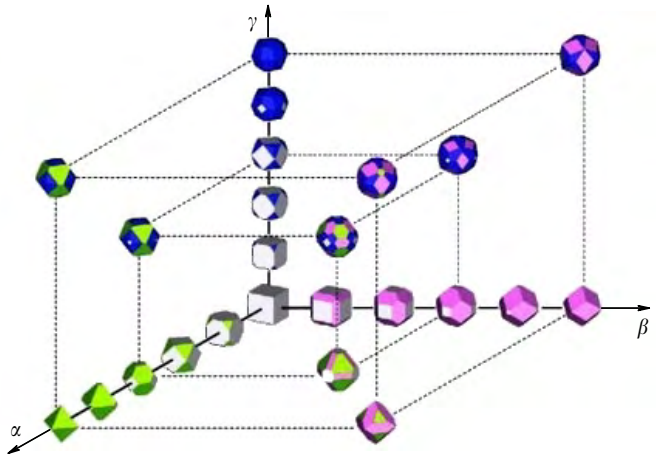

(a) Qualitative diagram showing the evolution of various equilibrium shapes relative to the α, β, and γ parameters. The diagram reproduced from [52], but is adapted from the work of [48]. Permission from both publishers was given.

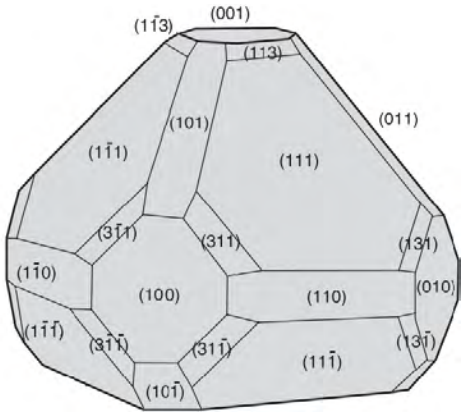

(b) A diagram for reference, which notes the various crystallographic planes important for diamond growth. Adapted from Maes *et al.* [53] with permission

.

Figure 2.1

events are shown in Table 2.1.) The slowest crystal plane tends to dominate the final morphology (as the orthogonal faces will grow, enlarging the slow face). These final morphologies are shown in Figure 2.1a where the increase of the $\boldsymbol{\alpha}$, $\boldsymbol{\beta}$, and $\boldsymbol{\gamma}$ parameter dictate the final size of each face. The combination of these variables and associated limiting values lead to a non-trivial variable space, with 55 unique growth modalities [49], although within the range of a typical reactor only a subset of these modalities are expected to occur.

These parameters are also linked to various effects in the surface morphology and can therefore influence the quality of the resultant diamonds. Throughout this work, these parameters were measured and were used to understand and optimize the growth - see [37] for further discussion. Table 2.1 also gives the effect that adjusting plasma conditions have upon the growth parameters, while table 2.3 gives high quality growths found in literature with their parameter values, this was used as a starting point for understanding typical ranges for input and growth parameters.

	α	β	γ
Temperature [37, 50, 51]	↓	↓	↓
Methane percentage [37, 50, 54]	↑	↑	↑
Pressure [51]	—	—	×
Nitrogen presence [54]	↑	↑	?
Projection [51]	—	↑	×
Pocket width [55]	×	↓	×
Pocket depth [55]	×	↑	×

Table 2.2: Effect of the change of plasma conditions on the growth parameters. ↑, ↓, and — indicates increase, decrease, and no change, respectively. ? represents an inconsistent relationship and × represents an unmeasured quantity.

2.1.2 Surface Morphologies

The model described by Silva *et al.* [49] defines bulk growth modalities, which lead to important insights. However, this crystallographic view of growth neglects the consideration of surface dynamics. In this section, we will consider how these dynamics play out by specifically looking at several types of common undesirable growths. These modes are illustrated in Figure 2.2.

2.1.2.1 Pyramidal/Hillock Growth Modes

This defect is common for many lower-quality growths and visually appears to be a pyramid as seen in Figure 2.2a. This geometrically recognizable defect is common for the {100} and {111} growth surfaces. This shape is caused by other crystallographic faces growing at higher rates than the side of interest, specifically growing in the ⟨110⟩ directions for growths upon the {100} planes.

These pyramidal hillocks emerge from a nucleation point, specifically through a twinning defect [14], where the twinned growth rate is higher than the surrounding area. This allows for the formation of an atomically small pyramid shaped hillock if $\beta > 1$, as the {110} faces will dominate and create the hillock. Alternatively, if $\beta < 1$ an 'overgrowth' will occur, where the diamond will laterally grow over the defect and inhibit it completely.

The zone of enhanced twin formation corresponds with an α parameter which is between 1.0-1.5. [37]. This was originally found by Wild *et al.* [47] to be 1.0-2.0.

Therefore, the goal of hillock-free growth is achievable either through adjusting the β parameter to lie under 1.0 or for α to be outside 1.0 – 1.5. Unfortunately, this pyramidal hillock growth modality is typical, since these α, β ranges align with the commonly used settings.

2.1.2.2 Step/Terrance Structures

A typical mid-quality growth will lead to step/terrace growth (Figure 2.2b). These terraces are formed because of nucleations which occur upon the flat surface, which are then built up because of new growth species on the surface that diffuse until they reach the edge of the terrace. Therefore, the step edges will have a high lateral growth rate and will appear to flow across the surface. A schematic of this is shown in Figure 2.3, showing the clear difference between 'misoriented' and oriented substrates.

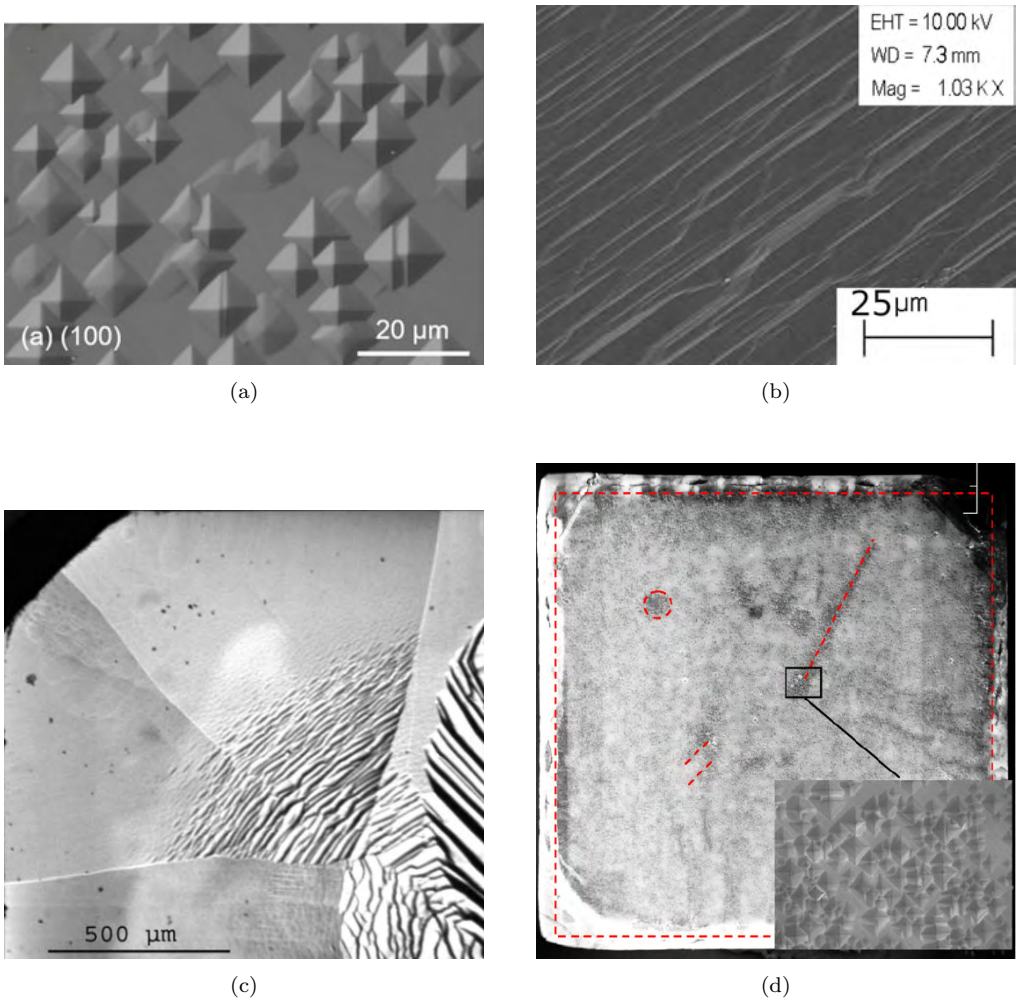

(a) (b) (c) (d)

Figure 2.2: Overview of common growth modes. a) Pyramidal Growth Mode. Reproduced from Yang [14] with permission. b) Stepwise growth mode. Sample SCD-β. c) Step bunching — stepwise growth mode, reproduced from Achard *et al.* [29] with permission. d) Etch pits. Reproduced from Silva *et al.* [37] with permission.

Step-like growth is particularly influenced by the misorientation angle, as it ideally can allow for a high number of atomically small edges, allowing flow/growth on an atomic scale. Alternatively, lowering the amount of growth species which arrive at the surface will lead to a lower number of adatoms ("adsorbed atoms" on the surface), and hence lower the possibility of nucleation on the smooth surface. [14]

Rough Surface The alternative to the occasional nucleations which create the islands of growth are common nucleations, which are randomly distributed. These will therefore form into many random islands, which in effect will create a rough surface.

2.1.2.3 Step Bunching

The macro step bunching defects (Figure 2.2c) requires stepwise growth. During the stepwise growth, if a defect obstructs the diffusion of the growth species it will stop the flow of the species. It will stop the step as well. However, the steps 'behind' it will continue to flow until it reaches

the same spot, effectively 'bunching' the steps.

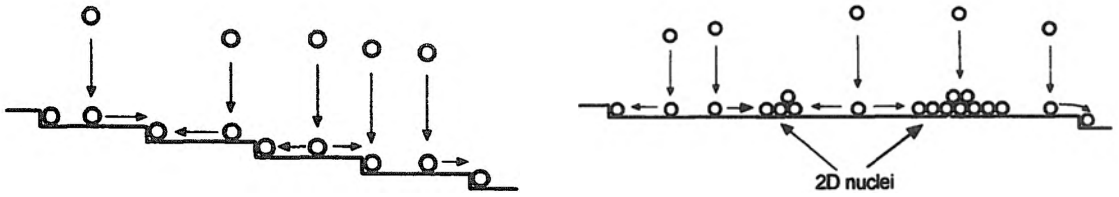

(a) Step-wise growth arising from a misorientated substrate (b) Terrace growth arising from a well-oriented substrate

Figure 2.3: Schematic view of diffusion based growth modes, stepwise and terrace. Reproduced from Lee and Badzian [56] with permission.

2.1.2.4 Etch Pits

Unlike the other surface defects, this imperfection occurs due to etching rather than growth. This etching occurs concurrently with growth, due to the hydrogen or oxygen species present in the plasma. However, in cases of high-quality growth these pits will be grown over and will not be seen.

Alternatively, it is also common to preform etching before and after growths [57] to improve growth quality. If shallow defects are present on the substrate, the etching will remove them, creating square etch pits (on {100} faces) as seen in Figure 2.2d. Aggressive etching can be a useful tool to remove this class of defects. One can note that the square pits are the opposite of the hillocks seen in Figure 2.2a etching preferentially along the defect rather than growing upon it.

2.2 CVD Growth Parameters

With the general principles of diamond synthesis established, an investigation into the parameters of the growth, and their known effect in the literature will follow. Table 2.3 gives examples of parameters from literature which attained high quality growth results for reference, while Table 2.2 gives a summary of how growth parameters will be affected by the growth conditions.

This parameter review and analysis is completed to allow for optimization of growth in section 3.4. However, we must first recognize what we are optimizing for. There are two possible 'optimal' conditions; the quality of the diamond or the growth rate. These terms are defined as:

High Quality As discussed in section 3.3, high quality is defined solely through defects, either in the form of dopants or structural defects.

Growth Rate This work's growth is completed on the {100} surface, which is the conventional choice for homoepitaxial thick films [14, 36, 59]. As it is difficult to get *in situ* measurements of growth rate, [60] it is assumed that growth occurs continuously at the same rate. This is a rough estimation, as surface conditions will change throughout growth, and we ignore pre- and post-etching.

	Pressure (mbar)	Methane $\frac{CH_4}{CH_4+H_2}$	Temp ($^\circ C$)	Power (kW)	α	β	γ
Silva *et al.* [37]	200	4%	840	3	1.8	1.1	5
Silva *et al.* [37]	200	4%	900	3	1.5	0.9	4.4
Tallaire *et al.* [50]	225 [58]	4%	850	3.3	1.7	0.75	5.3
Tallaire *et al.* [50]	225 [58]	4%	950	3.3	1.4	0.83	3.7
Widmann *et al.* [51]	250	3%	790	3	2.3	1.5	—
Widmann *et al.* [51]	250	3%	800	6	1.5	0.5	—

Table 2.3: Several chosen examples of CVD growth conditions and their respective $\boldsymbol{\alpha}$, $\boldsymbol{\beta}$, and $\boldsymbol{\gamma}$ parameters.

2.2.1 Substrate Temperature

The substrate temperature is one of, if not the most, important parameter in high quality single crystal synthesis. Therefore, it has been the most explored growth parameter. For example, diamond has been deposited from temperatures as low as 400°C [61] up to extremes of 1400°C [62]. However, for general high quality diamond growth, the temperature normally used in the current work is within the range of 800°C — 1200°C.

Effect on Growth Rate There are several growth regimes, the first and most widely studied being the "low" temperature regime, which occurs from ∼800°C to 1000°C. This region follows the Arrhenius relationship to model growth rate G_r using an activation energy which will be constant as a function of temperature, E_a and the surface temperature, T in kelvin. The general expression for this is: [63]

$$G_r \propto exp\left(\frac{-E_a}{RT}\right) \tag{2.2}$$

This Arrhenius relationship holds until T_{max}. T_{max} is 1000°C at typical growth conditions, but this limit is known to shift (1000°C — 1100°C). The main condition which pushes this maximum temperature up is the chamber pressure. The E_a term will depend on a number of factors and hence the temperature dependence can look linear or exponential [63, 64].

After the T_{max} is reached, the growth mode changes to be diffusion controlled, which shows weak temperature dependence. Further increasing the temperature past this point has little effect on the growth rate of the diamond, but may encourage graphite deposition. An example of this is given by Mokuno *et al.* [65] who find no temperature dependence of growth above 1100°C.

Effect on Growth Morphologies When only considering the growth rate, it is reasonable to push the temperature to T_{max} in order to gain the highest growth rate. However, this may create undesired growth conditions [29, 50] as an increase in temperature will lead to all three growth parameters (α, β, and γ) decreasing [37].

In the "low" temperature region governed by equation 2.2, this behaviour is explained by the variation of E_a based upon the crystal plane. For example, the {100} plane has significantly lower activation energy than the {111} plane [66]. Plugging in reasonable values, the {100} plane will have a growth rate increase of 1.7x by changing the substrate temperature from 800°C to 900°C. In the {111} plane, this would be an increase of 2.3x. Similar relations exist for all crystalline planes.

2.2.2 Methane Concentration

The methane concentration is heavily influential in the growth process. It is defined as the percentage of methane in reference to the total gas inflow. These percentages are calculated based on gases entering the chamber and therefore are not necessarily representative of the current methane percentage.

Effect on Growth Rates Since methane is the carbon source in the CVD diamond growth process, it can constitute the limiting factor in the reaction. This is the case when the microwave power and chamber pressure are high, creating a reaction controlled mode, where the reactant is the limiting factor and hence the inclusion of additional reactant allows the growth to increase linearly. This has been shown to be true under the following conditions: 3.8 kW, 160 Torr (213 mbar) and methane 4% — 10% [67]. This relation is corroborated by other experiments with lower powers of 1 – 3 kW and is valid to 10–20% concentrations [44, 60].

In the case of lower methane $< 1\%$ and lower power (including hot filament CVD), it is known that growth rate is proportional to the square root of the methane concentration. This growth rate is due to the domination of non-growth-related chemical radicals created in the plasma [67].

Effect on Quality The major downside of increasing the methane concentration is a decrease in the overall diamond quality. The extreme limit of this process will lead to soot forming on the reactor walls and a limiting of diamond growth. This has been reported at 8–10% [37, 50], although high growth rates of 50–100 μm/hr have been reported at methane concentrations of 8–22% [68]. These samples are considered to be of "optical" quality and great care must be taken to reduce the number of defects incorporated. Only specific reactors designed to allow for these sooty reactions can allow for these specialized growths. [28]

There is evidence that the methane concentration has an optimal range to achieve smooth surface quality [29]. Below this concentration, the etching of hydrogen will have a large effect and cause etch pits across the surface of the grown diamond. As methane is increased, an optimal range is found, where the surface is considered smooth (ex. power density of 95 Wcm^{-3}, T= 850°C $\implies$ 4% methane[29]). But above this optimal range, step bunching occurs, which is known to be associated with defects and impurities.

Effect on Growth Modes Silva *et al.* [37], has shown that all three growth parameters (α, β, and γ) trend upwards at a linear rate when methane concentration is varied from 4% to 7%. This change affects the γ parameter particularly strongly, meaning the {113} faces will often appear significantly in these high concentration growths. On a traditional HPHT diamond square substrate, this will appear as four angled corners on the top face as can be seen in Figure 2.1a.

2.2.3 Chamber Pressure

The chamber pressure heavily influences other parameters listed, particularly the plasma shape and the substrate temperature. It will increase plasma density and increase surface temperature as well, both due to the decreased size of the plasma [64].

In the low-pressure range (65–165 mbar), the growth rate has been shown by Li *et al.* [44] to increase superlinearly, indicating the importance of using higher pressures.

Therefore, moderate/high regime of pressures (200 mbar — 400 mbar) has become the norm in CVD growth as it was shown to obtain simultaneously both high purity and high growth rate [37].

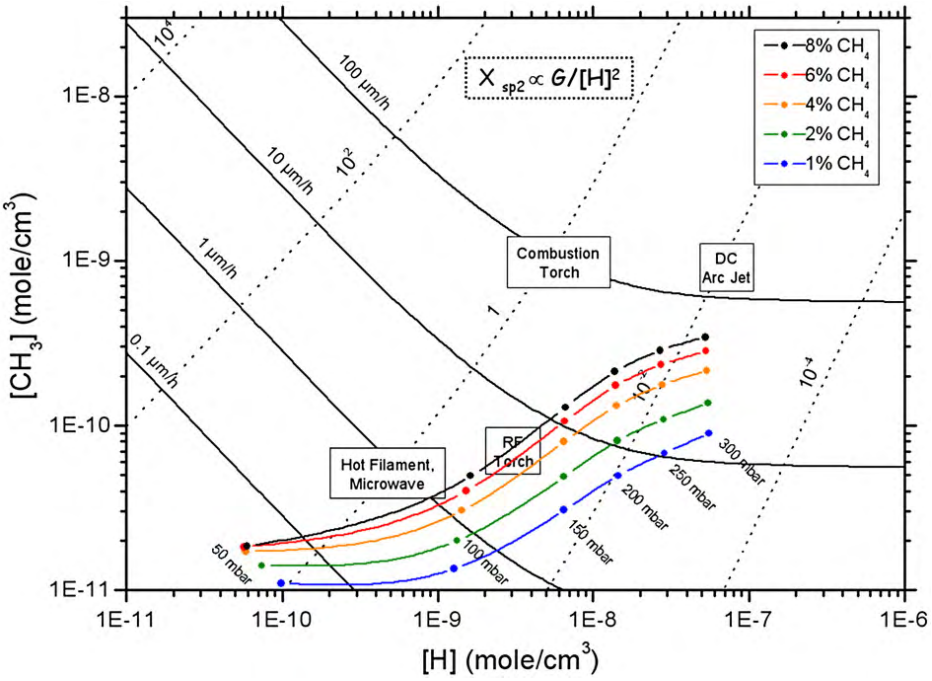

Figure 2.4: Process map reproduced from [37] with permission, which illustrates the operating conditions of CVD reactors to gain high growth rates. The defect level which is shown in the dotted line shown indicates the importance of high chamber pressures in the cavity.

This is well illustrated in Figure 2.4, which shows significant reductions in defect concentration and increase in growth rate at elevated pressure. In this high pressure range (190–300 mbar) it has been shown that the growth rate increases are nearly linear [65]. Recent studies have also indicated that high-pressure operation (>500 mbar) may be the future of high quality and high-speed growth. These studies by Muehle *et al.* [69] and Bolshakov *et al.* [30] attempt successively higher growth pressures (533 mbar and 800 mbar respectively) and encounter some technical difficulties regarding the plasma tuning. However, these high-pressure depositions show the potential to attain high growth rates (51 μm/hr, 57 μm/hr) with high quality. At these higher pressures, the plasma volume is significantly reduced and hence the power density will be significantly increased as well.

Unlike what is observed with the change of microwave power and substrate temperature, no major issues with morphology are caused by the increase of pressure. Therefore, increasing pressure is likely a wise method of increasing growth rate, as long as the systems related to thermal management and plasma stability can keep up.

Effect on Growth Modes The crystal growth parameters (α and β) do not appear to depend on pressure [51]. This further encourages the use of pressure as a relatively inert parameter to modulate or 'tune' plasma shape and size, focusing on adjusting other parameters to achieve the desired growth modes.

2.2.4 Microwave Power Density

The input microwave power introduced into the system is another key parameter to control growth. The growth rate has been shown, however, to rely upon microwave power density rather than the power itself. This relationship is linear in the range of 65–125 $W\,cm^{-3}$ [29, 50].

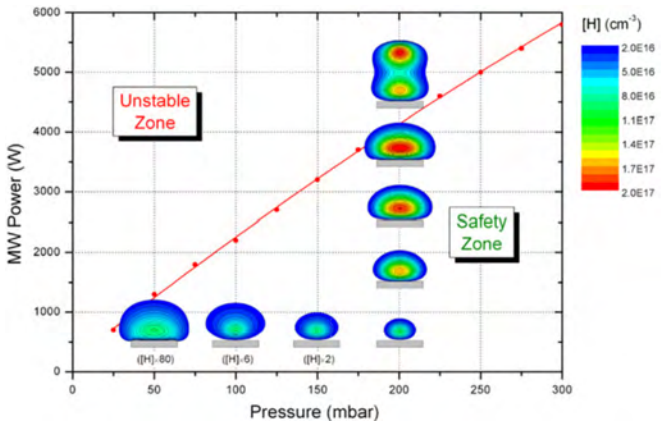

Figure 2.5: Power-pressure domain of the stable region for diamond deposition. Taken from Hassouni *et al.* [38], the suitable/desirable regime for deposition lies 10%- 20% below the transition line.

To compute the microwave power density, the volume of the plasma must be measured. This can be accomplished by taking the half maximum brightness level of the emission to measure the plasma volume through the use of a CCD based camera. This has been corroborated through the use of a spectrometer (H_α line) to ensure that the appropriate volume was used [28].

Unfortunately, no investigation regarding the influence of microwave power density on the growth parameters could be found in the literature. Widmann *et al.* [51] provides limited data in comparing 3 kW and 6 kW growth parameters, indicating that there is a strong decrease in α, and β with increasing power densities.

2.2.4.1 Pressure/Power Relations

While the goal of this section is to investigate plasma parameters individually in order to see their effects on growth, it is important to note that many of these parameters are intrinsically linked. This comes into effect most prominently for the plasma shape, defined primarily by the reactor geometry, microwave power, and chamber pressure. A schematic of the reactor is shown in Figure 1.5, while a photo is shown in section 2.4.1.

A higher gas pressure will contain the plasma into a smaller volume as the mean free path of the ions will become shorter. Conversely, the higher microwave powers will excite a larger quantity of the gas. An interesting relationship for a cylindrical cavity is shown in Figure 2.5: the relationship which needs to be maintained for the pressure/power relations is linear in the typical MWCVD range. The exact values and shape of the plasma will depend upon the particular reactor's cavity, but operating the reactor outside this range will lead to instabilities. It has also been found that the optimal conditions for containing pure hydrogen plasmas are similar to hydrogen/methane mixes of less than 10% [37]. This is because the introduction of methane minimally varies the electron density as found from models by Hassouni *et al.* [38].

2.2.5 Gas Flow Rate

The effect of gas flow rate on diamond growth is one of the most contentious questions in the field as its effect upon growth rate and growth morphologies is debated [34, 70–72]. The gas flow rate is directly related to the 'residence time' - defined as the time taken to refresh the entire volume of the growth chamber.

Broadly speaking, it can be said that higher flow rates correlate with effects we would expect from higher methane concentrations (higher graphite formation) [72] or higher growth rates [70]. This is reasonable to expect, as higher flows will provide more "fresh" reactants to the surface.

Beyond this observation, it appears that the gas flows effect will be highly dependent on other conditions, such as reactor geometry, substrate temperatures, nitrogen concentration and methane concentrations.

Reactors have been historically run at sub-atmospheric pressures. Therefore, a reactor is prone to air leaks. At low gas flow rates, any minor leak can provide a significant portion of the nitrogen during the growth, hence by decreasing refresh time (increasing gas flow rates) the leak's effect can be reduced.

Perhaps the best evidence of gas flow rate's complicated effect is its ability to grow high quality diamond in a zero flow or sealed environment [34]. This demonstrates that while it is important to optimize the reactors' environment, the gas flow rate is not an intrinsic variable in the plasma's parameters, and hence can be altered significantly depending on the reactor and growth conditions used.

Note that in this work, this parameter is not investigated, therefore all flows are consistent.

2.2.6 Tertiary Gas Inputs

The H_2 and CH_4 gas inputs are now commonly established as the key components of modern CVD growth, but a third gas is often added to change the plasma growth characteristics. We will discuss the additives of nitrogen and oxygen, both of which are also covered in chapter 3.4.

2.2.6.1 Nitrogen (N_2)

Nitrogen is the most common impurity incorporated into the diamond lattice and the most studied additive. Addition of nitrogen into the gas phase will increase the growth rate of the diamond. Even with low nitrogen input in the gas phase (10 ppm), the growth rate can be augmented by 2.5 times [73], this growth is particularly enhanced on the {100} face. This increase is often attributed to a 'relaxing' of the bond structure, allowing for diamond precursors to incorporate easily [74]. However, the exact mechanisms are not firmly established due to the difficulty of directly observing the phenomena, and therefore competing theories exist. This means experimentation is generally used to find optimal parameters rather than simulation work [73, 74].

With defect addition, the quality of the diamond can be strongly reduced, and most groups attempt to reduce the accidental incorporation of nitrogen. Therefore, high purity gases, high quality seals, and gas purifiers are important for controlled growth.

The relationship between added nitrogen in the gas phase and defect creation is related to doping efficiency, as per the equation : $D_e = \frac{[N_s^0]}{[N/C]}$ [73] (Note: defects are of substitutional nitrogen N_s^0). Where $[N/C]$ is the ratio of nitrogen to carbon atoms in the gas phase, found to be on the order of 10^{-4}. The exact doping efficiency will depend on factors such as crystal orientation.

The addition of nitrogen to the gas phase also affects the growth morphology, increasing the $\boldsymbol{\alpha}$ and $\boldsymbol{\beta}$ parameters. The γ parameter appears to be non-linear in this case. Increasing the growth parameters is generally undesirable (except when $\boldsymbol{\alpha > 1.5}$) so it is broadly a boon to have lower nitrogen content. [54]

2.2.6.2 Oxygen (O_2)

Oxygen is an important additive gas in the plasma process and can be used in two major ways.

First, it is used as an ingredient in a pre-treatment step for the CVD synthesis. This allows for higher quality growth, as first shown by Tallaire *et al.* [57] specifically to improve surface morphologies. During this phase, etch pits are created on the surface of the diamond, as the oxygen enhanced plasma will preferentially etch away {111} faces. This removes many of the defects that would have created unwanted growths on the surface. This treatment step is relatively simple to add to many reactors, and therefore has been adopted by several groups. [75, 76]

Secondarily, its further use as an in-growth additive may have more interesting prospects. Early in the study of diamond deposition, it was shown that growth is possible up to the point where carbon and oxygen are approximately equal [77] (2:1 ratio of CH_4:O_2 at maximum). The addition has been shown to increase film quality as etching is highly accelerated, leading to removal of undesired growth modes. It has additionally been related with decreased growth rates and lower temperatures. This is a relatively well-documented phenomenon [78–80]. However oxygen is not a widely used addition for most major groups operating in the space [68, 76].

More recent work has indicated that the quality of the diamond, as measured by the Raman linewidth, improves with O_2 addition. Furthermore, at high oxygen concentrations (2%), it is possible to increase the methane percentage to a high value (10%) while retaining a high level of quality. This addition of oxygen also suppresses polycrystalline diamond forming upon the surrounding substrate [46, 81].

The addition of oxygen to the gas phase has been shown to increase α and γ dramatically with a minimal effect on β. Literature on this topic this is minimal and is focused upon boron doped diamond, but it is logically consistent with previous work, as oxygen is known to preferentially etch the {111} and {113} faces as compared to the {100} face [82].

2.2.7 Misorientation Angle

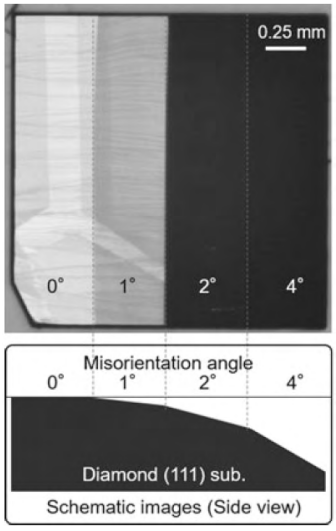

Figure 2.6: Optical microscopy and schematic explanation of misorientation angle. Angles are exaggerated on the schematic. Image from Yang [14], reproduced with permission.

We define the misorientation angle as the angle between the crystalline plane and the material's surface. This is shown schematically in Figure 2.6, and practically it is accomplished by completing

'off-angle' polishing. This off-angle is beneficial mainly for the purposes of gaining smooth final morphologies through stepwise growth. The reasoning behind this can be seen schematically in Figure 2.3 in the comparison of growth which occurs on a misoriented surface with that of a flat surface. The key parameter which differentiates the two are 'terrace widths', and when the terrace/step is short in comparison to the diffusion length of the growth species, the terrace/step will continue to expand in a 'flat' manner. However, if the step is too long, then the species can nucleate in the centre of the surface, creating a 'growth island'. The terrace length will decrease with increasing misorientation angle. For lower methane concentrations (<1%) an angle in the range of 2° will enable atomically smooth growth as shown in a review by Yang [14].

In addition to the increase in surface quality which can be achieved with misorientation angle, the growth rate has been shown to increase linearly between an angle of 0° - 10° [56].

Misorientation angle was not measured in this work. A measurement of this parameter could give a fuller knowledge of the samples studied.

2.2.8 Plasma Shape

The plasma produced in the MWCVD is obtained by acceleration of the electrons in the plasma, causing the necessary reactions to promote diamond growth in the plasma region. This microwave is generally focused slightly above the surface of the substrate, leading to a single plasma region which is affected by the metallic sample substrate. Temperature and plasma density changes as a

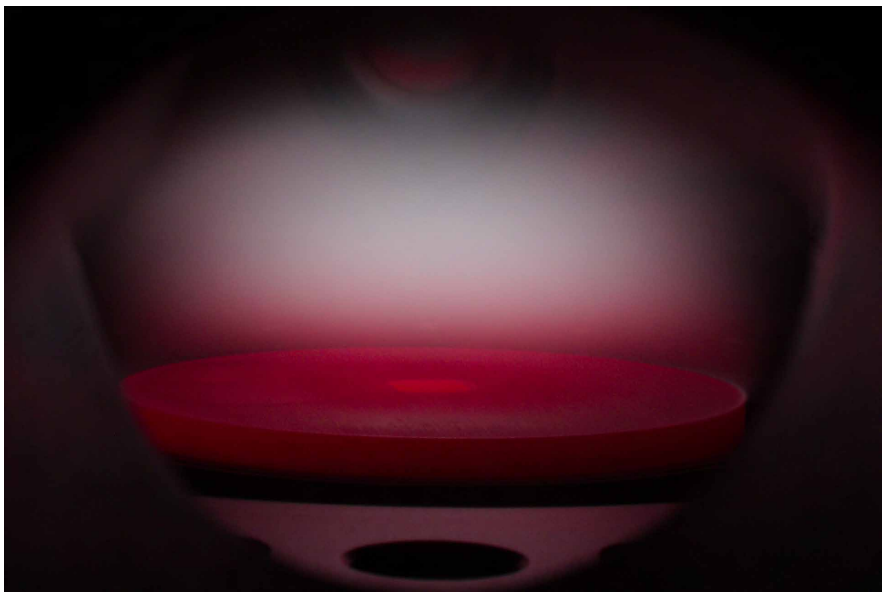

Figure 2.7: Photo of typical CVD growth (4.0 kW, 225 mbar, 4% CH_4, pocketed, SCD-β sample)

function of the excitation energy, so the excited region will have a distribution of chemical species at the varying temperatures across the ball. This chemical variation can be seen as a colour gradient across the plasma emission, or the species can be observed through OES (see Figure 2.7, or section 2.3).Note that this parameter is not easily characterized; hence it has not been heavily studied in the literature.

Work has been completed to simulate these distributions [45, 83] and through this the key parameters which have been listed previously can be manipulated through geometries of the substrate/reactor rather than the direct changes in the input parameters.

2.2.8.1 Substrate Holder Pocketing

One of the limiting factors for high quality diamond growth in an open-faced configuration, as seen in Figure 2.8b, is the simultaneous deposition of polycrystalline diamond (PCD) around the seed (Figure 2.8b). This PCD rim limits both the lateral and vertical growth: laterally by creating unusable surface; and vertically as the rim eventually encloses the entire seed.

This PCD rim has been attributed to a locally enhanced concentration of the microwave plasma around the edge of the seed [84].

The 'pocket' design is based on a simple principle: Instead of having the diamond sit directly upon the holder's surface, it is embedded inside it. This inhibits local plasma enhancement. Instead, the plasma is more evenly distributed across the metallic surface, even though the enclosure can be far (several mm) from the seed.

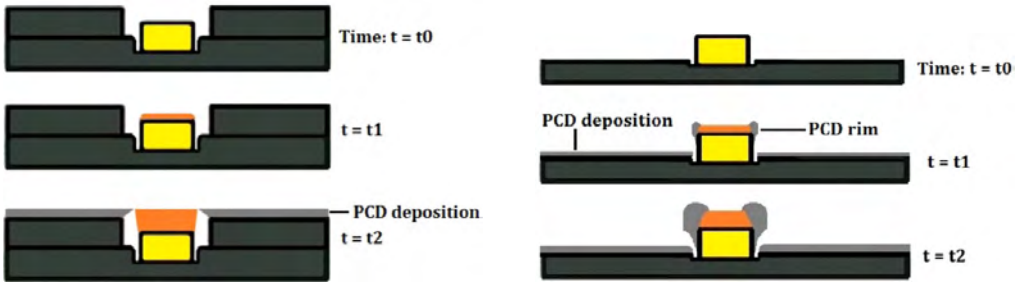

(a) Enclosed/Pocket growth, showing a lack of polycrystalline growths.

(b) Open face growth, showing the polycrystalline growths.

Figure 2.8: Comparison of pocket growth to the "normal" open face growth — reproduced from Nad *et al.* [85] with permission.

The idea of the pocket showed initial success through the work of Mokuno *et al.* [43] who created an "enclosed" diamond holder and showed that it created smooth and flat surface morphology, even with multiple repeated growths. This method of repeated deposition allows for the creation of significant growth on the substrates without interference of the surrounding PCD, and while keeping the reactor geometry consistent. This allowed for much higher limits in vertical growths (24 consecutive depositions without cutting/polishing), but some PCD was still formed along the lateral dimensions.

Furthering this concept Nad *et al.* [85], Wu *et al.* [86], and Charris *et al.* [87] proved that with the optimization of the enclosure the complete elimination of this rim is possible. These pockets place the diamond's top surface a short distance from the holder's top, with the walls of the substrate holder close to the diamond (within ∼1 mm). All growths were stopped once the diamond reached the holder's surface. Pockets which are too large or too small will still result in PCD growth.

Effect on Growth Geometries The most important variable in these recessed pocket holders is the distance from plasma to diamond surface. The further the diamond is from the top surface, the less the plasma is able to interact, which leads to slower depositions with lower stresses and higher quality [86]. However, for many studies this presents a problem as the distance will change as the diamond itself grows. Optimal recessed diamond growers use specialized geometry which keeps this distance constant [30, 46].

Nad *et al.* [33] has completed the most thorough investigation of this topic in collaboration with Charris [55]. They note that the main effect of this distance is the direct relationship with surface temperature. As the plasma is further from the substrate, the temperature drops, necessitating an increase in power.

From this study, it can be stated that with high pressures and relatively high microwave powers, the distance with effective growth is at least 1 - 1.5 mm, and this can be completed at high growth rates (20–30 μm/hr).

The other parameter which can be varied in the pocket is the width of the aperture, as investigated by Charris [55]. From this study, it is indicated that the topologies are not significantly altered. There is an increase in lateral growth as the pocket-size increases, but the vertical growth rates remain relatively stable across the range.

Overall, the studies indicate that there are a wide range of acceptable pocket geometries which will enable high quality and reasonably high-speed growth. This is encouraging for other users, as parameters often vary strongly from reactor to reactor and a narrow set of conditions could be difficult to reproduce. There is a need for further research in optimizing the exact parameters/geometry which will produce the optimal conditions.

Effect on Growth Morphologies It has been shown that with an increase in pocket depth (distance of substrate from plasma), the β parameter will drastically increase, per Charris *et al.* [87] who reported a sevenfold increase in the parameter by increasing surface depth from 0.6 mm to 1.5 mm. This effect was studied in the context of optimizing for a high β to enlarge the surface of the HPHT seed.

2.3 Optical Emission Spectroscopy

While we have attempted to describe the plasma through its effects on diamond growth, it is important to note that it can be directly observed and characterized through its emission. Overall, the optical emission of plasmas are well known and the species introduced are well controlled. Therefore, Optical Emission Spectroscopy (OES) can be used as a powerful diagnostic tool during the etching and growth processes.

We will focus here on the major known species present in the majority of growths. These are hydrogen, carbon from methane and the nitrogen mainly from unintentional leakage from the atmosphere. An example spectrum is shown in Figure 2.9. Note that all bands are known and labelled, with the majority of the lines arising from hydrogen or carbon emissions.

Next, we describe the emission of these chemical species useful in the process.

2.3.0.1 C_2 Dimer (516.52nm)

This plasma band, commonly known as the C_2 dimer, is notable for its intensity in the visible range. Its transition ($d^3\Pi \longrightarrow a^3\Pi$) occurs at 516.52 nm. The C_2 dimer has additional — and weaker — lines which appear at 619 nm, 563 nm, and 471 nm. This leads to a green tint, and generally defines the size and shape of the overall plasma as seen by the unfiltered eye. Due to this ease of measurement, the relationship between the dimer and growth species have been well studied, but the correlations are weak [40].

However, in OES the dimer band is often used to gauge the plasma's temperature; this is

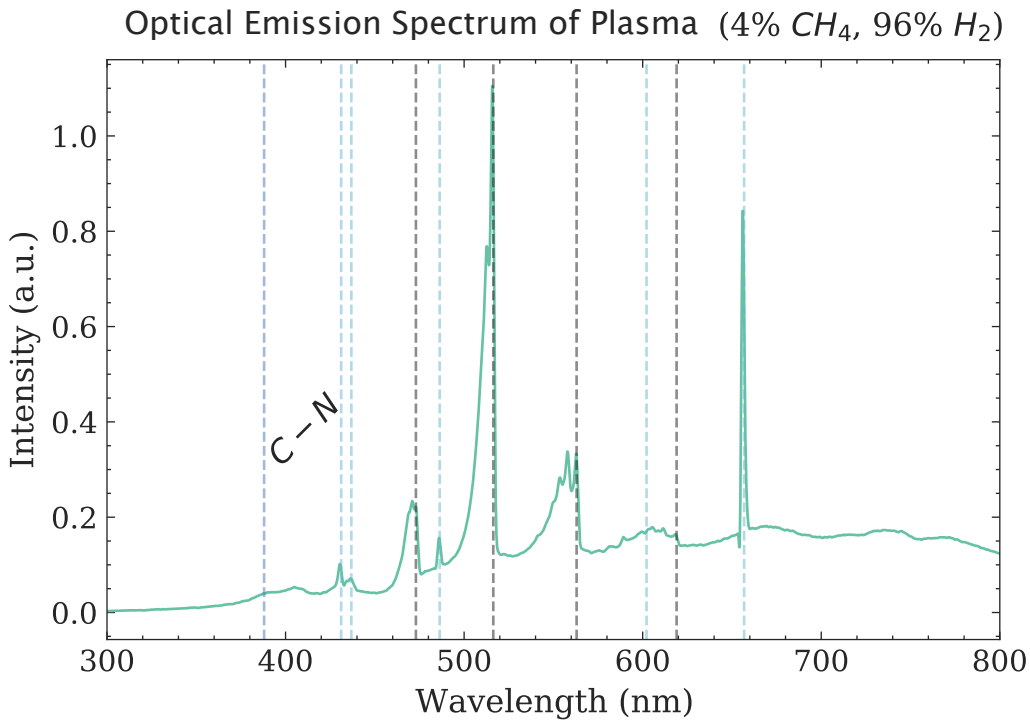

Figure 2.9: An example of an OES spectrum, with several major bands of interest noted. Blue lines represent hydrogen species, while black lines represent the carbon species. Spectra shown is of a stable growth, 15 minutes after methane introduction. Settings used for growth were: 160 mbar, 5 kW, 850°C substrate temperature, 4% methane percentage deposited upon a silicon wafer in the system described in Section 2.4.1.

completed by recording the relative intensities within the 516 nm band and scaling/fitting them to rotational temperature calculated by the Boltzmann relationship. The technique is described by Hemawan and Hemley [88].

2.3.0.2 Hydrogen Species ($H_2, H_\alpha, H_\beta, H_\gamma, CH$)

Hydrogen is the major constituent of the plasma and hence it is responsible for the majority of the strong observable emission lines. These lines are specifically H_2 (602.16 nm), H_α (656.81 nm), H_β (486.31 nm), H_γ (436.85 nm) and CH (431.15 nm).

H_α (656.81 nm) is particularly interesting as it has been shown to correlate well with electron density and the spatial extent of its corresponding emission is often used to define the bounds of the overall plasma. This is intuitively understandable as the ionized hydrogen is both the major constituent of the plasma and is involved in electron creation (Reaction 1.1).

It is important that the H_2 is converted to the ionized hydrogen, so these lines can be used to monitor this conversion. The other lines (H_β - 486.31 nm, H_γ - 436.85 nm, and CH - 431.15 nm) are not well used for plasma diagnostics.

CN Violet System (388.34 nm) Nitrogen is one of the most consequential gas additions in the plasma, but its addition is often unintentional, therefore knowing its exact concentration is useful. The CN band at 388.34 nm can be used for this purpose. The CN system also has additional strong emissions starting at 359.04 nm and 421.58 nm due to its molecular series [89].

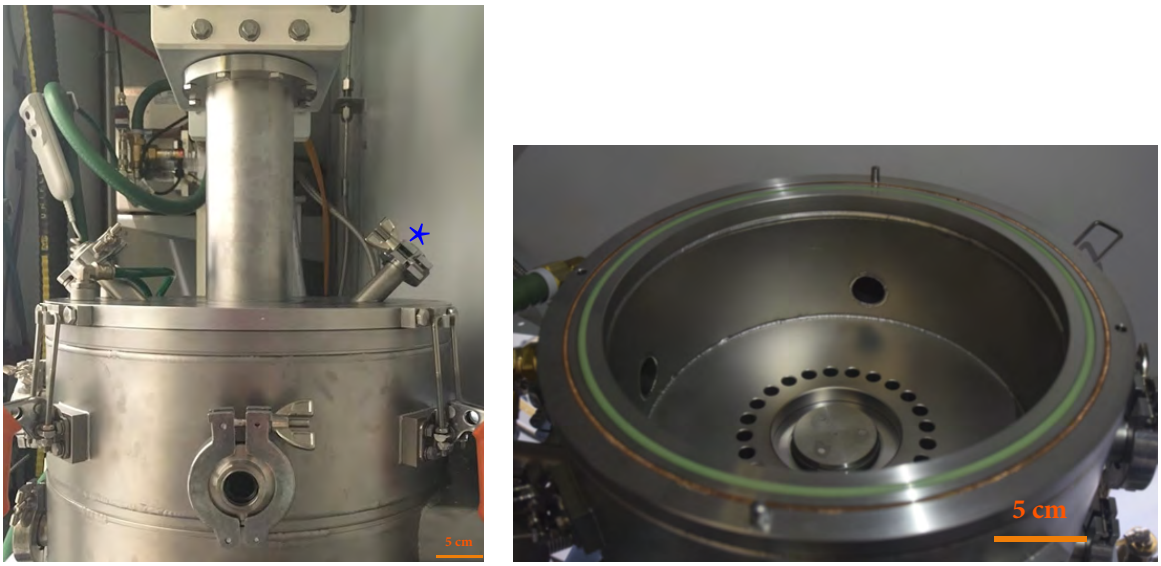

(a) (b)

Figure 2.10: Photos of the reactor, a) Side view of the reactor, showing the column to insert the microwave and gases from the top and the window the pyrometer uses indicated by *. b) View of the interior of the reactor chamber, where the central column would hold the substrate.

These emissions only represent the (often quenched) excited states of the species, and therefore depend upon the chamber conditions. However, several studies have determined CN concentrations from the line's intensity. These have ranged from high concentration studies [90, 91] to high sensitivity measurements [73, 92]. At the highest limit of sensitivity Yurov *et al.* [92] shows that under ideal circumstances (a 7 min acquisition, with a 2400 lines/mm grating) the group can view concentrations of 1 ppm in their plasma. With average or less optimized spectroscopy, it can be stated that if the CN band is visible that there is a significant amount of nitrogen within the chamber [91].

2.4 Experimental System Overview

A microwave plasma chemical vapour deposition (MWCVD) reactor is used for all growths carried out during this work. This machine (MW6-P8013) was made by NeoCoat SA, and can work at a wide range of plasma and growth conditions. See Figure 2.11 for a schematic. The CVD reactor consists of a cylindrical vacuum chamber (Figure 2.10) which can be pumped to a base pressure of about 10^{-6} mbar. The microwave input power can be adjusted from 600 W to 6000 W at 2.45 GHz, and the chamber pressure from 10 mbar to 300 mbar. Substrate temperature can be varied from 500°C to 1200°C. Additionally, there are six gas input lines, which are configured to supply hydrogen, argon, methane, oxygen, nitrogen and carbon dioxide. Deposition is carried out upon a vertically adjustable, cooled, substrate holder with a diameter of 54 mm.

Microwaves are channelled into the top of the reactor chamber, passing through a domed quartz window and are focused to ignite the plasma and minimize reflection. Gases are also introduced from the top of the reactor, 'showering' directly onto the deposition area. Additionally, there are quartz viewing ports which are placed on the side of the vacuum chamber and far (20 cm) from the substrate holder to minimize contamination. The remainder of the reactor is made from stainless

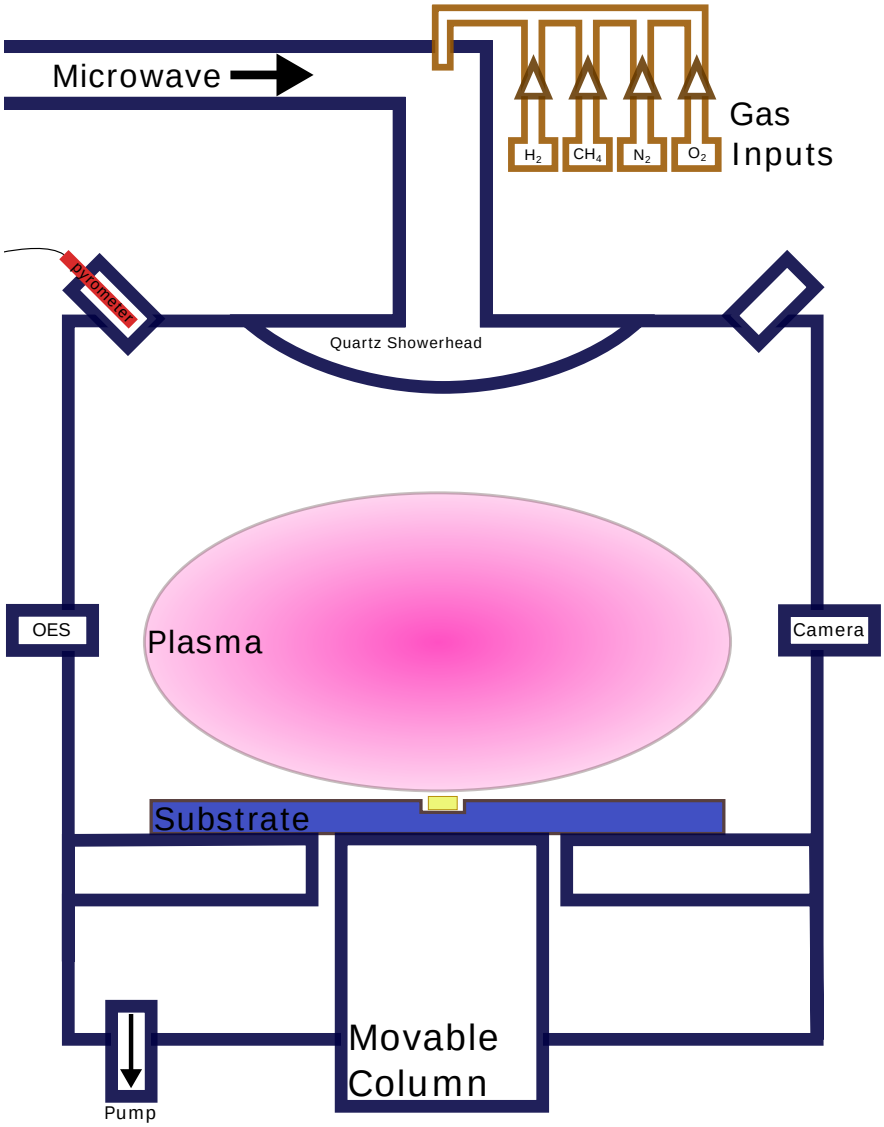

Figure 2.11: A schematic showing the major elements and subsystems of the MWCVD reactor.

steel, and the system has water-cooling system embedded to ensure consistent temperatures.

A load-lock chamber is also part of the system; it allows for the introduction of samples without the breaking of high vacuum in the deposition chamber.

A detailed explanation of CVD subsystems follows. A schematic is shown in Figure 2.11, which notes most of the subsystems employed in the reactor.

2.4.1 Plasma/Microwave Control System

The input microwave and reflected microwave powers are both recorded by the Sairem GMP G3 2.45 GHz microwave generator. The absorbed power is calculated as: $P_{abs} = P_{incident}$ - $P_{reflected}$ - P_{loss}. For our study, however, no modelling or calculations are completed for the P_{loss}. We note that in other studies the P_{loss} has been shown to be minimal ($\sim$2%) [30], and the inaccuracies in reporting plasma volumes would generally dominate this small error. Establishing the level of P_{loss} for our reactor has not been completed.

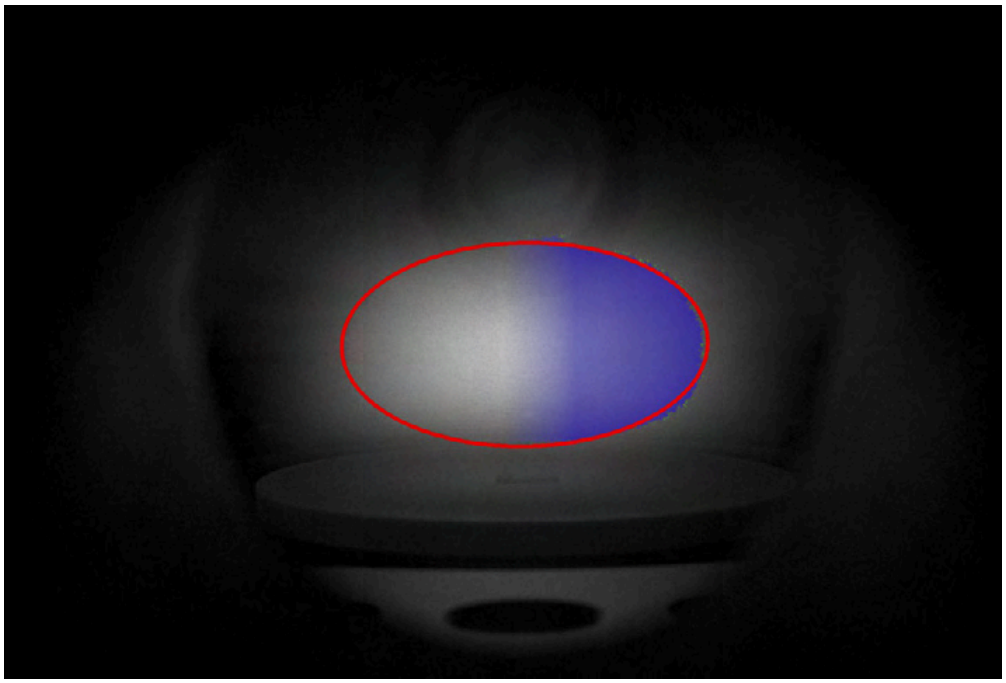

Figure 2.12: Example of plasma cut-off procedure. Background grey scale image is the red channel of a Canon M3 image after being passed through a hydrogen filter. The blue mask on the right shows the zones above the intensity threshold. The area is symmetric and is faded on the left to allow for observation of the plasma. The red line shows the automatically calculated oval, found through use of *The OpenCV Library* [93], which is used to calculate an ellipsoid. Note that the image of the plasma emission is recorded through the CVD system side viewport.

2.4.1.1 Plasma Volume

Estimation of plasma volume is essential for determining power density, which as discussed in section 2.2.4 is directly related to true growth parameters. The plasma volume is calculated by mapping the hydrogen Hα line optical emission intensity I(Hα). Since the intensity I(Hα) is a good indicator of electron concentration n_e [39], we can gain an accurate indication of the plasma volume by use of a camera with a transmission Hα/Hβ filter.

As the intensity cut-off for determining plasma size is not universally agreed upon, for our study the criteria of $1/e$ will be used (see [30] for further discussion). From this determination, we can estimate the plasma volume by fitting the plasma discharge's edge with an oval (See Figure 2.12). The volume of the plasma is then calculated by assuming the plasma region is radially symmetric. In three dimensions this is a flattened ellipsoid, and this flattening is due to the geometry of gas input.

2.4.2 Substrate Temperature

As the growth parameters described are highly sensitive to the substrate temperature, accurate control is important to achieve the growth of high quality diamond. This control is, however, only as valuable as the measurements completed, so both will be investigated here.

2.4.2.1 Temperature Observation

As the operating conditions of the growth will not easily allow for a contact measurement of the temperature, alternative optical-only measurements are preferred. In this case, a pyrometer (Williamson DWF-24-40) is used to measure the temperature from a window, at an angle of 45°C (blue star in Figure 2.10a). The instrument is calibrated as a dual wavelength pyrometer, which measures two narrow and distinct points on the black-body emission curve and then uses the ratio of their respective amplitudes to determine the temperature. This technique is necessary to eliminate the variable emissivity of the substrate (grey-body emission) which will change over the course of the deposition, as PCD has a different emissivity to that of SCD and molybdenum.

Since the plasma is an intense source of light over a broad spectral range, the wavelengths of 2.1 μm and 2.4 μm used by the pyrometer are carefully chosen. These wavelengths are chosen to minimize overlap and interference with any of the known hydrogen, argon, or methane lines.

An additional complication in estimating the substrate temperature can come from monitoring through the diamond (as it is transparent in this range) or viewing areas around the diamond instead of the true growth surface. Unfortunately, it is difficult to eliminate this effect. The pyrometer takes the highest value within its field of view, so a well-centred instrument will minimize the error from these effects. A custom mount was created to adjust the pyrometer aiming orientation and hold it in place. An inline laser is also utilized for aiming.

Thin film interference can also occur when looking at a polished metal substrate for the initial several hours of growth. This was observed in several depositions through the pyrometer.

2.4.2.2 Substrate Temperature Control

As a high temperature ($\sim$ 2000 - 3000°C) plasma is in contact with the substrate, and narrow and consistent temperature is needed for high quality growth, control of temperature is both necessary and non-trivial.

One strategy that is widely used in the literature is the variation of input microwave power to alter the substrate temperature. As the change of power will modify the growth parameters, this strategy has its limitations, as the plasma power, chamber pressure, and substrate temperature will be strongly linked, which limits growth to specific parameter zones. These zones are dependent on the heat dissipation potential of the substrate.

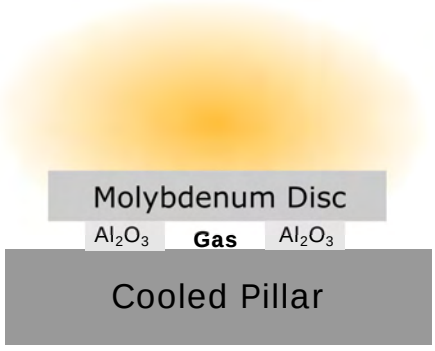

Figure 2.13: Diagram of the cooling solution, where the gas flowed under the molybdenum disk is changed to modify the temperature of the substrate.

The method used in this work directly changes the level of heat dissipation. This is carried out by placing the substrate disk on top of a water-cooled column, with a gas used to transfer heat

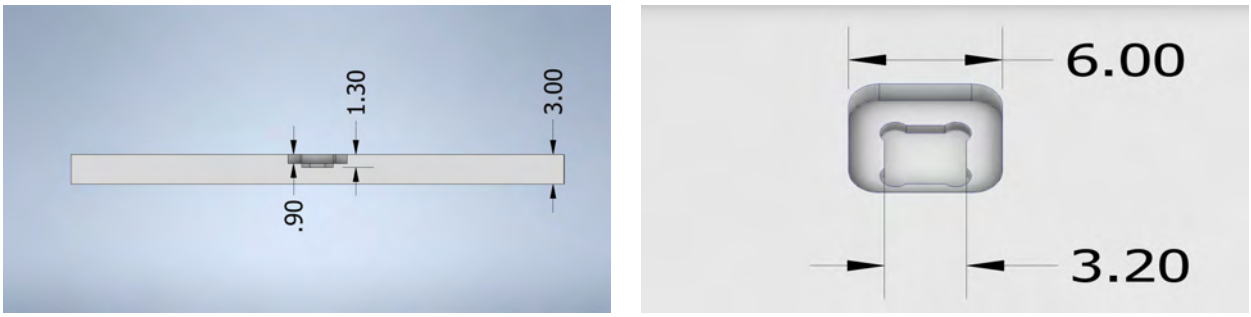

(a) (b)

Figure 2.14: Example of pocket design for the CVD seeds. Pocket depth and width are varied and discussed where applicable. The bottom pocket is machined to hold the seed tightly, while the upper cutout is larger to allow for plasma uniformity. a) Side view of pocket, showing the two tiers of cutouts. b) Isometric view of the cutout, showing curved pocket edges and layers. Dimensions are in mm.

away from the disk (Figure 2.13). The gas can be argon, hydrogen, or a mix of the two. Since hydrogen has a thermal conductivity which is x10 higher than that of argon (186.6 $mW/m \cdot K$, 17.7 $mW/m \cdot K$ respectively [94]), the temperature can be controlled by adjusting the mixing ratios. More argon in the gas mixture will help to maintain a higher substrate temperature. A Proportional–Integral–Derivative (PID) control feedback loop based upon the pyrometer's measurements can be used to control the gas mixture and hence the substrate temperature.

To extend the range of this thermal control, the distance between the disk and cooling pillar is also adjusted by using aluminum oxide spacers of differing thicknesses (100 – 500 μm). This allows coarse control (several hundred $^{\circ}C$), and the adjustment of gas mixing ratios gives us fine control (adjustments range of $\sim 200^{\circ}C$).

2.4.3 Substrate Holder Pocketing

The pocket is described in section 2.2.8.1 and allows for high quality growth of the SCD without polycrystalline edges. In practice, the technique means machining cutouts in the metallic substrate in which the diamond seeds are placed in order to grow.

A drawing of one of our manufactured pockets is shown in Figure 2.14. The general design follows that of Charris [55].

There are two 'levels' of the cutouts, the bottom is machined to tightly hold the seed diamond, promoting thermal transfer through the diamond sides, and ensuring centring within the upper larger pocket. The depth of the cutout is designed to be slightly shorter than that of the diamond, only letting the top of the diamond seed interact strongly with the plasma.

The upper cutout is significantly larger, as plasma non-uniformities will exist close to the molybdenum disk edge. The main objective of the pocket design is to allow the diamond to interact with a highly uniform plasma; which can only occur when the plasma is distanced from the diamond surface. It is noted that PCD grows inevitably on the top surface of the disk, effectively leading to a reduction in the cutout dimensions during growth.

Substrate temperature is one of the most significant factors in the diamond synthesis. It influences crystallinity, morphology, and rate of growth. As the machined pocket is the only thermal contact point between the diamond seed and the molybdenum disk, care is therefore taken to reduce the roughness of the pocket through the use of abrasive blasting (using fine Al_2O_3

particles). Following a deposition, within the pocket there is generally no soot formation under the seed, while in unpocketed growth there is often graphite formation. Avoiding the latter is important.

2.4.4 Substrate Height

To optimize the plasma conditions and allow for substrates of varying geometries, the height of the substrate holder can be adjusted throughout a growth. The column allows for 17 mm of vertical motion, but the vast majority of adjustments between growths take place within a 3 mm range.

Growth Tracking During high growth rate depositions ($> 10\,\mu m/hr$), hundreds of micrometres of undesired PCD diamond is deposited upon the metallic substrate. The increased height of the substrate significantly alters the plasma conditions. To account for these changes, during pocketed growths, the substrate vertical position can be moved down. We refer to this motion as "tracking" the growth.

To track the growth accurately, a feedback signal is required. The intensity of the plasma was chosen as our signal. The plasma intensity as recorded through the red channel by a PiCam v2 (mounted on a side viewing port to monitor the plasma) is used as a proxy for the Hα signal, monitored in real time. A rectangular region of interest across the signal is captured, vertically binned and fit with to a Gaussian profile distribution. The intensity of this Gaussian is monitored in real time, and is used to adjust the vertical substrate position in steps of 10 μm to keep the measured plasma intensity approximately constant. As there exists a mechanical backlash in the column position, corrections are only made in one direction. It was found that applying these corrections kept intensity consistent across the growth, and that the distance tracked matched well with the PCD formation. This may indicate that the deposited PCD on the substrate is the major cause of plasma 'drift' during synthesis.

2.4.5 Gas Inputs

The gases which constitute the initial chemical species are introduced to rain down onto the substrate. The gases are premixed before introduction to the chamber through the use of individual gas mass flow controllers. The total gas flow is set to 800 sccm, and the percentage of introduced gas is calculated by $\frac{gas\,flow}{total\,gas\,flow}$. The majority ($\geq$ 95%) of the gas input is hydrogen, and methane is generally input at 1–5%.

2.4.5.1 Gas Purities

To reduce the nitrogen defects incorporated into the grown diamond, care is taken to ensure that the input gases are of high purity and the known sources of nitrogen are well understood. Purities are measured in N's, standing for 'nines'. 2N = 99% purity, 3N = 99.9% purity, *etc*, indicating the content of the main gas species.

The methane which is used is of 4N or 5N purity and has 70 or 5 ppm of nitrogen respectively. This is one of the major sources of unintentional nitrogen incorporation within the growth process. If the methane constitutes 5% of the total input gas, this will introduce 2 or 0.2 ppm of nitrogen into the gas phase.

It is noted that other gases present have a negligible impact on the diamond growth process. For methane of 5N purity, they are C_2H_6 at <5 ppm, O_2 at <2 ppm, and other hydrocarbons at <2 ppm.

The hydrogen which is used is of 4N quality and is subsequently passed through a heated palladium sheet, which purifies it to 9N level, leaving 1 ppb of nitrogen within the input gas. The purification step is crucial as the hydrogen constitutes the majority of the input gas. Without purification, the nitrogen from a 4N purity hydrogen bottle would contribute <20 ppm (95% mixture) of nitrogen, which would often be the largest nitrogen contribution.

The final known contributors of unintentional gas flows are the vacuum leaks which exist in the system. These are quantified by a rate leak test executed before the start of a growth, which evacuates the reactor to a high vacuum (10^{-5} — 10^{-6} mbar), and then allows for the chamber to partially fill for 10 minutes as a result of leaks and outgasing. From this, the quality of the vacuum seal can be determined, and a leak rate is measured. This leak rate is converted assuming it acts as an ideal gas. We can convert it through:

$$\Delta PV = \Delta nRT \qquad \text{We have a pressure flow rate in mbar/min}$$

$$\Delta V_{atm} = \frac{\Delta nRT}{P_{atm}} \qquad \Delta V_{atm} \text{ is known as volumetric flow rate and is measured in sccm}$$

$$\Delta V_{atm} = \frac{\Delta PV}{P_{atm}}$$

The volumetric flow rate (ΔV_{atm}) is then corrected to represent the correct pressure differential (as it leaks into the full reactor, which is at $\sim$ 150 mbar rather than at a vacuum). This correction is: Flow $\propto \sqrt{P_1 - P_2}$, and will account for a correction on the order of 5%.

The leak rate therefore enables a calculation of the undesirable gas content. For a leak rate of 5 $\times 10^{-4}$mbar/min, this translates into nitrogen content of 7 ppm at 800 sccm of total flow. Microleaks can therefore become the dominant source of unintentional nitrogen in the gas volume and necessary measures are taken to control this problem. Extended pumping of the chamber before deposition, checking of o-rings, and pre-pumping of input lines are carefully completed.

2.4.6 Substrate Cleaning

Defects are known to propagate from the diamond seed surface into the newly synthesized diamond, due to structural defects or polishing contaminants. This is one of the most significant sources of defects, therefore significant action must be taken to clean the substrates preceding growth. This is accomplished by chemical and physical etching methods as outlined below.

Chemical Etching To remove surface contaminants, each diamond sample was subjected to a chemical cleaning procedure prior to deposition. This effort focused upon removing any graphite and metallic surface defects present following other sample preparation procedures. The steps taken for the chemical cleaning were:

1. Diamond placed in a 1:1 mixture of nitric/sulphuric acid (40 mL & 40 mL), brought to boil (300°C). This step lasts for 30 minutes;
2. Diamond is transferred to boiling HCl at 300°C for 25 minutes;
3. Diamond is transferred to *Aqua Regia* (1:3 nitric/hydrochloric acid mixture) for 1 hour ;

4. Ultrasonic cleaning is accomplished in acetone for 10 minutes;
5. Ultrasonic cleaning is accomplished in methanol for 10 minutes; and
6. Nitrogen gas drying.

The nitric/sulphuric acid boils are mainly completed with the goal of removing graphite and other surface containments with a strongly oxidizing reaction.

The hydrochloric acid boil is aimed at etching metallic contaminants and the *Aqua Regia* continues this process, eliminating many of the difficult metal inclusions. Acetone/methanol ultrasonic cleans will remove any organic contamination from handling as well as residue from the acid. Following the cleaning procedure, the diamond seeds are placed inside the reactor.

This chemical cleaning procedure was developed by referencing several publications which describe diamond cleaning within their publications [51, 55, 95, 96]. Perchloric acid etching [97] and chromium based oxidizing reactions [98] were also considered and would likely allow for a faster processing times, but the methods defined here were deemed sufficient when considering safety, time pressures and available equipment. The determination of etch times were completed by analyzing the sample's condition through spectroscopy.

Plasma Etching In addition to the acid cleaning, plasma etching is used before each growth. Plasma etching is necessary to remove any contaminants which were not successfully removed through the acid boil. This step based on strong oxidation reactions to etch away weaker diamond, which are effectively structural defects left by the chemical cleaning. This leads to etch pits on the surface. This in turn means the growth will have to fill in these pits, which is not known to cause major issues.

The main plasma etch is a hydrogen-oxygen etch, which, as discussed in section 2.2.6.2, has been proven to remove defects. This plasma etch is accomplished with 2% O_2 (800 sccm total) for a period of two hours followed by a one-hour pure hydrogen etch at the same parameters as will be used for the final growth.

Post-Deposition Cleaning After the deposition, a secondary cleaning procedure for the grown diamonds is completed to remove the significant non-diamond carbonic layer. This second cleaning is similar to the pre-deposition cleaning, but with three major differences:

1. A plasma etch is completed before the chemical cleaning;
2. Only a hydrogen plasma etch is performed; and
3. The nitric/sulphuric acid etch is completed for a minimum of 1 hour.

Since an oxygen plasma etch induces etch pits, it is not completed for the post-cleaning. The nitric/sulphuric acid etch can also take a significant amount of time, as the graphite layer formed is often significant. In this process, the acid mixture is refreshed every hour if etching is not complete. Afterwards, the grown diamond is characterized by Raman spectroscopy to determine if there is any graphite remaining. Chemical cleaning is only deemed complete if no traces of graphite are found.

It is worth noting that in the case of PCD growth, it is common for the polycrystalline samples to skip the acid etching steps due to the delicate nature of the samples. Additionally, graphite quantity is likely significantly higher. This will be discussed further for specific samples, such as in section 4.1.3.

2.5 Deposition Procedure

A standardized procedure is utilized to deposit diamond with the previously mentioned subsystems. An example of this full deposition process is given in Chapter 3.4, but the creation and stabilization of the growth plasma will be explained here. These procedures are consistent throughout all growths.

2.5.1 Ignition/Ramp

Note that while the conditions quoted here and in the literature are the stable conditions (ex. 3.8 kW and 1000°C), the plasma/temperature must be slowly brought up to these values not to shock the system or substrate.

The plasma is ignited as a pure hydrogen plasma at a nominal microwave power of 1000 W (30 mbar) and ramped up to the desired growth pressure or power through the hydrogen plasma coupling condition according to:

$$\text{Microwave Power (W)} = \text{Pressure (mbar)} \times\ 20\ W/mbar\ + 400\ W \tag{2.3}$$

This allows for a stable plasma to be initiated (similar to Figure 2.5). This plasma has the least effect upon the substrate out of the possible plasmas therefore all tuning is completed as a pure hydrogen plasma. The vertical position of the plasma is monitored to focus it slightly above the sample substrate. Logs and photographs are completed and compared to ensure consistency in the plasma position. A similar level of local plasma enhancement (plasma bunching on the sides of the metallic substrate), vertical plasma height, reflected power, and radial size are used as metrics to determine a consistent plasma position.

As mentioned previously (section 2.4.1.1) plasma position and plasma shape are difficult to quantify and therefore not well studied in the literature. This means that while these growths presented are internally consistent, tuning of the vertical position is necessary to complete experimentally on a per-reactor basis. A comprehensive simulation study which analyzes these factors could be useful for experimentalists.

2.5.1.1 Plasma Etching

As discussed in section 2.4.6, these etching procedures using the plasmas are completed at growth condition and are run for the noted time (generally 1 hour for hydrogen plasma and 2 hours for oxygen plasma etch).

2.5.1.2 Growth

Methane is introduced into the chamber at growth conditions. Upon the mixing with methane, the substrate temperature will change and is readjusted accordingly. Efforts are made to control any variation to within ±20 °C and to minimize reflected power through microwave tuning.

Early stabilization (minutes) will often fluctuate in the ±20 °C range, while later in growth, the temperature is typically controlled within ±2 °C.

2.5.2 Optical Emission Spectroscopy

To characterize the plasma conditions, its spectral emission characteristics are monitored. Data is captured using an Ocean Optics USB4000 spectrometer. The spectrometer is attached by a fibre

to a lens which points at the plasma through one of the chamber viewports. The spectrometer has 3648 pixels, a slit size of 10 μm and a grating of 600 lines/mm. It is set to detect a spectral range of 177 nm to 892 nm. This gives an approximate resolution of 1.08 nm as defined by the manufacturer, which allows for analysis of broad signals.

A wide spectral range was chosen as it gives a broad understanding of the plasma and allows use as a diagnostic tool. The majority of emission peaks from the plasma are highly intense and spectrally well resolved.

It is recommended that for accurate observation of a single line (ex. 388 nm C-N line), or to observe temperature (C_2 dimer) that a high resolution, high sensitivity spectrometer is used.

Chapter 3

High-Quality Diamond Growth (Single Crystal)

3.1 Introduction

Most of the interesting or extreme properties of diamond fundamentally originate from the four strong covalent bonds between carbon atoms, which are arranged in the so-called diamond cubic crystalline structure. The alteration of this structure will quickly change the physical properties of the material; therefore for further scientific exploration, it is essential that synthesized diamond is of a high quality.

As diamond growth which utilizes the CVD process is a new endeavour at Laboratoire de physique des solides denses (LPSD), a significant period of time was required to optimize the experimental procedures. This chapter first looks at explaining how the determination of high quality diamond is accomplished (section 3.2), and proceeds to give an example of growth and characterization for a high quality diamond sample (section 3.4).

3.2 Characterization Methods

As improvement of the diamond growth process is only possible once the resulting samples are well understood, the physical characterization is a key aspect of this work.

The techniques selected to determine the quality of samples grown were: Fourier Transform Infrared Absorption (Mid-IR), Electron Paramagnetic Resonance (EPR), Raman Spectroscopy (RS), Profilometry, Photoluminescence (PL), Scanning Electron Microscopy (SEM) and Birefringence Imaging (BI). A discussion of these various techniques follows.

3.2.1 Vibrational Spectroscopy

Since defects will form bonds inside the diamond crystal lattice, they have the potential to be probed by vibrational spectroscopy. To characterize the vibrational states in samples two complimentary methods are used: Raman and infrared spectroscopy, which allow for the measure of vibrational energies related to different bonds or defects. Both spectroscopic methods obey different selection rules, and when combined, can give a more complete picture of the symmetry and other physical properties of a studied material.

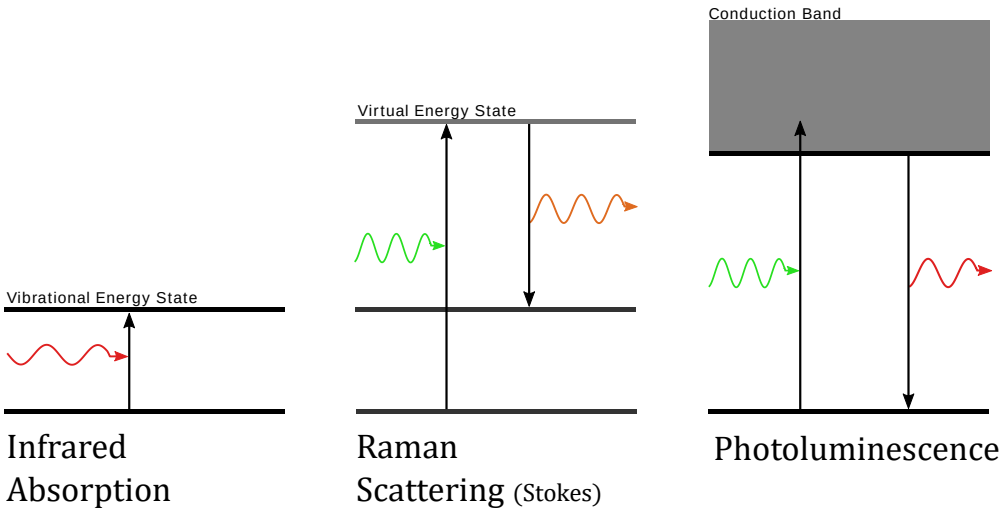

Figure 3.1: Energy diagrams of different light-matter interactions. IR absorption is a direct vibrational coupling, Raman scattering (Stokes) implies a relaxation to a vibrational state, and photoluminescence results in the emission of light arising from electronic state transitions (commonly arising from transitions into the conduction band, as pictured).

3.2.2 Infrared Absorption

Infrared (IR) spectroscopy is based on the direct absorption of the photons' energy into a vibrational state. For this light to be absorbed (IR activity), the transition must satisfy a selection criterion. These can be described classically by the activation of an electric dipole moment [99].

Broadly speaking, a system which absorbs through this process requires an 'asymmetric' bond. This asymmetry allows the dipole and hence the absorption to exist. (e.g., the stretching vibration of gaseous CO is active, but in not in gaseous H_2 [100]). Note that crystal lattice vibrations can complicate this simple model, but they will not be a primary cause of absorption for the isolated diamond defects which are studied here.

Practically, IR absorption spectroscopy requires a simple experimental system. A known broadband IR source (high quality blackbody) is transmitted through a sample, and all transmitted wavelengths in the range are detected. The measured quantity—absorbance—is expressed as:

$$A = log\left(\frac{I_o}{I_t}\right) \qquad I_o \text{ is reference, } I_t \text{ is transmitted signal} \tag{3.1}$$

Absolute IR absorption can be quantified if the material's thickness is known. In this case, an absorption coefficient (μ_a) is defined as $\mu_a = \frac{A}{length}$. For IR absorption, it is commonly reported in units of cm^{-1} and is directly proportional to the concentration of absorbing material. Concentrations of absorbing material (for instance vibration states of defects in diamond) are commonly reported in ppm (parts per million total atoms) for diamond research and in general in defects/cm^3 or cm^{-3} for CVD related work. In this study both will be reported in the format of ppm (cm^{-3}).

As diamond is an inherently symmetric material, the majority of defects will disturb its symmetry, thus creating an environment which often results in IR absorption. Additionally, the perfect diamond is mostly IR transparent outside of the two-phonon region (1333–2666 cm^{-1}). For these reasons, IR absorption from the defects are likely to be active and observed.

3.2.2.1 Experimental Procedure - Fourier Transform Infrared Spectroscopy (FTIR)

To capture mid-infrared absorption, a FTIR microscope was used (Agilent Cary 600 series). It uses a liquid nitrogen cooled HgCdTe (MCT) point detector and a mid-IR thermal source to measure an absorption spectrum in the range of 400 to 4000 cm^{-1} at a scan speed of 2.5 kHz. The sample area and optics were flooded with dry nitrogen gas throughout the acquisition, to minimize atmospheric vapour and CO_2 IR absorption.

Diamond samples were placed and imaged on top of a two millimetre thick calcium fluoride (CaF_2) slide, which is transparent up to the end of the mid-infrared region. But below 1000 cm^{-1} it becomes opaque, hence limiting our analysis to the range of 1000–4000 cm^{-1}. Reference measurements were completed with the CaF_2 to eliminate its influence.

The samples are elevated above the CaF_2 to avoid thin film interference occurring in the μm sized air gap which can occur between the diamond and the CaF_2 slide.

Each sample IR absorption spectrum is background subtracted and scaled based on the diamond intrinsic absorption peak at 1995 cm^{-1} (two-phonon band) to an absorbance value of 12.3 cm^{-1}. This is a commonly used scaling technique [101], which gives the path length of the diamond, and allows for measurements of the absorption coefficient. When the path length was compared to the sample thickness, they were found to agree well. These thickness measurements were completed with a Mitutoyo micrometer (with a precision of $\pm$ 1 μm).

Signal to Noise Ratio (SNR) of the recorded IR spectra differed depending on the level of light scattering and sample opacity. For this reason, post-sample cleaning was conducted before data collection to improve clarity (See section 2.4.6). All quantitative concentration measurements were performed at a resolution of 2 cm^{-1} for consistency and a local background subtraction was executed when analyzing any absorption particular peak. The number of average scans varied considerably dependent on the sample, with PCD samples requiring a minimum of 300 averaged scans. Many SCD samples only required 30 scans to have low levels of noise.

Samples synthesized on top of seeds were imaged only through the growth portion. Pre-growth baselines for all seeds were captured and then compared to the synthesized sector.

IR absorption spectrum of thin PCD films were also recorded, although many scattered light significantly and therefore required high levels of background subtraction following extended acquisitions. Several of the thinner films obtained also presented large interference signals related to thin-film interference. This can be used for thickness determination or can be simply eliminated through adequate filtering such as peak removal in the interferogram (in Fourier space).

3.2.3 Raman Spectroscopy

The selection rules allowing Raman scattering to occur essentially reverse the conservation laws of IR absorption as it is a scattering rather than absorption technique. Consequently, it is a fundamentally complementary technique to IR absorption. This means that the Raman scattering technique will probe vibrations related to symmetric bonds (such as the C−C bond in diamond) and is classically described by a change in polarizability.

The scattering process underlying the technique is shown in Figure 3.1, and shows the relaxation of the virtually excited state into a different state from where it was originally excited. This occurs at a rate of 10^{-6} less than relaxation back to the original state, but with a high-power laser it can gain relatively high rates. The relaxation can lead to corresponding vibrational energies above

or below the input wavelength; in this work only those that are lower energy will be considered (longer λ, corresponding to what is known as Stokes scattering) as they are generally more intense at room or low temperatures.

3.2.4 Photoluminescence

Photon-induced luminescence or photoluminescence should be presented alongside Raman scattering as the two processes are often recorded using the same equipment – as is the case in this work. Examples of these can be seen in Figures 3.11 and A.2a.

The cause of the photon emission is a higher energy electronic band excitation followed by a relaxation to another electronic state. Practically, in diamond this shows up through defect cluster states known as colour centres (as they often emit in the visible range). Examples of clusters found in diamond are defects formed by an impurity atomic species, and a carbon vacancy. Notable examples are negatively charged nitrogen and silicon vacancy defects, abbreviated as NV^- and SiV^-, respectively. They have a Zero Phonon Line (ZPL), which results from the direct transition from the intrinsic excited to ground state, and a Phonon Side Band (PSB), which is caused by relaxation with the assistance of some phonons. This photoluminescence technique is not usually reliable for a quantitative analysis.

3.2.4.1 Raman Spectroscopy/Photoluminescence Experimental Procedure

Excitation with a frequency doubled Nd:YAG laser (532.18 nm) or diode laser (785 nm) was conducted in a near-confocal Raman spectroscopy setup in the back scattering configuration. Scattered light was recorded on a 0.5 m Andor spectrograph and a Andor Newton cooled CCD. Neon emission calibration was completed for every dataset using sub-pixel Lorentzian peak fits for high accuracy spectral positions ($\pm 0.01\ nm$ for 300 lines/mm diffraction grating, $\pm 0.001\ nm$ for 1799 lines/mm grating). Each dataset was collected with the focal plane of the Raman microscope situated to maximize the intensity of the diamond fundamental Raman line. Additionally, a high-quality CVD diamond, used as a 'standard' was captured and compared to ensure a calibration (central wavelength and linewidth) consistency of results.

To distinguish Raman signals from those due to PL, spectra can be taken with incident light at different excitation wavelengths. Only graphite and diamond were found to have important Raman signals. Excitation at longer wavelengths was generally used to find and record PL of colour centres with emissions and absorption in that spectral range.

As expected, few defects showed up in the Raman spectra [101], but the major emission known as the 'diamond line' (at 1332.5 cm^{-1}, at room conditions) was clearly visible. In general the width of the diamond Raman line indicated the quality of the lattice, while its position points to internal strains or temperature shifts [14, 101, 102].

To determine the linewidth of this diamond line, a correction for instrument related broadening was required [103]. Additionally, instrument broadening and laser width were taken into account. To complete this, a correction function was applied by fitting the peak with a pseudo-Voigt function (see Váczi [104] for additional discussion). Only post-correction linewidths are reported for the diamond fundamental Raman line, but the plots show the data as recorded. The reporting of the diamond linewidth as either corrected or uncorrected is not standardized in the literature [29, 105].

Raman spectroscopy can also be sensitive to non-dopant defects such as stacking faults, and

can show when other carbon solid-state phases exist alongside the diamond. The identification of these other constituents in a sample is important, as these imperfections in the diamond growth often occur and are not easily identifiable through other spectroscopic methods.

3.2.5 Electron Paramagnetic Resonance

Electron Paramagnetic Resonance (EPR) or Electron Spin Resonance (ESR) is a key tool in observing the presence of impurities in diamond. EPR works well in concert with infrared absorption to quantify the nitrogen concentration in diamond. The two techniques complement each other, as they have specific and complementary advantages with respect to sensitivity and specificity. IR absorption has low sensitivity, but allows for high specificity of the defects under question, spectral shapes or line frequencies can be considered 'signatures' of specific defects. Alternatively, EPR presents a low specificity, due to convolved spectra, it offers, however, an unparalleled sensitivity for observing those defects. These characterization tools offer synergetic methodologies: whereas IR absorption can be used in broad identification for the majority of defects in a sample, EPR is useful in accurately quantifying low levels of specific defects.

The high sensitivity EPR allow for the measurement of 10^{11} spins — meaning the concentration sensitivity achievable depends on the total volume of material under study. For example, EPR is capable of giving a sensitivity of 0.05 ppb (10^{13} cm^{-3}) spins in a 40 mg sample [22]. For its sensitivity EPR is an irreplaceable tool to sense low impurity and defect levels and as such, quantify high purity samples for sensing or electronic devices application. These uses often require ultrahigh purities in the ppb range (10^{15} cm^{-3}) N [3].

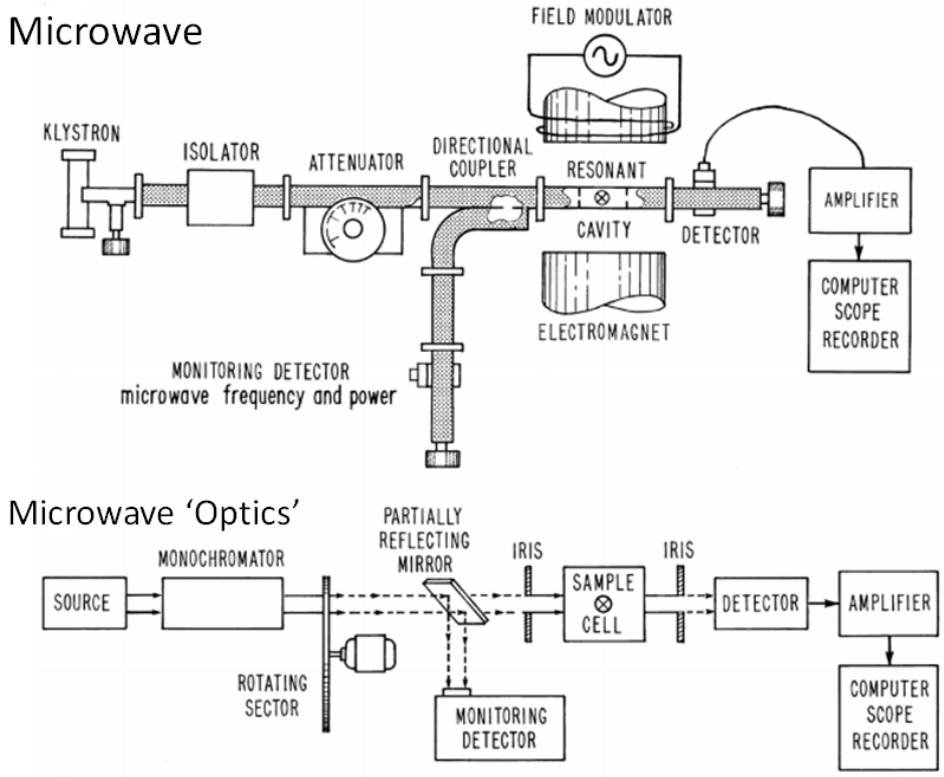

Figure 3.2: Schematic diagram of the EPR microwave setup, with equivalent physical 'optics' shown below. Adapted from Eaton *et al.* [106] with permission.

EPR Theory The Zeeman effect is a phenomenon where a single unpaired electron splits energy levels under the influence of an external magnetic field. This energy difference will only depend on three variables: Strength of the magnetic field, gyromagnetic ratio (electron $\implies$ g_e=2.0023), and the Bohr magneton value (μ_B). The ΔE energy degeneracy is thus given by:

$$\Delta E = h\nu = g\mu_B B_0 \tag{3.2}$$

Experimentally, the magnetic field (B_0) or the radiation frequency (ν) can be varied. Due to technical considerations, the magnetic field magnitude is scanned and while the absorption from the sample is monitored at a fixed microwave frequency.

By scanning through the strength of the magnetic field, points at which the sample absorbs microwave are recorded in accordance to Equation 3.2. Therefore, the g of absorbing substance is determined, allowing for the identification of defects. The technique was useful to pinpoint defects with differing gyromagnetic ratios and differing hyperfine couplings, allowing for precise identification of specific defects as detailed in section 3.2.5.1).

It is known that under specific experimental conditions, it is possible to accurately quantify the number of spins (thus impurity atoms) present within a sample. This is achieved by integrating the area under a given absorption curve, denoted as the double integral signal in the literature. [106].

Throughout all literature discussing EPR, the first derivative of the absorption is presented. This is related to the lock-in detection technique used to collect the absorption data, which enable the signal-to-noise ratio (SNR) to be low. All EPR data in this work are presented in this way, in accordance to what is reported in the literature.

3.2.5.1 EPR Experimental Procedure

The Bruker CW-EPR spectrometer with X-band excitation was used at the Faculty of Science NMR Facility to capture the Electron Paramagnetic Resonance (EPR) spectra of diamond samples. Each of the diamond samples was loaded into the resonator and centred manually. Single crystal samples were also made to orient with the magnetic field axis along the $\langle 100 \rangle$ direction. This minimizes the number of peaks which are known to appear in the EPR spectrum, and ensures the absorbing lines did not occur outside the central zone [106].

The EPR data were captured and analyzed using SpinCount software in the Xenon package (Bruker); simulations of the EPR spectra were accomplished utilizing EasySpin [107], which was modified to simulate details of our spectra, such as the misorientation of the sample in the magnetic field. An additional step was also completed to remove any background signal to allow for a more accurate quantification of the spin concentration in the samples. To complete this, a simulation of each defect on the EPR spectrum was created (N_s^0, NVH, NV^-) then these models were used to fit the background corrected spectra.

The magnetic field in the EPR spectrometer was calibrated by use of the HPHT diamond sample, as reference. This g-factor calibration assumes that the HPHT is dominated by N_s^0, which is a well-founded assumption [101, 108, 109] and does not affect quantification.

3.2.6 Imaging

Several well-known imaging techniques were used for qualitative analysis. Due to the varied nature of the information obtained by imaging (microscopy), there was less standardization in capture and less post-processing completed. Therefore, capture settings will be discussed in-line when needed.

Nonetheless, general methods used for the present work are summarized as follows:

Optical Microscopy Microscopy was completed across two main instruments. The first was a "3D microscope" (Zeiss Smartzoom 5), which allowed for magnifications of up to 1000x and Extended Depth of Field (EDF) images to be stitched across the field of view. EDF is a computational photography methodology which takes multiple images at differing focal planes and stitches them together to emulate a deep depth of field.

Since the 3D depth measurements were completed by the analysis of focus depths, it was not reliable for the transparent diamond. However, EDF imaging gave high quality images of surface texture over a large area.

The second microscope utilized was the Zeiss Axio Zoom V16, which is an upright general-purpose microscope. It was also used with coaxial illumination for successfully observing textures of diamond surfaces which are highly reflective.

Birefringence Imaging Birefringence is an optical property of materials, defined by the existence of orientation-dependent indices of refraction. As diamond has a cubic structure, it has four-fold symmetry, meaning all perpendicular axes are equivalent. This high level of symmetry means it is by definition isotropic. Therefore, any anisotropy found must result from imperfections in the lattice. The strains arising from imperfections can be spatially well defined (being 'point-like') or they can show up as general patterns. In the process of diamond classification, it is common to utilize birefringence to determine the quality of the solid. For example, the "tatami" pattern is commonly associated with type II diamonds [110, 111].

Birefringence is often related to the dislocation density of the diamond. These dislocations can begin at the epitaxial boundary layer if the surface of the diamond seed is not properly cleaned or is significantly damaged. Alternatively, extended defects can propagate from the seed into the synthesized surface. These defects present in the seed diamond will propagate with the grown surface, and do not terminate [66]. This means that the birefringence through the deposited direction is maximized, as the shift occurs throughout the entire length of growth.

Since these faults propagate from the underlying seed into the grown diamond, and there is an experimental need for diamonds without structural or optical aberrations, there has been significant interest in the reduction of these defects.

To solve epitaxial growth defects, considerable care was taken to clean diamond surfaces before deposition. This was completed in our experiment through careful chemical and plasma cleaning. Polishing would have enabled further control [57], but was not accomplished in this study.

The solution for propagating defects is more difficult, but solutions have been attempted, such as the growth of diamonds in orthogonal directions [112], use of substantial (40 ppm) nitrogen concentrations [113], and the growth of diamond over an empty cavity [58].

Procedure The Zeiss Axio Zoom V16 was used as a qualitative birefringence microscope, by using two crossed linear polarizers, optimized by observing the minimal brightness value of the surrounding field. Images with aligned polarizers were also taken for the sake of comparison. As all effects which shift the polarization are due to non-isotropic effects, we can relate them to imperfections within the diamond. Quantitative birefringence measurements were not attempted, but may be useful for future work.

Scanning Electron Microscopy (SEM) The Zeiss Gemini SEM 500 in uOttawa's CRPuO NanoFab was used to resolve growth features which are difficult to determine through optical means. Specifically, these are topographic features such as indications of growth nucleation and sub-micron etching features. The SEM is also useful for scaling features observed. Samples were secured to the platform by using carbon tape, for electrical conductivity and sample charging varied considerably across the samples. Parameters used for SEM imaging will be presented with images.

3.3 Defects

Defects are any alteration to the known repeating crystal structure. It has been said that "Unit cells are all alike, each defect is unalike in its own way" (adapted from [114]). This leads to a great variety of possible defects in solids which are classified into several families: point, line, planar, and bulk defects.

3.3.1 Point Defects

We will look at a limited number of common point defects. The naming systems for these point defects have historically been inconsistent depending on the characterization method used, hence the names stated here follow the example of Ashfold *et al.* [22]. This naming convention is based on the atomic structure of the defect and bracketed names are the 'common' names.

There are three major types of point defects which can be combined into defect complexes:
Vacancies — An absence of a native atom at the lattice site
Substitutions — A foreign atom taking the place of a native atom in the lattice
Interstitials — An atom situated between normal lattice points

In the diamond structure carbon is the native atom, meaning that atoms of similar sizes (e.g., nitrogen, boron) can substitute into the lattice easily. Larger atoms (e.g., silicon, germanium) will simply not fit in place of a carbon atom. For this reason, and because of natural abundance, the vast majority of defects known in the diamond lattice are nitrogen or boron based.

Nitrogen Defect Systems We will first look at the classic defects which were traditionally named A, B, and C labelled as such due to their likelihood of occurrence and of being detected (mainly through IR absorption) within natural diamonds. The atomic models of these classic defects are illustrated in Figure 3.3.

3.3.1.1 N_2^0 (A)

The conventionally named A-centre is a highly studied defect which commonly occurs within natural diamonds. This defect is uncommon in synthetic diamonds unless they are intentionally formed by annealing following their growth [111]. It is an easily identifiable defect given its intense characteristic light absorption in the one-phonon spectral range (1050–1330 cm^{-1}) and can be quantified through the measurement of intensity of its most intense peak (1282 cm^{-1}).

This defect is not active in EPR unless the diamond is irradiated during capture, which transforms the defect into N_2^+ [22].

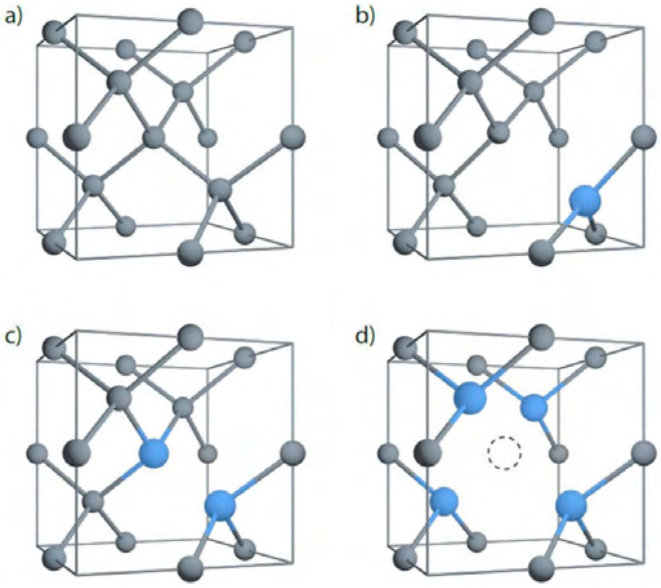

Figure 3.3: Atomic models of natural diamond and the three most common defects in natural diamond, all involving nitrogen (shown in blue) a) the diamond lattice b) the N_s (C-centre), c) the N_2^0 (A-centre), d) the N_4V^0 (B-centre). Reproduced from Ashfold *et al.* [22] with permission. Copyright 2020 American Chemical Society.

3.3.1.2 N_4V^0 (B)

The second most commonly occurring stable defect within natural diamond is a similar agglomeration to the previously described N_2^0, but is formed at higher temperatures. This defect is observed for most natural Ia diamonds and has a distinctive IR absorption feature in the one phonon spectral range. Hence this will overlap with the N_2^0 centre and most other nitrogen defect absorption bands.

This defect is also not active in EPR but can be quantified based upon the intensity of the infrared absorption based on the line at 1332 cm^{-1} [109].

3.3.1.3 N_s (C, P1)

For N_s the subscripted 's' stands for substitutional, and the defect occurs when a single nitrogen substitutes the carbon atom in the lattice. This is the most common defect which results from CVD and HPHT diamond synthesis, it is consequently a focus of our investigation. It shows an IR absorption band at 1344 cm^{-1} [115].

The neutral state N_s^0, is EPR active and is known in the literature as the P1 centre. When a nitrogen replaces a carbon, it forms bonds with the four neighbouring atoms, and the extra electron goes into a highly localized anti-bonding orbital directed along one of the bonds. Consequently, the spin of this localized electron can be sensed using EPR; this is an ideal candidate for quantitative EPR techniques.

An electron is gained across each of the bonds, meaning that a distinctive three-peak EPR signal arises from this defect if the magnetic field if oriented along $\langle 100 \rangle$, as shown in Figure 3.4.

3.3.1.4 NV

As discussed in section 1.1.2, this defect is of prime interest due to recent developments in magnetometry, quantum sensing and potential use in quantum information processing.

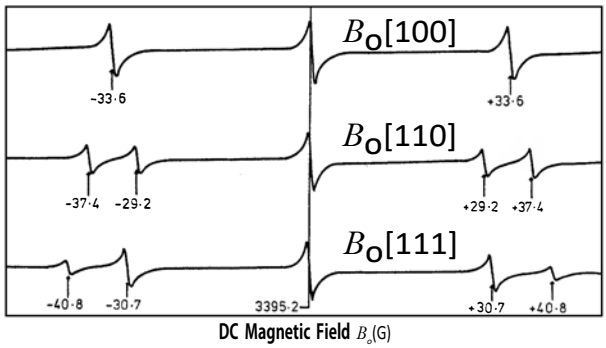

Figure 3.4: EPR signal recorded from a diamond with the B-field oriented along differing axes. Adapted from Loubser and Wyk [116] with permission.

The photoluminescence of the negatively charged centre has a ZPL centred around 637 nm when it is in its neutral spin state. This emission lies within an easily detectable portion of the optical range, with high absorptions and photoluminescence properties. Quantifying the concentration through these methods, however, has been difficult. Particularly, the absorption cross-sections are currently not agreed upon by differing groups - ranging an order of magnitude. Accurate schemes of detection and quantification have been proposed; but they have not been, however, standardized. See Chapman and Plakhotnik [117] and Santori *et al.* [118] for more details.

The NV^- defect system is part of the NV family, presenting a -, 0, or + charge state. These electronic states lead to the spin states of S = 0, 1/2, or 1 respectively. It is therefore expected that one will see an EPR interaction of the NV^0 state, although this has not been observed and is a topic of active research [119]. A quadrupole interaction of the NV^- due to its spin 1 nature is also observable. This means that spin concentrations within the normally studied in the g = 2.00 range would give a signal that is difficult to interpret and quantify. This means that a half-field measurement (g = 4.27) is useful to quantify NV^- concentrations. [120]

3.3.1.5 Silicon Vacancy - SiV^-

This defect is of relevance to what is covered in Chapter 4 and hence is discussed in detail at that point. The colour centre is known to occur commonly in CVD growths and is a split-vacancy system. The defect has a strong photoluminescence signal centred at 737 nm.

3.3.2 Structural Defects

Structural defects are imperfections in the crystalline network of the diamond. They are especially important for devices, as they tend to degrade the performance of the material.

Although planar and line defects are rare, the plane/line will not terminate properly during the CVD growth and hence can 'build up', especially if multiple growths occur on top of one another [121]. These faults often occur starting at the surface of the seeding crystal. It has been demonstrated that cleaning methods such as those reported in 2.4.6 lessen the impact of these defects. Significant work in the fabrication of electronic/quantum grade diamond has focused on the reduction of these structural faults, considered as undesirable [102].

Structural defects can be detected through several techniques, such as X-ray tomography, etch pit analysis, and SEM. Additionally, observing the width of the Raman line and performing birefringence measurements, as rough measures, have been useful for this purpose in our study.

3.4 Single Crystal Diamond Growth

3.4.1 Past Growths

The general procedures regarding growth were presented in chapter 2, along with a literature review which describes how individual parameters can affect diamond synthesis. For this study the experimental growth process was an iterative process, involving hypotheses about the effect of adjusting parameters and characterization to determine if these adjustments worked as predicted.

On the completion of any deposition, a report summarizing these characterization processes was completed, assessing the quality of the final diamond. Using the characterization results, suggestions were made to alter and improve the procedure.

Significant alterations resulting from this process were:

- Introduction of the sample holder pocket (2.4.3) to reduce the growth of PCD on the rim of diamond seed;
- Adjustment of overall pressure to increase the growth rate;
- Increase of the substrate temperature to decrease the α parameter and enhance the growth rate;
- Introduction of 'substrate height tracking' (2.4.4) to ensure consistent power delivery to the sample and a more consistent concentration of carbon-bearing radicals to the surface; and
- Introduction of a small amount of oxygen ($< 1\%$) during growth to increase crystalline quality and increase the α parameter.

3.4.2 Growth Procedures

After several iterations in tuning the parameters, a single crystal diamond of reasonably high quality was synthesized. This sample is named SCD-α. Although SCD-α has shown the attributes of high quality, further refinement of the growth parameters/process specific to our CVD system should lead to significant improvements.

For the sake of completeness, the parameters dialed-in to create SCD-α are listed as follows:

Diamond Seed A substrate synthesized by CVD was used. This seed's effect on growth will be discussed in the following section. The seed diamond had a size of 3.10 x 3.10 x 0.53 $\pm$0.01 mm and was acid etched (according to the recipe outlined in section 2.4.6) prior to being introduced into the CVD reactor. The face to be grown is a {100} plane and the top face has a roughness (P_q) of 30(5) nm as measured by profilometery. Measurements of birefringence (Figure 3.10a), Raman scattering (Figure 3.11a) and infrared absorption (Figure 3.12) will be presented and compared to post growth data below.

Pocket The seed (HPHT diamond) was placed inside a pocket (Figure 2.14) at the centre of a 3 mm thick molybdenum disk. The cutout has an overall depth of 1.30 mm and a bottom step of 0.4 mm (Figure 2.14). This optimizes the interaction of the diamond seed's top surface with the plasma, without a significant local enhancement at the diamond edges. The close bottom layer also enables an increased heat dissipation through its sides. The bottom step of the pocket was

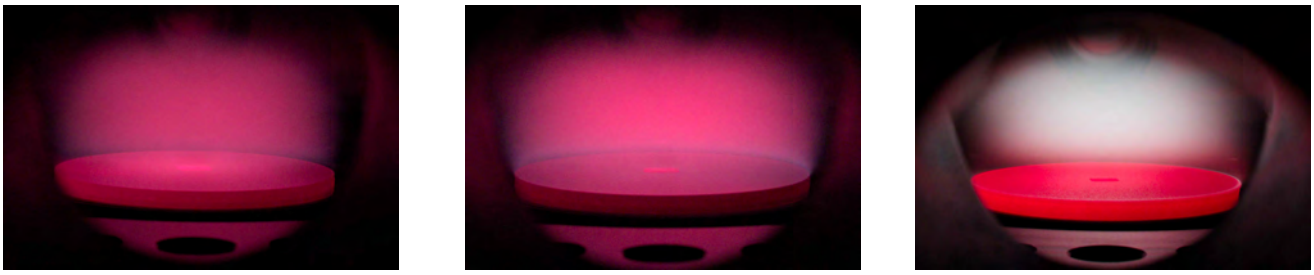

(a) (b) (c)

Figure 3.5: Photographs of the plasma during growth of SCD-α under differing conditions, captured through a narrow Hα/Hβ optical filter. For each photograph the exposure was modified to keep the pixels from overexposing. The growth plasma (containing methane and hydrogen) was approximately 10 times brighter than the pure hydrogen plasma. All plasmas had consistent temperature — 1000°C and total gas flow rate of 800 sccm. a) Hydrogen plasma for pre-etching of the substrate, 4 kW, 240 mbar 100% H_2 flowing. b) Hydrogen + Oxygen plasma for pre-etching of the substrate, 3.6 kW, 200 mbar 98% H_2 + 2% O_2 c) Growth plasma, 4.2 kW, 240 mbar 95.75% hydrogen, 4% methane and 0.25% oxygen.

3.2 mm in width, closely holding the 3.1 mm wide seed. The top cutout was 6 mm in width, allowing 1.4 mm of space between the seed and the edge cutout. This pocket had previously been used for one growth and therefore had been abrasive blasted and cleaned to remove the previous diamond film deposition.

Plasma Cleaning After placing the molybdenum disk into the CVD reaction chamber, a vacuum of 5.2×10^{-6} mbar was established, with a measured leak rate of 8.8×10^{-5} mbar/min (note: a low leak rate reduces nitrogen introduced during growth). A two-hour hydrogen-oxygen etch was completed (2% oxygen, 98% hydrogen, 200 mbar, 3.6 kW, 800 sccm, 1000°C) followed by a pure hydrogen etch of a half hour (100% hydrogen, 200 mbar, 3.6 kW, 800 sccm, 1000°C), prior to growth.

Growth Process A plasma was created with a hydrogen (95.75%), methane (4%) and oxygen (0.25%) mixture, these gases resulted in a total flow rate of 800 sccm. The methane gas was of 5 N purity (Messer, 99.999%). There should have been a baseline nitrogen content of 2.14 ppm in the gas phase due to methane (0.20 ppm) and the atmospheric leak rate (1.93 ppm). Since argon is used to control substrate temperature, minor additions of argon gas should be present inside the chamber, although no argon emissions were seen in the OES spectra of the plasma recorded during the deposition.

A constant pressure of 240 mbar with 4.2 kW was used to create the plasma. However, during the deposition, the volume of the plasma region drifted from 24 cm^3 to 30 cm^3. This led to a plasma density starting around 170 Wcm^{-3} and ending at 140 Wcm^{-3}. Large power densities such as these typically allow for rapid growth of the diamond, without a significant sacrifice of quality.

Note that as a side effect of the relatively high pressure used, the plasma region was approximately 4 cm in diameter, which is smaller than the 5 cm wide molybdenum disk (Figure 3.5c). This should not have affected the synthesis results for the SCD as our effective growth area, i.e., the seed pocket was small (6 mm) and is laterally centred on the molybdenum disk.

The substrate temperature was controlled to be 1000°C ± 20°C as measured by the two-colour optical pyrometer aimed at the diamond seed. Growth proceeded continuously for a period of 48 hours. During the deposition, the size and intensity of the plasma emission were monitored and

measured, allowing for substrate height tracking. Over the course of the growth, the substrate was moved in nine discrete steps to ensure plasma intensity uniformity (per section 2.4.4). This resulted in a displacement of 400 μm downwards as the diamond deposition proceeded. This correlated roughly with the measured height of the synthesized PCD. This was measured to be 440(10) μm with a micrometer and 370(4) μm in IR absorption.

The plasma volume changed—likely due to the substrate height tracking—therefore it is recommended for future runs that the pressure be adjusted to ensure constant plasma volume. This is recommended because the chamber pressure does not appear to affect growth conditions, while the plasma density is known to be an important variable.

Post-Growth Cleaning Immediately following deposition a pure two-hour hydrogen etch was completed, with the sample remaining inside the CVD reactor (100% hydrogen, 240 mbar, 4.2 kW, 800 sccm, 1000°C), to remove any remaining graphite from the surface. Upon the conclusion of the growth process, the sample was acid etched for two hours in a boiling nitric/sulphuric acid mixture, followed by a half hour of boiling in hydrochloric acid and finished by a half hour of room temperature *Aqua Regia*. Finally, the sample was ultrasonically rinsed for 15 minutes in both clean acetone and methanol. This process removed all measurable traces of the graphite from the sample, as determined afterwards by visual inspection and Raman spectroscopy.

3.5 Single Crystal Growth Characterization

Following growth, characterization of the sample's relevant physical properties could begin. This starts with a determination of the growth rate.

Weights and Measures The sample (i.e., the initial seed crystal) increased in weight from 17.623 mg to 39.978 mg corresponding to an added 0.1 carat. It increased in volume from 3.10 x 3.10 x 0.53 $\pm$0.01 mm to 3.80 x 3.80 x 1.04 $\pm$0.01 mm. Consequently, over 48 hours it had a growth rate of 10.6 μm/hr vertically and 7.3 μm/hr laterally.

Compared to results reported in the literature, this was significantly slower than high growth rate studies (>20 μmhr^{-1}) [30, 122, 123], but is higher than many studies on high quality diamond synthesis (5–8) μmhr^{-1} [37, 51, 73]. This therefore can be classified as a high growth rate, given the quality of the diamond obtained [45, 113].

3.5.1 Optical Microscopy

From microscopy following deposition (Figure 3.6), there was no PCD observed, as evidenced by a clear top surface. However, the surface morphology was not smooth and was asymmetric. This was primarily due to steps and step-bunching occurring. The particularities of the surface morphology will be explored below through the profilometery, 3D microscopy, and SEM results.

The side image in Figure 3.6c shows two growth regimes. The top half of the growth is clear, while the bottom half has blackened PCD. This could imply a shift in growth parameters during deposition. This may indicate a greater need for stability of conditions. One controllable parameter is the plasma density, as previously discussed.

A secondary difference in the side image is the height difference between the two sides of the growth. This is a difference of $\sim$80 μm. Profilometery corroborated by establishing a maximum height difference of 75$\pm$5 μm from edge to edge of the crystal.

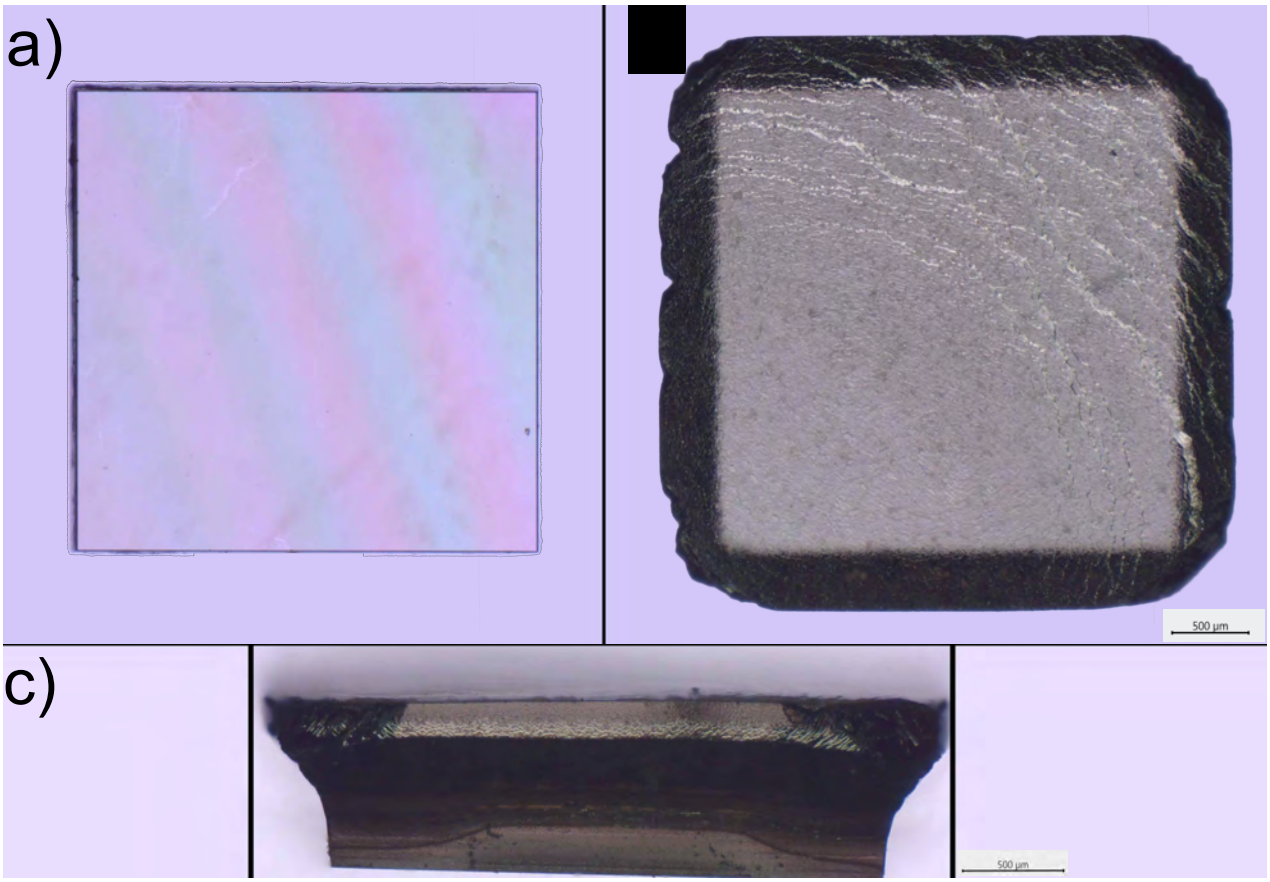

Figure 3.6: Optical microscopy of the SCD-α diamond, before (the seed crystal) (a) and after (b + c) overgrowth and etching. c) View of the overgrown diamond as seen from the side—the clear area on top is grown diamond.

Through the observation of dominant crystallographic faces in the final crystal (see Figure 3.6b, or 3.8), a determination of bulk crystallographic morphology can be made. Only the {100} + {111} faces survived. As seen in Figure 3.7, this gives bounds to the possible growth parameters of $3 > \alpha > 1$, $\beta < 3/2\alpha$ and $\gamma < 11\frac{\alpha}{3+2\alpha}$, Additionally, as pyramids are not observed, it can be understood they are overgrown by the {111} faces ($\alpha > 1.5$). Starting from a {100} cube it is not possible to determine values for β and γ, but they are in a 'desirable' range as they prevent {110} and {113} faces (see Table 2.1).

Growth rates of the faces were measured and the α parameter is measured to be 2.05±0.2 for this deposition. This confirms that α is in a desirable range, disallowing the possibility of pyramidal growths while ensuring the corners do not dominate the usable surface.

Further depositions should attempt to maintain these growth parameters, although a minor reduction in α could be beneficial, as it would lead to a larger usable surface area.

3.5.2 Surface Morphology - Scanning Electron Microscopy (SEM)/3D Imaging

The image captured by the 3D microscope shows two undesirable surface topologies. These are steps bunching and terraces. These growth types, although unwanted are nonetheless consistent with surface growth in the ⟨100⟩ direction. This is important as growth in certain crystallographic directions incorporate varying quantities of defects: {100} is known to incorporate a low number

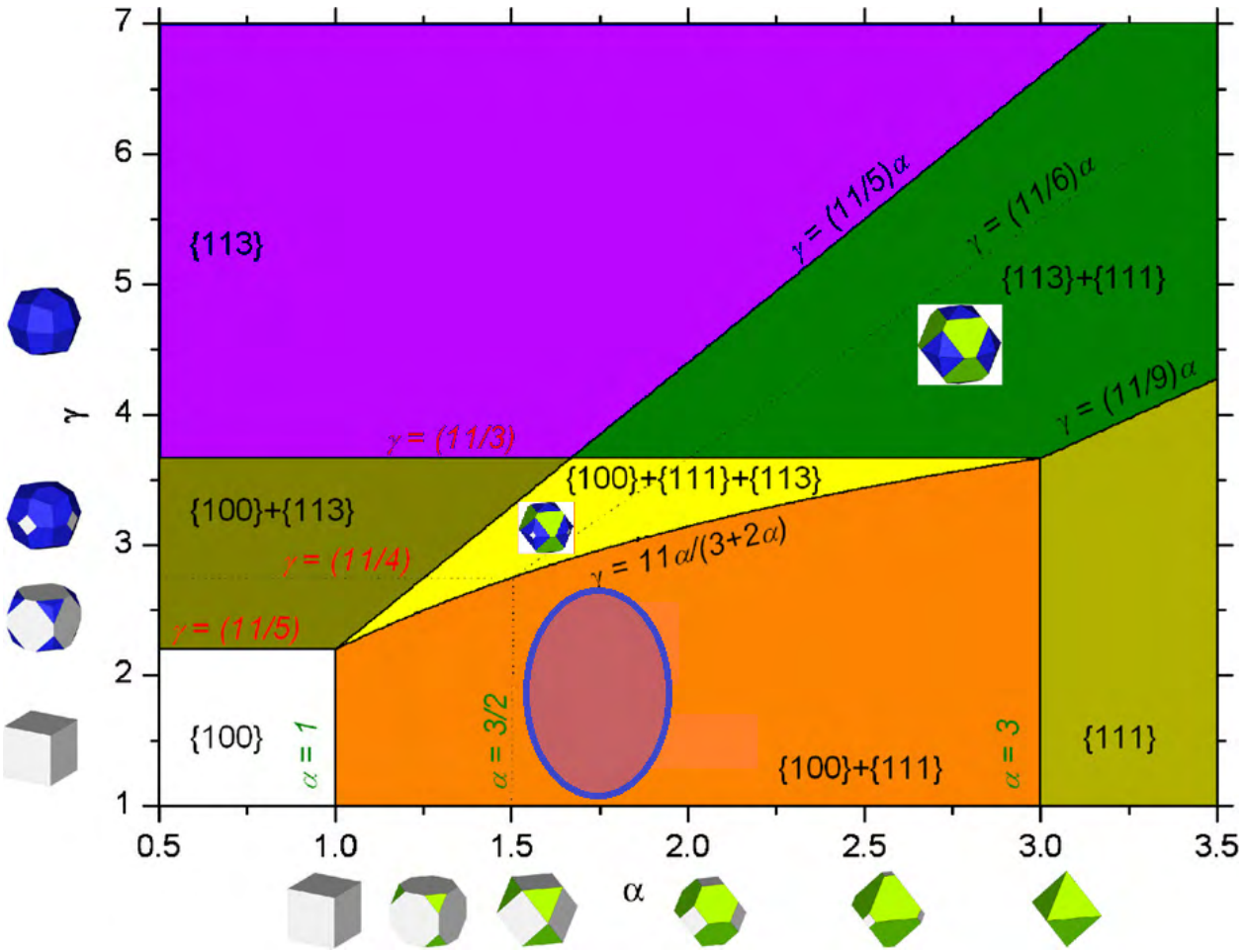

Figure 3.7: Bulk morphology phase diagram of diamond showing the growth region. The blue ellipse indicates the current growth for SCD-α, β is omitted in this graph as 110 faces do not occur, implying that $\beta < \frac{2}{3}\alpha$. Modified from Silva *et al.* [48] with permission.

of defects during CVD synthesis [22, 124].

Step bunching and plateaus are non-desirable due to their correlations with lower quality diamond growth [110]. It practically causes an uneven vertical growth height as previously observed. This would leave less vertical diamond after polishing.

A higher misorientation angle (section 2.6) has been shown to lead to a smoother and higher quality surface morphology. However, misorientation was not measured. The existence of plateaus strongly indicate a low angle [14]. For further work with high-quality SCD synthesis, it is suggested that the measurement of misorientation be completed and possibly use of samples with an off-axis polish.

SEM imaging as shown in Figure 3.9 allowed for more detailed capture of the previously mentioned growth modes—stepwise (Fig. 3.9a, 3.9b) and terraces (Fig. 3.9d).

Imaging with SEM allowed for the observation of an additional feature; the etch pits (Fig. 3.9c). These are seen to occur in sizes ranging from 100–300 nm and are likely caused by strong plasma etching, significantly enhanced by the added oxygen. Their creation should allow for higher crystal quality, with fewer structural and impurity-related defects. This is because the defects are weaker than the native diamond lattice. Enhanced etching also competes with growth, reducing the growth rate.

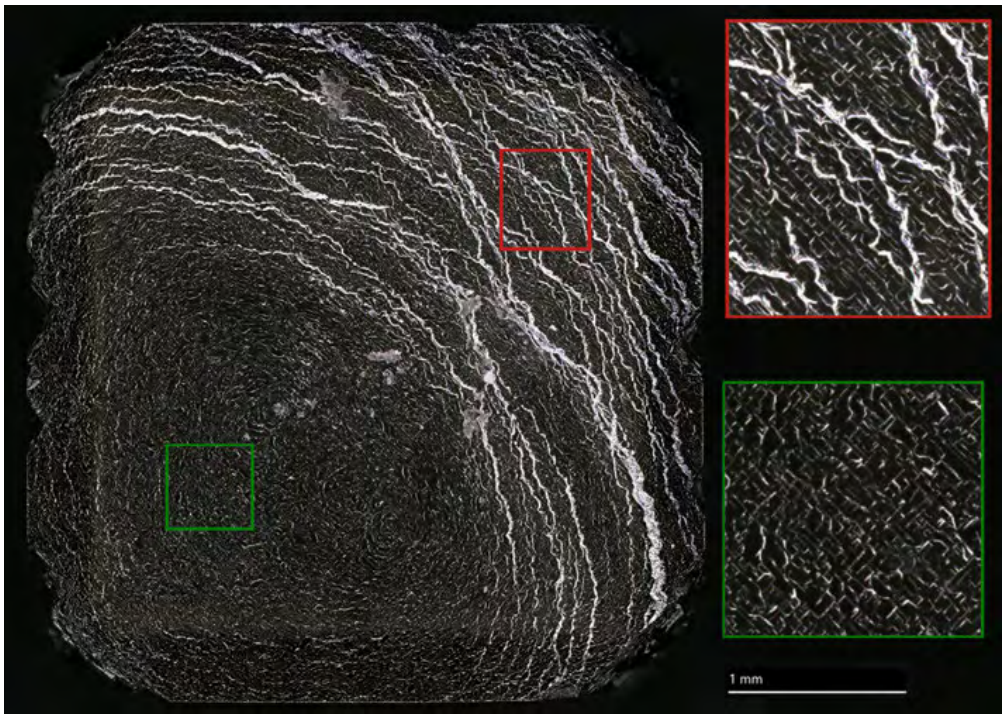

Figure 3.8: Image completed of SCD-α with the 3D microscope, which uses EDF and stitching to give a broad picture of microscopic surface morphologies. Cutouts show two selected regions of interest that are representative of the sample areas. These are the plateau in the green cutout and the stepwise area in the red cutout.

Birefringent Imaging Birefringence images were taken of the diamond seed (Figure 3.10a) and the post-growth sample (3.10b). Recall that this measurement is a qualitative determination of residual strain or asymmetric characteristics within the sample and this measurement is sensitive to low levels of strain [125].

The seed's birefringence pattern was not clearly replicated upon the grown diamond, indicating that the grown diamond had significant localized internal strains which were independent of the underlying seed. A high quality diamond would be entirely dark, as it would not alter the incoming linearly polarized light. It is hypothesized that these strains are correlated with the step bunching process, as the more birefringent areas correlate with the more bunched areas.

Additionally, by observing the side profile (Figure 3.6c) it was seen that the strain is vertically uniform throughout the grown diamond, indicating that it was a growth effect.

As cutting and polishing was not completed for this sample, it is also possible that these reported effects are limited to the diamond surface. It is therefore recommended that diamond cutting and polishing facilities be created/utilized for future growths. It is known that due to diamond's unique hardness, both of these facilities are non-trivial to create.

Photo-induced Emission Fundamentally, for a given stimulating wavelength, Raman scattering (Stokes) and photoluminescence have overlapped emissions. However, in high purity diamond, the common impurities and defects can be determined and lines from the two effects can be distinguished.

We are primarily interested in comparing diamond in the grown region and the seed, but for reference and context, two additional samples will be included in the graphs. The first sample for comparison used to represent the objective of the growth: high quality. This sample was a high quality (IIas - Supplier: Almax-EasyLab Inc. Grower: unknown) diamond which was particularly

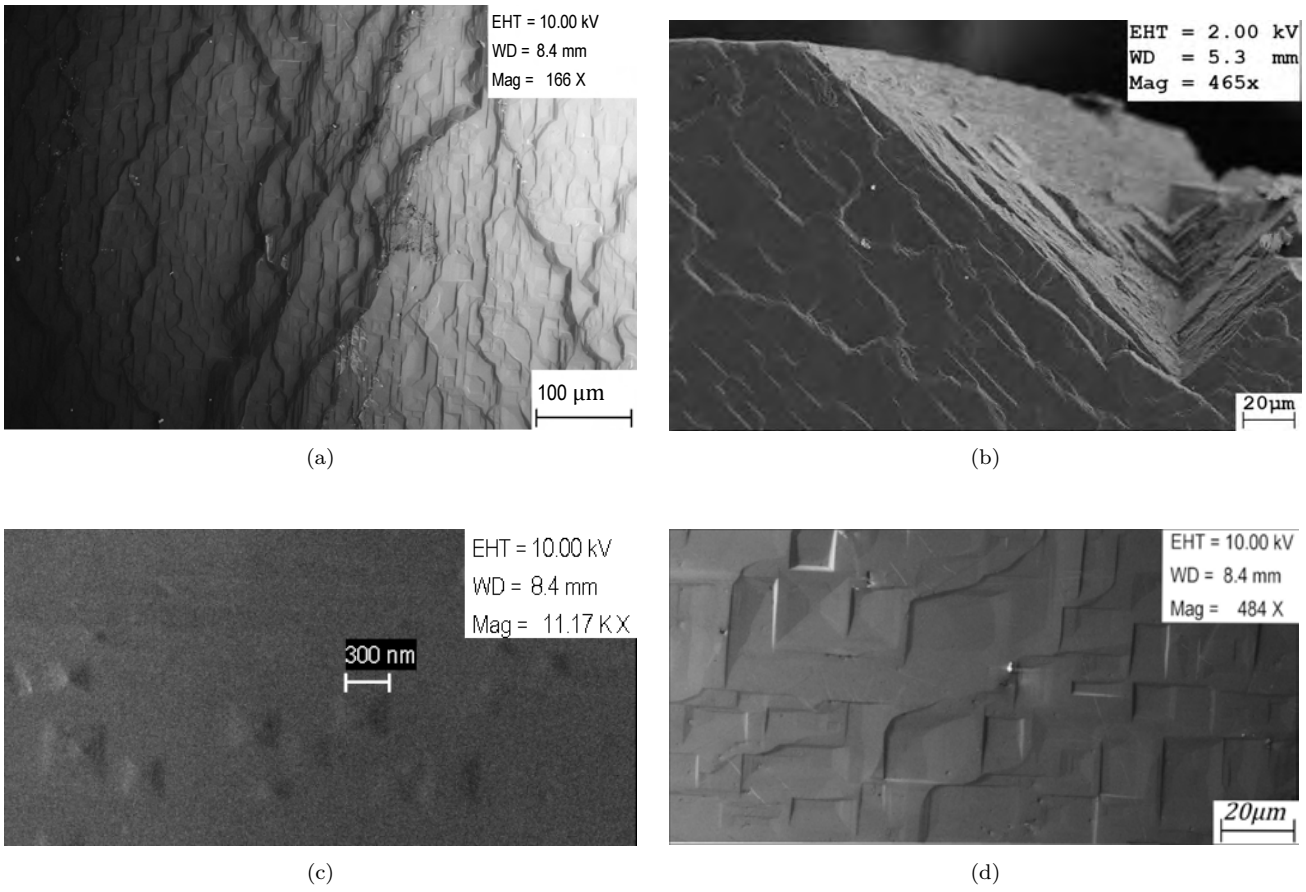

Figure 3.9: Several growth morphologies which exist upon SCD-α a) Stepwise growth b) Stepwise growth on the diamond corner c) Etch pits d) Growth plateaus. Images obtained by SEM.

grown and sold for its ultra-low birefringence and ultra-low luminescence. For additional comparison, the results from a lower quality diamond will also be included in the graphs. This sample was the heteroepitaxial PCD co-grown with the SCD; PCD intrinsically has a lower crystalline quality and present a larger number of defects. Further discussion of PCD is found in section 4.1.3.

3.5.3 Raman Spectroscopy

The Raman scattering emissions of note are from diamond and graphite in the range of 800-1600 cm^{-1}. The graphite lines (1355 cm^{-1}, 1500 cm^{-1}, and 1620 cm^{-1}) were useful in determining low quality growth and/or un-etched deposition early in the growth optimization process. However, after acid etching, it was determined that none of these samples have graphite, therefore only the diamond one phonon Raman line is of note. This is a one-phonon peak commonly known as the 'diamond' line and is shown in Figure 3.11a. Uncertainties related to linewidth are ± 0.05 cm^{-1} while line positions are ± 0.1 cm^{-1}.

The spectral characteristics of the Raman line are useful in serving as an indicator of diamond quality. As presented in section 3.2.4.1, both the position (Raman shift or wavenumber) and linewidth are of interest. The linewidth is correlated with overall quality; with this in mind the diamond noted as the "anvil" has a width of 1.63 cm $^{-1}$. This value designates it the highest quality diamond possible to characterize through the measurement of the diamond line [30, 73,

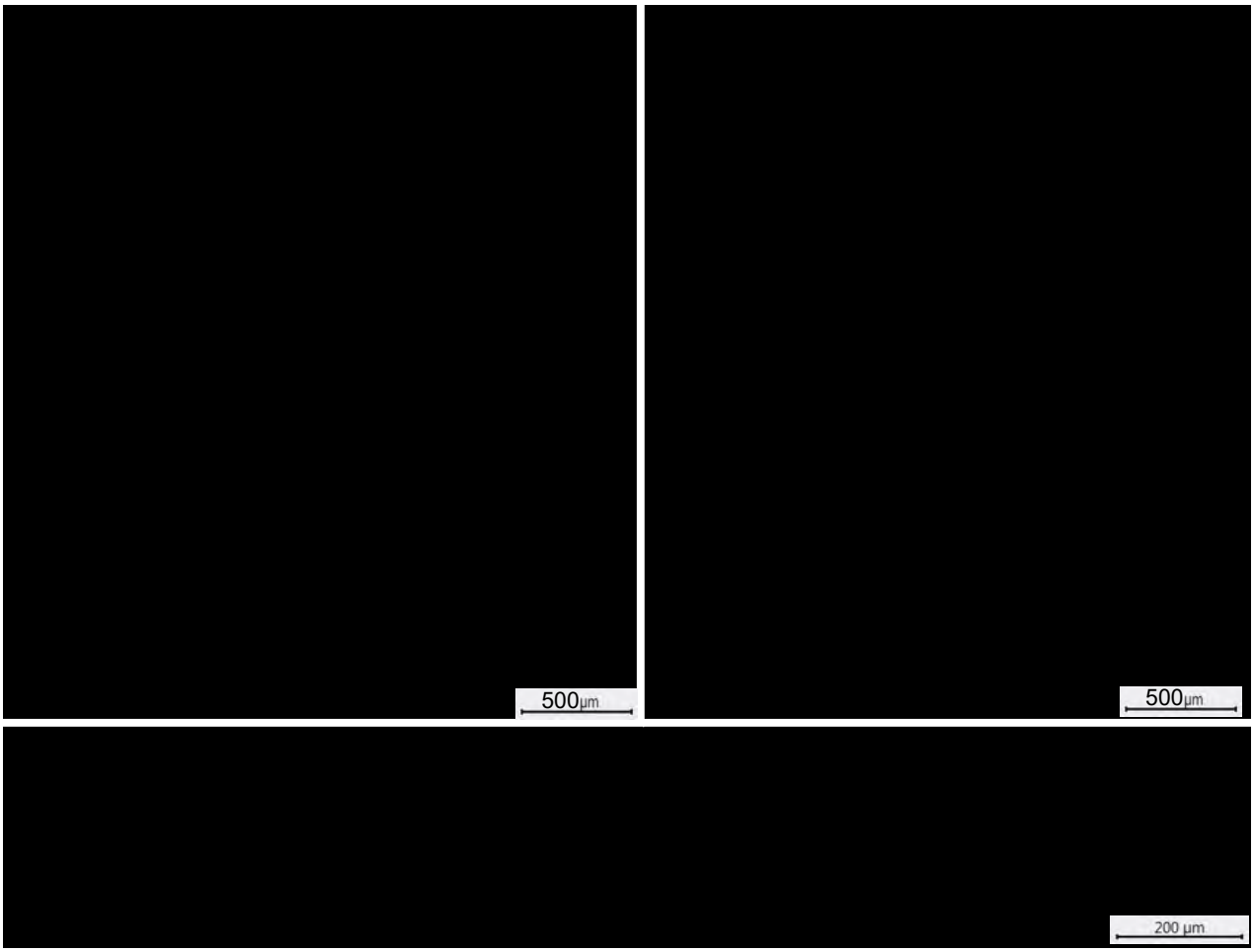

Figure 3.10: Optical microscopy of the SCD-α diamond under crossed linear polarizers, before (seed) (a) and after (b + c) growth on top of the seed and etching. c) View of the diamond from the side. The images show diamond birefringence.

126]. In comparison the seed and grown diamond represent lower qualities. But any diamond with a width under ~ 2 cm^{-1} is, however, considered of higher quality than the majority of natural IIa diamonds [127]. With this considered, it can be noted in the present case that the grown diamond SCD-α is of higher crystalline quality than its commercially purchased seed and can be considered 'high quality'.

Based on the Raman line, the low quality of the PCD as compared to SCD obtained during the same growth under the same conditions shows the downsides of heteroepitaxial growth. It inherently produces a lower crystalline quality and shows a higher concentration of impurities due to its randomly oriented growth and small crystallites.

The shift of the Raman line from the nominal position can be caused by several factors: the most likely is the presence of residual stress within the sample. This anisotropic strain stress the Raman line at a rate of:

$$Stress = 0.34 \ \frac{GPa}{cm^{-1}} \times \Delta\nu \qquad where \quad \Delta\nu = \nu - \ 1331.8 \ cm^{-1} \tag{3.3}$$

We find that the seed and grown diamond have internal strains resulting from a compressive stress of approximately 0.3 GPa.

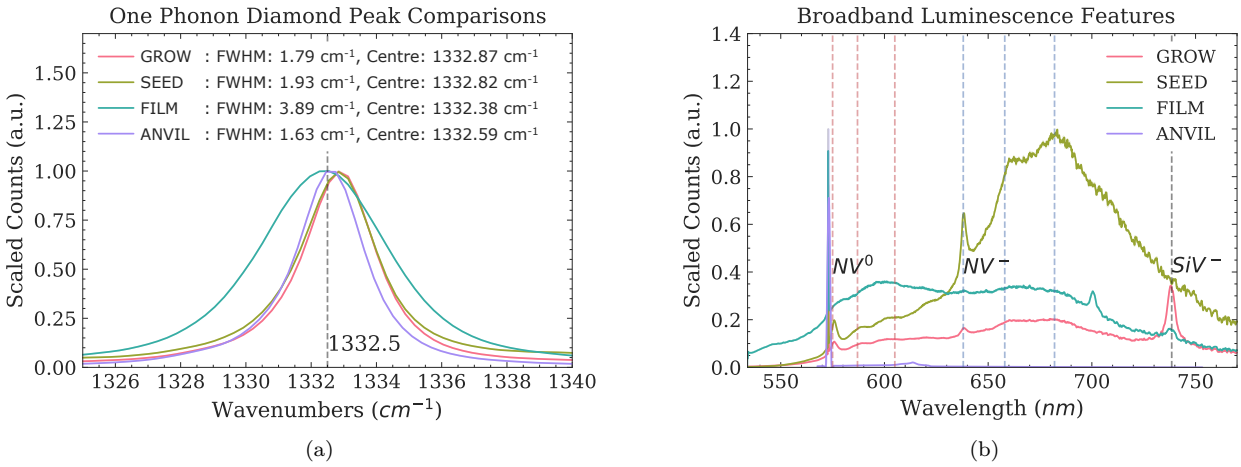

Figure 3.11: Raman and photoluminescence spectra recorded from the SCD-α and reference samples as excited by a 532 nm laser. Three parts of the sample are compared. The grown segment labelled 'GROW', the homoepitaxial seed (SEED) and the PCD film (FILM). Additionally, a high quality IIas diamond is graphed for comparison (ANVIL, used as a reference). Both Raman and photoluminescence are seen. a) Focus on the diamond one phonon Raman line, which gives a good indication of the overall crystalline high quality. b) A broadband spectrum, with significant luminescent contributions from various colour centres, superimposing the Raman lines.

Single substitutional nitrogen (N_s^0) is also known to shift the line to higher wavenumbers, but the shift is too large to be accounted for by this effect [101] based on the EPR and FTIR spectra, which is presented below.

The Raman line downshift of the film was possibly due to local heating from laser illumination. If this were the case, it would correlate to an increase of 7°C if the Raman peak shifted from 1332.5 cm^{-1} or 20°C from 1332.8 cm^{-1} [101].

The grown diamond is shown to have a high level of crystalline quality, improving upon the homoepitaxial seed's quality, as desired. Further optimizations of growth should allow for further improvements. It is hypothesized that the primary broadening factor is internal strain due to step bunching.

3.5.4 Photoluminescence

The PL signal primarily arises from fluorescent colour centres. As seen in Figure 3.11b, the major colour centres which are embedded in the characterized diamonds have been identified. For these diamonds, they are the two nitrogen vacancies NV^0 and NV$^-$ found with zero phonon lines at 575 nm, and 637 nm, respectively. Both of these have large PSB which is indicated in Figure 3.11b.

In the seed, PCD and grown diamond, large photoluminescence signatures are seen. The ratio of NV^0 as compared to NV$^-$ changes relative to the local charge environment, but the strength of these signatures is indicative of an unintentional and uncontrolled nitrogen source.

The intensity of this signature is generally not used as a quantitative gauge of nitrogen content in the diamond. However, Yamada *et al.* [74] have seen a relationship between the NV^0 photoluminecence intensity and mass spectroscopy (secondary ion mass spectroscopy) measurements of nitrogen. Using their relationship, we can estimate that the overall nitrogen content in the diamond is ~2 ppm ($4\times10^{17} cm^{-3}$). This result agrees with the EPR results as presented below. But

it should be noted that local charge environment and growth conditions could affect this signal significantly, independent of nitrogen content. Further work should be completed to identify sources and reduce nitrogen content in the growth chamber to the lowest possible level.

The IIas anvil does not have any significant PL signal, either indicating a post-treatment was done to reduce any causes of PL or a strong control of unintentional nitrogen was accomplished during growth. In section 3.5.5, evidence for photoluminescence compensation methods is found.

The final photoluminescence signal found in our spectra is that of the SiV^- defect. This colour centre has a ZPL centred at 737 nm: it is only seen in the grown samples. This defect is caused by silicon from previous growth, etched quartz windows and an o-ring (FKM per manufacturer) attacked by the plasma. This defect is of interest to this work and therefore efforts to reduce its inclusion was not pursued. The motivation to study the SiV^- defect is further explored in appendix 4.

Significant nitrogen-related PL signals are measured, with larger quantities than would be expected from the known quantity of nitrogen in the chamber. The reduction of nitrogen and silicon in the diamond should be a priority for following CVD growths.

3.5.5 Fourier Transform Infrared Spectroscopy(FTIR)

The infrared absorption spectra, as captured through Fourier Transform Infrared Spectroscopy (FTIR) can give strong and accurate determinations of certain defects. It is commonly used in diamond grading and can give some information around growth orientation along with the information about incorporated defects.

As with the Raman/PL spectra, the seed and grown diamonds are analyzed alongside with two other samples for reference. The first reference sample is the same IIas diamond used above, but for the low quality comparison, a secondary reference is used. This bulk Ia diamond was chosen over a PCD sample since as-grown thin sections encounter significant thin film interference and scattering. This will be further explored in appendix A.

The IR spectra can be divided into three regions, based on the phonon spectral ranges. The one phonon region (< 1332 cm^{-1}, Figure 3.12b) is interesting as the diamond has no intrinsic dipole moment, consequently, it is intrinsically non-absorbing throughout this region. It is ideal for investigation of many defects, with several notable nitrogen-related defects.

This is evidenced by the 'ANVIL' Ia sample and the 'SEED' sample. Each has active nitrogen defects within this region. Within the Ia diamond, these can be identified as N_2^0 (A) at 1282 cm^{-1} and N_4V° (B) at 1332 cm^{-1} defects, at quantities of 350 ± 40 ppm and 270 ± 70 ppm respectively.

The seed diamond has one broad line in the one phonon region which correlates best with the N_s^+ defect at 1046 cm^{-1}. The defect is difficult to quantify as the sharp, but weak line used for quantification (located at 1332 cm^{-1}) is weaker than the interference fringes. It can be roughly quantified to be < 0.5 ppm ($9\times10^{16}\,cm^{-3}$) [128].

The existence of substitutional nitrogen is expected, as it is the most common defect within CVD synthesized diamond, but they are generally neutral. The positive charge of these defects, along with the relative strength of the NV^- as compared to NV^0 luminescence in the PL spectra, indicate that a significant quantity of the substitutional nitrogen atoms have donated their electrons to the NV^- centres, as has been observed in the literature [128].

For the grown diamond, no defects are visible from the IR spectrum. However, as this was a non-annealed CVD grown diamond, it is known that there is a non-zero quantity of substitutional nitrogen. From our graph we can determine that there is <0.74 ppm ($1.3\times10^{17}\,cm^{-3}$) of N_s^0 - per Section 3.3.1.3.

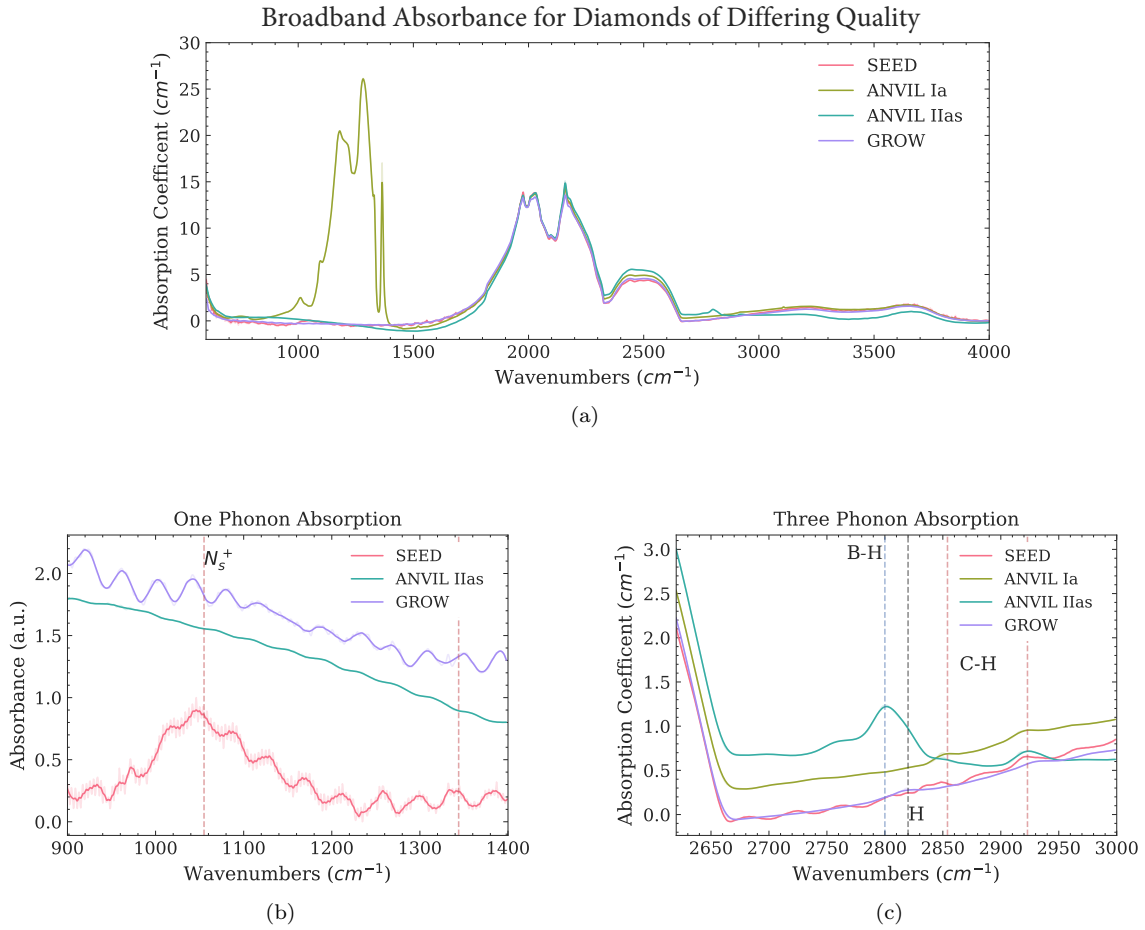

Figure 3.12: IR spectra captured of the SCD-α sample and references using the FTIR technique. a) Broad spectra of the mid-IR range b) Narrow focus upon the one phonon containing region of the spectra, which mainly contains nitrogen defects. c) Focus upon the three-phonon region, vertical lines designate various defects, blue lines are boron, black are hydrogen terminations and red are C-H stretch bonds.

The two-phonon region however (1600-2666 cm^{-1}) has a strong and consistent intrinsic absorption profile, which can be seen to be similar through all the samples (see Figure 3.12a).

The three-phonon region is the final region visible in the spectra and shows various lines. For these samples, the region above 3000 cm^{-1} only includes the two broad intrinsic diamond lines.

In this region there are three types of lines detected across the samples. The first is a C-H stretch doublet (2854 cm^{-1}, 2923 cm^{-1}), which only occurs on the 111 faces [129], the natural Ia diamond and synthetic IIas diamond show evidence of this growth mode.

The next is the H-termination detected at 2820 cm^{-1} [130], which may indicate lower quality diamond on the face of the grown diamond. Cutting and polishing would be required to ensure that this is not a surface effect.

The third line detected is the B-H line, which is only seen in the IIas anvil. This is likely an intentional dopant to add holes to the diamond to passivate luminescent defects such as the NV^- and N_s^0. By taking this line and integrating it, we can determine that the concentration of uncompensated boron is 0.17(5) ppm ($3\times10^{16}\,cm^{-3}$) [101].

Overall, the FTIR spectrum indicates that the grown diamond has low (<1 ppm) amounts of nitrogen in its most common form and no evidence of boron defects, meaning it can be classified as

a IIa diamond. Additionally, it is proven that it grew in the desired ⟨100⟩ direction, with evidence of surface hydrogen defects which should be polished or cut away.

3.5.6 Electron Paramagnetic Resonance (EPR)

The EPR signal captured from SCD-α is shown in Figure 3.13. The grown sample was not cut off the seed; hence the signal obtained is a combination of the two diamond layers. Unfortunately, although data were captured from the seed before growth, it was captured with a saturated signal, preventing a quantification and accurate comparison. As an alternative, a comparison of the grown sample with two similar seeds are completed (one is pictured).

The paramagnetic defects which dominate the signal are the same for the seed as for the grown sample. These significant defects are N_s^0, NVH^- and H-termination which account for approximately 60%, 20% and 15% of the known signal respectively. These can then be quantified at a rate of 1.5 ppm ($2.7{\times}10^{17} cm^{-3}$) of N_s^0, 0.5 ppm ($6.0{\times}10^{16} cm^{-3}$) of NVH^- and 0.3 ppm ($3.6{\times}10^{16} cm^{-3}$) of H-terminations.

These defects are expected and common, arising from unintentional nitrogen incorporation and hydrogen etching during growth. These are common defects seen in the majority of CVD samples [108, 131]. No neutral silicon vacancy was detected, which is consistent with the findings in PL. Unfortunately, SiV^- has not been found to be EPR active [108], so quantification of it is difficult.

In previous EPR spectra, additional defects could clearly be seen above the seeds' baseline, but this was not observed to be the case for this sample. It is very likely that many of these detected defects occurred from the growth. But, distinguishing the two signals is not possible with the current procedure. This indicates higher quality as compared to previous growths, but also indicates the need for a detachment of the grown sample from the seed to determine defect concentrations accurately.

Based on these measurements, we can place an upper bound on the defect. Therefore, we can state that there is a concentration of <2.0 ppm ($3.6{\times}10^{17}\, cm^{-3}$) of nitrogen-related defects. This cautious upper bound still allows for the classification of the grown sample as a IIa diamond.

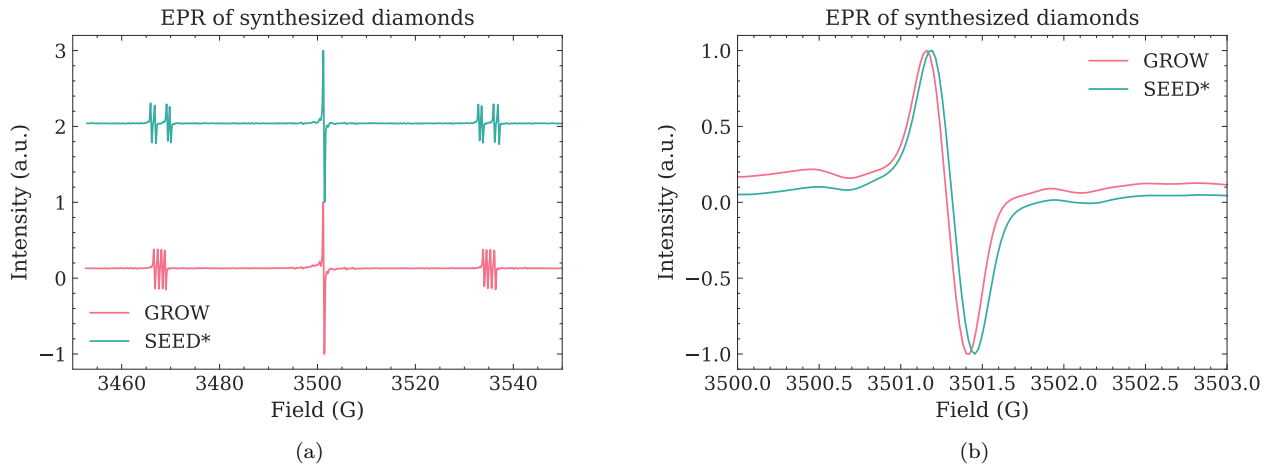

Figure 3.13: EPR derivative data captured of the SCD-α sample with a power of 0.2 μW at a frequency of 9.712 GHz. Graphs show a visual comparison of the seed and grown diamond. Note that the seed is a similar seed, and not the seed used for growth. a) Broad spectra of the diamond signal b) Narrow focus upon the central g=2.0023 region of the spectra.

3.5.7 Discussion

Overall, the diamond synthesized is of high quality and would be classified as a IIa diamond due to its found defect quantity. Additionally, its crystalline quality has been found to be relatively high with a Raman linewidth of 1.8 cm^{-1}. Despite this, it has a significant number of photoluminescing defects. Both PL and EPR measures of nitrogen content give a similar rough estimate measurement of defects concentrations at $\sim$ 2.0 ppm ($4{\times}10^{17}\,cm^{-3}$).

According to the measurements of Tallaire *et al.* [73], a solid-state concentration of 2 ppm of nitrogen would correlate with a gas phase concentration of 100 ppm. This is two orders of magnitude more than the known gas phase nitrogen content of 2.14 ppm of our supplied gases. This indicates a large leak into the chamber of unknown origin (leak of $4{\times}10^{-3}\,mbar/min$ or 0.1 sccm, compared to a measured rate of $9{\times}10^{-5} mbar/min$ or 0.002 sccm). More investigation is required to identify the source of nitrogen and alleviate its incorporation in diamond during growth to improve quality.

Due to this large nitrogen defect quantity, the sample cannot be classified, unfortunately, as 'quantum' or 'electronic' grade. If the unintentional source were found, a gas phase nitrogen content of 2 ppm could be achieved and a crystalline nitrogen content in the ppb ($10^{14}\,cm^{-3}$) range [73] should be achievable.

The source of the growth height inhomogeneity was not determined. Further investigation of the reactor and pocket conditions are likely needed to determine the cause and address it.

3.6 Future Work

The following are several recommendations to improve the quality of the diamond in future growth in our CVD system.

As discussed above, the most significant improvement would be the reduction of foreign atoms into the lattice, specifically nitrogen. The reduction of nitrogen would likely result in marked improvements in quality. However, it is important to monitor the α parameter while completing this, as a reduction of nitrogen decreases α, and care must be taken to ensure the growth parameter (currently 2.05 ± 0.2) does not reduce below 1.5.

The use of diamond seeds polished with a misorientation angle also has the potential to increase the quality of the surface morphologies, specifically reducing step bunching and increasing step-flow growth modes. The resolution of this could additionally improve stress in the sample.

A further improvement would be to ensure a consistent power density on the surface throughout the growth process. Inconsistent power density is likely caused by the changing substrate height due to heteroepitaxial PCD growth. This effect could be compensated for by increasing pressure as growth parameters are not affected by chamber pressure, but pressure changes power density.

Cutting and polishing of the grown diamond layer would allow for accurate determination of defects through EPR and would additionally allow for the disentanglement of surface effects from effects in the bulk material in FTIR, Raman spectroscopy, and birefringence imaging.

Chapter 4

The Silicon Vacancy under Extreme Conditions

4.1 Diamond Photonic Defects

Currently, diamond photonics is a field built up around the NV^- centre. As described in section 3.3.1.4, this well-known defect in diamond allows for experimental access to a long-lifetime, solid-state qubit state without cryogenic temperatures.

Despite its favourable qualities which enable easy interfacing, the NV^- centre has several undesirable properties, specifically related to its optical characteristics. These shortcomings are a low quantum efficiency, a large spectral extent, and a low Debye-Waller factor. All of these factors prohibit the deployment of NV^- centres in contexts which require the quantum information to be written and read out reliably from the centre embedded in a diamond network.

The most extensively studied alternative to the NV^- centre is the negatively charged silicon vacancy defect (SiV^-). It was first observed in the mid-1990s [101, 132], but was not considered at the time to be a possible photonic platform. Its utility was not recognized until the groundbreaking investigation led by Neu *et al.* [133] in 2011. This study showed the favourable optical characteristics of the SiV^- defect: narrow linewidth (0.7 nm at 30K) and high quantum conversion efficiency (88%). Following this study, the SiV^- defect quickly became a focus of intense research [134–139], establishing SiV^- as a colour centre with advantageous qualities for quantum technology. Based upon these characteristics, the SiV^- defect has shown promise as a high sensitivity quantum sensor, single photon source, and qubit [140]. Unfortunately, the SiV^- centre is an intrinsically more complex quantum system than the NV^- centre and requires cryogenic temperatures to reveal the useful spin-based interactions. In this work, we will investigate the utility of the SiV^- centre as a sensor for extreme conditions research by studying its photoluminescence characteristics at high pressures and low temperatures.

4.1.1 Group IV Colour Centres

The silicon vacancy (SiV) belongs to a family of defects commonly known as the group IV colour centres. It is aptly named, as all stable elements in group IV (group 14) have been shown to form an interstitial defect with the same structure. The negatively charged variants are SiV^-, GeV^-, SnV^-, and PbV^-, they were discovered in 2011, 2015, 2017, and 2018 [133, 141–143], respectively.

These defects are arranged equivalently in the diamond lattice. Each foreign atom is significantly larger than an atom of carbon, so they move into the interstitial position, situating

themselves between two neighbouring vacancies. The commonly accepted nomenclature for this type of defect is XV (X=foreign atom), but a more evocative label may have been VXV. Figure 4.1 shows an example of the XV defect's structure.

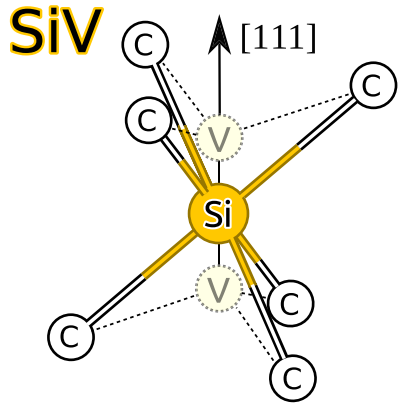

Figure 4.1: Crystalline structure of a group IV colour centre in the diamond lattice, with native carbon atoms and vacancies represented by C and V, respectively. Reproduced from Thiering and Gali [144] with permission.

With this physical configuration, the centres have threefold rotational symmetry along the diamond $\langle 111 \rangle$ direction, similar to the configuration of the NV^- centre (C_{3v}). Additionally, due to the interstitial position of the foreign atom, they also exhibit inversion symmetry (D_{3d}). This is of considerable consequence, as the static dipole moment is suppressed leading to a significant decrease in sensitivity with respect to any electrical field interference [145]. Specifically, it has no first-order Stark shift (electrical field response). This in turn directly leads to the protection of the colour centre from proximate charges in the diamond and greatly reduces its spectral extent. For a detailed discussion of symmetries for the SiV centre, refer to Hepp [136].

The energy level diagram of the group IV defects is shown in Figure 4.2. It differs from the energy level structure of the NV^- centre (Figure 1.2b) in several ways. The most significant difference is the appearance of ground state zero field splitting, as a spin-orbit splitting exists for both ground and excited states. This means that four distinct optical transitions emerge for B = 0. At low temperatures (<40K), in diamonds with low strain, all of these transitions are observable within the photoluminescence signal. These optical transitions are shown in Figure 4.2, and are conventionally labelled as A-D based upon the wavelengths of their corresponding lines.

4.1.2 Silicon Vacancy - SiV^-

While all group IV defects share common properties, the SiV^- has been the most intensely studied. This is largely due to the ease of experimental fabrication (see section 4.1.3). Furthermore, it has been determined that the zero phonon line (ZPL)—appearing at 738 nm—has a high level of photon conversion efficiency, allowing 70% of the photoluminescence to be concentrated in the ZPL at room temperature (RT). Additionally, without linear Stark shifts, the linewidth of the defect is relatively narrow (6 nm at RT). Enabled by these properties, indistinguishable quantum emitters from separate SiV^- centres have been manufactured [146].

While the SiV^- centre is largely unaffected by local charges, it is not, however, immune to strain in the diamond lattice [135, 147]; thus the study of lattice strain's effect on the centre has

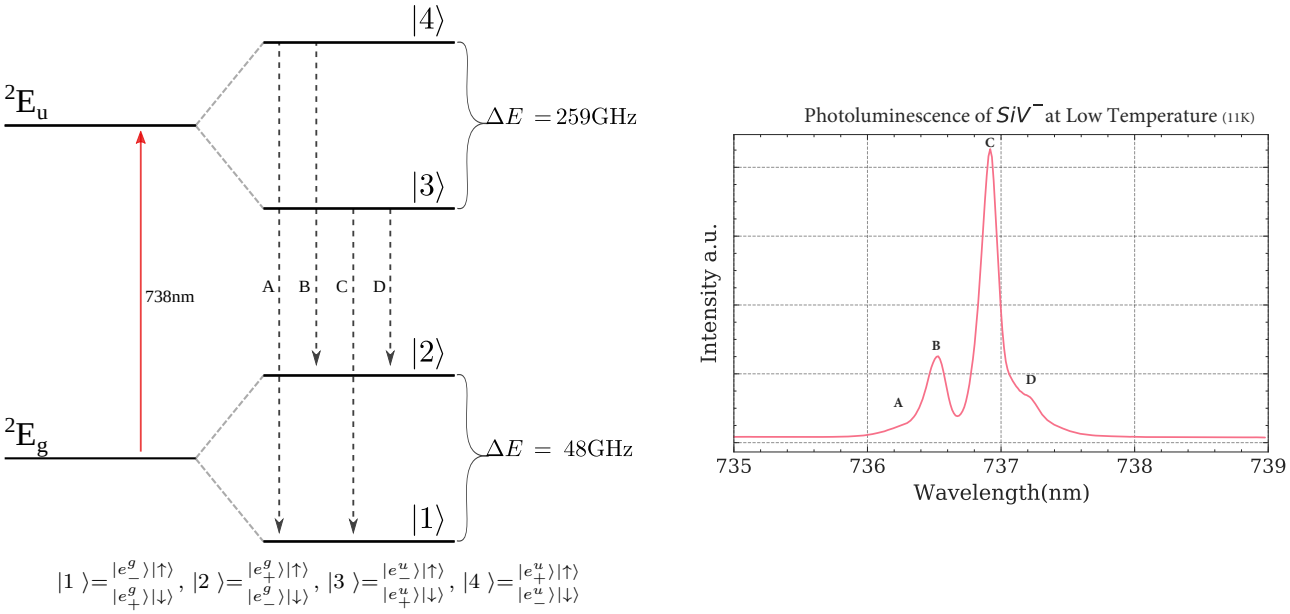

Figure 4.2: (left panel) The energy level diagram indicates values for SiV; all other group IV defects will share the same structure under zero magnetic field. Energy levels are not to scale. The labelled A-D transitions are radiative transitions, as are seen in the fine spectral structure observable at low temperatures. Energy levels are separated due to spin orbit and the Jahn-Teller interaction (right panel). Photoluminescence and fine splitting of the SiV^- centre while at 11 K. In this case, the diamond sample is of a single crystal quality (SCD-β) and shows the line of the A transition convoluted with the B transition.

been of interest. Although the growth of high quality, low strain diamonds has been important to achieve high quality emitters, 'strain engineering' has also been developed to tune the defect properties (*i.e.,* increase its coherence time [148]).

4.1.2.1 Local Vibrational Mode (LVM)

A sharp peak has been observed in every colour centre's phonon sideband (PSB). ($NV^{-/0}$[23], SiV^-[149], GeV [141], SnV [142]) This line is the most intense portion of the sideband and is known as the local vibrational mode (LVM). It is attributed to the electron-phonon interaction of the oscillating heavy impurity atom [149].

The energy of the LVM relates to the curvature of the potential well in which the impurity atom is located, as shown in Figure 4.3. In SiV^- it has been observed to be 64 meV from the ZPL, placing it to be at 1.618 eV (766 nm). Interestingly and unsurprisingly these energies are known to shift with temperature, isotropic shifts, and pressure [150].

4.1.2.2 Neutral Vacancies — Charge Control

The neutral states of the known group IV defects (*i.e.,* SiV^0) are less affected by local phonons while maintaining an invariant structure; hence they could enable higher quality and more useful quantum systems [151].

To create this centre, charge control must be completed, which is typically conducted by co-doping the substrate with appropriate levels of charge donors/acceptors (commonly utilizing nitrogen or boron). At this time, among all group IV defects, only SiV^0 has been fabricated [152].

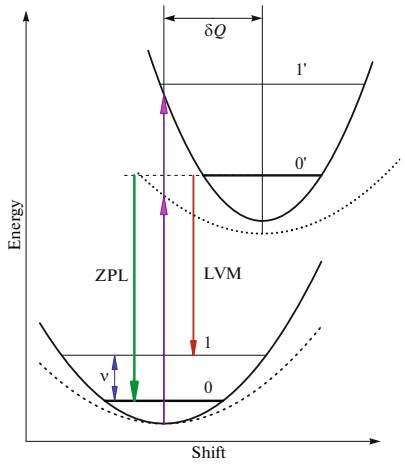

Figure 4.3: Schematic diagram of the potential surfaces for a Local Vibrational Mode (LVM). ν corresponds to the local vibrational mode. Solid curves correspond to the energies low pressures, while dotted lines represent high pressures. Reproduced from Ekimov *et al.* [150] with permission.

To our knowledge, the concentrations of co-dopants required to gain significant SiV^0 populations have not yet been published. The recent quantum photonics studies which have investigated the neutral silicon vacancy centre have relied upon commercially purchased diamonds [151, 153, 154].

For all samples presented in this thesis, PL from this defect was searched for, but unfortunately not detected. Most likely the concentration of SiV^0 was far too low, a situation which is not surprising as no post-processing or precise charge control was completed to enhance the probability of forming the defect.

4.1.3 SiV^- Growth

The SiV^- centre is known to form easily during CVD synthesis. It is so easily incorporated that the existence of SiV^- photoluminescence is used a key marker to identify CVD synthesized diamond. It rarely appears in natural diamonds [155].

During CVD synthesis, unintentional incorporation of silicon into diamond often occurs due to either the plasma etching of quartz present within the chamber or the residual silicon in the chamber from previous growth sessions. Both sources are common, as quartz (SiO_2) is the preferred window material for these CVD systems and silicon wafers are typically utilized as high-quality substrates to grow PCD diamond films. Furthermore, silicon vacancies form with a yield of approximately 15% (per foreign atom introduced) [134]. This formation rate is much greater than the level at which nitrogen is transformed into NV^- (about 1%) [140]. Combined with the high level of quantum efficiency (70%) observing the ZPL emission of SiV^- is relatively straightforward, even from minimal levels of silicon contamination in the CVD system.

Intentional silicon doping is often achieved by introducing silane gas to the deposition or by placing solid silicon into the chamber. Post-growth silicon doping by ion implantation can also be accomplished with the advantage of controlled spatial precision. This method, however, gives low yields and causes damage to the diamond. [140, 151]. This work utilizes silicon doping within the CVD process.

4.1.3.1 CVD Growth

As indicated previously, although silicon atoms can be added during a CVD growth through gas phase or solid, vacancies are also required to form the split vacancy centre (SiV^-). Vacancies present in the diamond lattice are known to be mobile above 800°C [156]. CVD growth is typically completed with the diamond above 850°C. These growth conditions can lead to an inherent mobilization of the vacancies during silicon implementation, allowing vacancy capture and consequently SiV^- creation at higher rates [134].

Si Source: Solid State The process of introducing silicon into the diamond by using silicon samples is simple, as evidenced by the difficulty that most producers have with reducing unintentionally introduced silicon. If a sample of solid silicon is placed into the chamber alongside the desired growth substrate, the hydrogen ions will efficiently etch atoms from the solid and add them into the plasma ball. In particular, if the growth rate is low, a large number of silicon atoms can be found in the diamond (hundreds of ppm) [157].

While the placement of silicon pieces into the CVD chamber is simple and efficient, it comes with two major problems. The first is the lack of control in silicon release, as it is difficult to "tune" and control the amount of silicon which will be etched and incorporated. Second, the silicon pieces will eventually be covered by a co-deposited diamond film, and consequently, will not be etched further, leading to a gradual reduction of silicon release into the plasma ball.

Si Source: Gas Phase Due to the inherent issues with silicon doping from a solid sample, the usage of silicon containing gases has gained popularity. In that regard, silane, SiH_4, has been a common choice. Unfortunately, it has been observed that the SiV^- concentration varies non-monotonically with gas addition [158]. Nonetheless, the use of silane has become the preferred method to obtain SiV^-, as it can result in high quality diamond with low residual strain [139, 140].

4.2 Photoluminescence of Colour Centres under Extreme Conditions

4.2.1 SiV^- Temperature Dependence

The SiV^- photoluminescence emission will shift with respect to temperature. The zero phonon line (ZPL) decreases in linewidth and blueshifts with decreasing temperatures. A similar spectral shift behaviour has been found in all other studied group IV colour centres as well as in the NV^- centre. With the NV^- centre, this has been ascribed to lattice contractions, which change the band gap E_g of diamond [159]. Upon first glance, this could also explain the changes recorded for the SiV^- centre. However, this explanation does not appear to hold up [135]. Instead, the shift appears to be dominated by second-order linear interactions with E-symmetric phonons [138, 140].

This interaction with phonons has been well described by Jahnke *et al.* [138]. For low strained diamonds, from low to room temperatures, the two-phonon electron scattering is expected to scale proportionally with T^3. Therefore, a T^3 function in the range of our study should best describe the relationship of linewidth to temperature and line shift to temperature [135, 140].

It is important to check this relation as it can change dependent on external factors. Note that

in the case of high strain diamonds a T^5 relation may dominate [138], and at high temperatures, the E-symmetric phonons which cause the T^3 relation instead result in a T^2 relationship. [160]. Finally, at low temperatures with high quality diamond, a linear dependence can dominate [135].

The defect spectral behaviour has been described for temperatures ranging from that of liquid helium (4 K) to room temperature (300 K) [135, 138] and up to 800 K [161].

Discussion of the high compared to low strain diamonds are included in [138], however in the present study (section 4.4.1) we will not attempt to estimate the actual strain value - per section A.3.2.

4.2.2 Pressure Dependence

To investigate the properties of the SiV^- centre under extreme pressure conditions, it is important to review previous work. Work upon the SiV^- centre is limited, therefore investigations of NV^- will also be described.

4.2.2.1 NV^- Pressure Relation

The high-pressure dependence of both the ZPL, and zero magnetic field splitting of the NV^- defect has been reported upon. The corresponding pressure shift of the ZPL has experimentally been found to be linear and shift at a rate of 5.5–5.8 meV/GPa [162, 163].

In addition to the experimental work, two theoretical studies have also given coefficients relating ZPL line shift to pressure. The first by Deng *et al.* [164] gives 5.75 meV/GPa calculated up to 500 GPa. A second study (Ekimov *et al.* [150]) gives a value of 6.5 meV/GPa. These ascribe the shift to lattice contraction upon the increase of pressure, which also changes the diamond band gap energy E_g.

Non-linearity Several of the theoretical studies [164, 165] have shown a non-linearity of the ZPL energy's pressure-related shift when examined over a large interval (≈100 GPa). In comparison, most experiments have reported linearity at more moderate pressures (up to 50 GPa) [24, 162, 163, 166]. However, one group has reported an experimentally observable quadratic dependence of the NV^- ZPL studying over the interval of 0–52 GPa) [147].

Phonon Side Band (PSB) It has been theorized that the photoluminescence from the PSB in the NV^- centre will be significantly suppressed and redistributed toward the ZPL emission under high pressures at low temperatures [164]. This has not been explored experimentally, but this increase in quantum efficiency could be of interest to several systems, particularly if single photon emitters are sought after.

4.2.2.2 Group IV Vacancies Pressure Relationship

Intrinsically, it is known that there will be a shift of the PL spectrum of any group IV defect with the application of pressure, as the lattice will contract and the electron density will restructure. These shifts can be caused by hydrostatic (isotropic) or uniaxial stresses. This study focuses primarily on the effect of hydrostatic (or quasi-hydrostatic) pressure conditions on the SiV^- defect (also see section 4.3.1.1).

Effects of Hydrostatic Pressure A single experimental high-pressure study has been published with respect to the SiV^- defect. The studied diamond was grown in nanocrystalline diamond through HPHT synthesis [147]. The experiment used a pressure transmitting medium (PTM) (explained in section 4.3.1.1) of helium up to 60 GPa. Pressure ramps at RT and 80 K were completed, which gave a quadratic pressure dependence. These results are presented in the form of:

$$E(P) = E_o \ + \ \alpha P \ + \ \beta P^2 \tag{4.1}$$

The α value was found to be 1.09 or 1.02 meV/GPa while the β was found to be -5.7 or -5.3$\times$ 10^{-3} meV/GPa^2 at 295 K or 80 K respectively. No error bounds were given by the authors.

Ab-initio calculations on the SiV^- defect to determine its high pressures properties gave a theoretical linear pressure dependence of 1.5 meV/GPa [150].

Similarly, comparisons with group IV defects under pressure (tin and germanium vacancies) show a linear pressure dependence for the ZPL spectral shift, with no pressure broadening of the emission. These experiments were performed, however, only up to moderate pressures of 9.4 and 6.9 GPa for SnV and GeV respectively [167, 168].

Additionally, the Local Vibrational Mode (LVM), known to occur for the SiV^- at 766 nm [169] is predicted to shift with pressure, but this has not been measured experimentally. An ab initio calculation by Ekimov *et al.* [150] has given the emission energy of the LVM correctly and predicted its energy at an elevated pressure, namely 10 GPa, with the value of 65.87 meV from the ZPL. An experimental verification of this pressure dependence could provide a piece of unique information on the curvature of the potential well and would likely lead to further understanding of this defect class. This study also makes predictions for the pressure dependence of the PSB which, to the best of our knowledge, have not been experimentally validated.

Effect of Uniaxial Pressure While it is not a focus of this study, it is worth mentioning that uniaxial stress is often used to elucidate the electronic structure of diamond. It is known that the application of stress strains a lattice along a known plane, lifting degeneracies and possibly revealing symmetries. For this reason, the SiV^- has been studied with uniaxial stresses [136, 170], where it has been seen to shift and split - revealing the fine spectral structure of the defect. Remarkably, the sensitivity to stress of SiV^- is roughly two-times stronger than that of NV^-, this leads to large shifts in the fine structure components [136].

Strain engineering of the SiV^- defect has also been completed, using a nano-electromechanical system to introduce uniaxial stress and tune the fine structure of the defect. The induced strain suppresses the interactions of the spins with the thermal bath. Due to this suppression, experiments performed at 4 K, were able to achieve spin-spin relaxation times (T_2) similar to that of 100 mK conditions without stress, for further discussion see Sohn *et al.* [172] and Meesala *et al.* [148].

Internal Strain It is important to take into account the amount of strain inherent to synthetic diamond, as it can vary depending on the method/quality of fabrication and the diamond post-processing. The method of examining the internal strain is best completed through the investigation of the PL low-temperature fine structure. Specifically, the ground state and excited state splitting are highly sensitive to strain, meaning that stressed defects will show splitting values which deviate from the known values of $\Delta\nu_{ground} = 48$ GHz = A-B = C-D and $\Delta\nu_{excited} = 259$ GHz = A-C = B-D as illustrated in Figure 4.2 [136]. These splittings were not resolved in the current PCD samples used for the pressure experiments of this work.

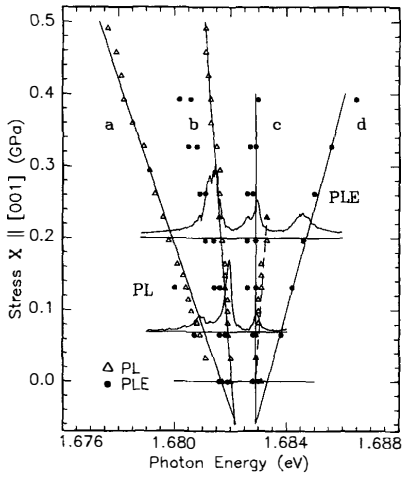

Figure 4.4: SiV^- fine structure spectra revealed by the application of increasing uniaxial pressure (from bottom to top). Reproduced from Sternschulte *et al.* [171] with permission.

4.3 Experimental Details

High-pressure conditions that are combined with temperature, magnetic fields, or uniaxial stress are often referred to as extreme conditions. In the present work, low temperature is needed to elucidate the SiV's electronic fine structure. The application of high pressures leads to manipulation of the vibrational and electronic energy states. Consequently, by utilizing both low temperature and high pressure simultaneously, the interesting dynamics of the colour centre's spin-orbital coupling are probed [148].

4.3.1 High Pressure Generation Equipment

Diamond Anvil Cell (DAC) As described previously (1.1.1), high pressures are generated through use of the DAC, pressurizing small volumes (nanolitres) of a sample to hundreds of GPa. In a DAC, microscopic samples are compressed between two opposing diamond anvils as shown in Figure 4.5.

A moderate force applied to the outer surfaces of the diamond anvils (known as the table, ∼2–4 mm diameter) transmit down into a much smaller area on the anvil culet (∼100–300 μm diameter). This dramatic reduction in area (∼10,000x) directly causes an amplification of pressure by this same ratio (recall: $P = F/A$).

With this device, a well-controlled force is needed. This was often accomplished mechanically, using screws which actuate a piston on which one of the two anvils is fixed. Alternatively, a remotely controlled gas membrane can be used to move the piston, providing fine control of the pressure on the sample under study.

For the present experiments, low temperature DACs (made out of beryllium copper—Easylab, Inc.) was used for all samples studied. The diamond anvils were of Ia type and had flat culet diameter of 300 μm. A pneumatically driven gas membrane was filled with helium to apply a precise force on the diamond anvil support (piston of the DAC), therefore precisely controlling pressure on the sample.

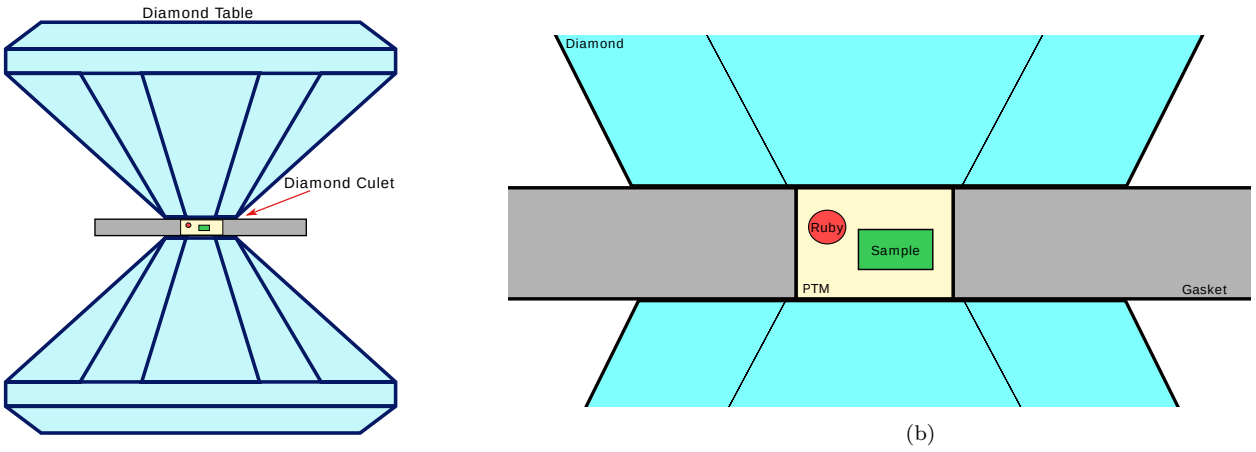

Figure 4.5: Schematic diamond of the Diamond Anvil Cell (DAC), showing the sample trapped between two opposing diamond anvils. Pressure is generated by the action of an axial force. A metallic gasket deforms axially and radially upon the displacement of the opposed anvils. This results in the reduction of the volume and a compression of the sample. a) Shows the entire cell, while b) focuses upon the sample chamber. Drawings are not to scale.

4.3.1.1 Hydrostatic Conditions

Stress and pressure are related concepts; while stress is directional, pressure is isotropic. The application of stress will broaden most transitions, can lift energy degeneracies, and create 'anomalous' signals [173]. For these reasons, an isotropic or hydrostatic pressure applied to a sample is the goal of experiments completed under high pressures.

Achieving hydrostatic conditions can be difficult in the DAC as the force is only applied to the cell uniaxially. Under moderate (<10 GPa) pressures at room temperatures, this can be mitigated entirely via the use of a fluid (liquid or high density gas). These fluids will become uniformly denser and will therefore isotropically spread the pressure throughout the chamber (hydrostatic conditions). At higher pressures every known medium will solidify, leading to possible strain (non-hydrostatic conditions). Through careful choice of the medium known as the Pressure Transmitting Medium (PTM), the effect of these non-hydrostatic conditions can be minimized.

Pressure Transmitting Medium (PTM) As discussed above, the selection of a PTM is highly significant. It has been determined through experimentation that materials will maintain hydrostatic conditions until certain pressures are reached. We worked with two PTMs in this study, these are a soft solid NaCl and nitrogen gas (at room temperature and pressure).

NaCl was used as a PTM at low pressures. This choice was motivated by experimental concerns such as ease of handling, good optical transparency, and lack of significant spectral features. However, it does not allow for hydrostatic conditions, and gives rise to minor non-hydrostatic conditions at relatively low pressures. Specifically, NaCl is known to maintain a consistent 'quasi-hydrostatic' state until around 15 GPa at room temperatures [174]. Unfortunately, under low temperature this pressure limit is dramatically lowered [175].

Nitrogen fluid was utilized as the second PTM. Note that nitrogen fluid is a high quality PTM, but is bested in its isotropic nature by only helium, and neon which can be seen in Figure 4.7 [173]. At room temperature, nitrogen fluid will maintain high quality hydrostatic conditions until ∼15 GPa, and past this point it will be more hydrostatic than non-gaseous PTM [173]. The choice of a high quality PTM is particularly important for low-temperature experiments as the non-

hydrostatic effects are accentuated under cryogenic temperatures. These non-hydrostatic effects are largely due to the solidification of the medium. For nitrogen, this occurs at 63 K at a pressure below 1 MPa [176].

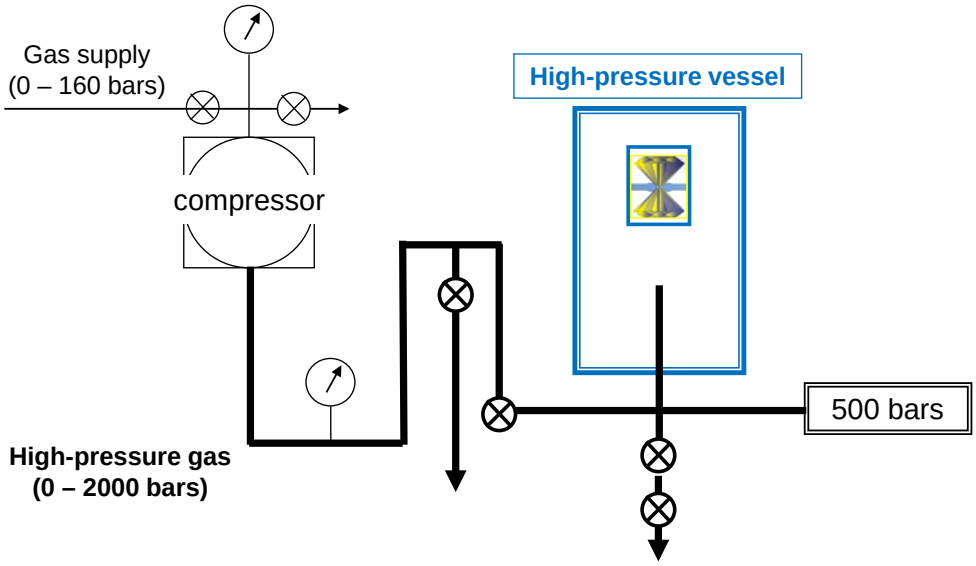

Figure 4.6: Schematic diagram of the gas system to load a gaseous species used as pressure transmitting medium in the diamond anvil. An inert gas (nitrogen, in the present work) is compressed in a high-pressure vessel to approximately ten times the pressure that is supplied from a standard supply cylinder. A diamond anvil cell prepared with a sample is placed for loading inside the high pressure vessel. A mechanism actuated from outside the vessel allows for the trapping of the high-density gas, sealing the metallic gasket on the diamond anvils. After loading, the diamond anvil is retrieved with the sample in a pressure transmitting medium at an initial pressure of approximately 0.5-1 GPa.

Loading of gas for use as a PTM is technically difficult, requiring cryogenic loading or the use of specialized equipment—namely a loading system, as is shown in Figure 4.6. In this work, a custom gas loading system designed and installed at LPSD at the University of Ottawa was used. To load the high density gas, a partially open DAC is placed inside a high-pressure vessel, filled with the gas of choice at elevated pressures (typically 0.15-0.2 GPa) using a compressor. Once the required gas pressure is achieved in the vessel at room temperature, an external motor activates a clamping mechanism which closes the DAC by moving the anvils against the gasket, hence trapping the high density gas. Further details of a similar system and its operation can be found in the literature [177]. The experiments in this study started with gas pressures of 500 bar (0.05 GPa) upon loading.

Metallic Gasket To contain the sample radially, a thin metallic 'gasket' is used to seal the small compression chamber containing the sample and the PTM between the diamond anvils (see Figure 4.5). It has one main success criterion, which is to compress and deform isotropically under load, as a non-uniform chamber in the axial or radial direction can lead to a gasket rupture and sample loss. This process is essential to maintain hydrostatic conditions.

In our study, the gasket was work-hardened by pre-compressing it with the diamond anvils from an initial thickness of $\sim$250 μm down to $\sim$100 μm. Following this, a custom laser micro-machining setup was used to cut out the tiny sample compression chamber. The sample chamber

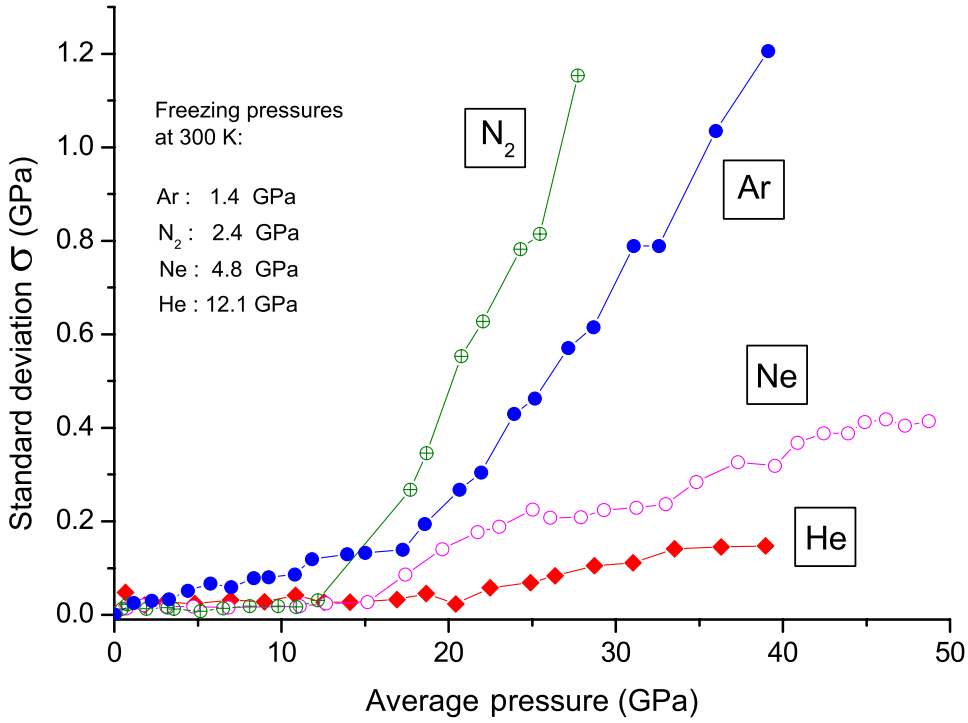

Figure 4.7: Comparison of various gaseous PTMs at room temperature. The standard deviation of pressures is estimated several pressures. Lower standard deviation pressures indicated a more hydrostatic PTM. Pressures and standard deviations are measured with a ruby gauge. Reproduced from Klotz *et al.* [173] with permission.

was then cleaned, the gasket realigned on one of the anvil culets and the sample was placed in the compression chamber along with an optical pressure gauge. Typical gasket materials for use in the experiments were either full-hard T301 stainless steel or rhenium.

Ruby Pressure Gauge Pressure detection within the DAC has largely standardized around the use of ruby (Al_2O_3:Cr^{3+}) photoluminescence as an optical gauge for pressures under 100 GPa. This is due to an easily accessible high-intensity photoluminescence signal, characterized by a strong doublet peak (the R-lines). The well-accepted standard curve for ruby pressure tracking is utilized in this study [178]. It must also be altered to account for temperature variation [179].

The measurement in this study was completed with two photoluminescence measurement systems, a real-time low accuracy system, which uses a 405 nm laser with a modified Mightex spectrometer. This allowed for a rough measurement of pressure. Due to significant spectral broadening and less reliable calibrations, it was not used as the final pressure measurement.

Instead, at each stabilized pressure point, the ruby luminescence, excited by a frequency-doubled Nd:YVO_4 laser (532.005 nm) was passed through a 0.5 m Andor spectrograph and recorded onto an Andor Newton cooled CCD. This process gives pressure uncertainties of 0.01 GPa with the peak fitting procedure detailed in section 4.3.5.

At high temperatures, the entire Lorentzian doublet describing the ruby lines was fit, but at low temperatures (<100 K) one line in the doublet (R_2) reduces severely in intensity. This along with a narrowing of both peaks means that fitting a single Lorentzian profile was preferred for all low temperature ruby spectra and pressure measurements.

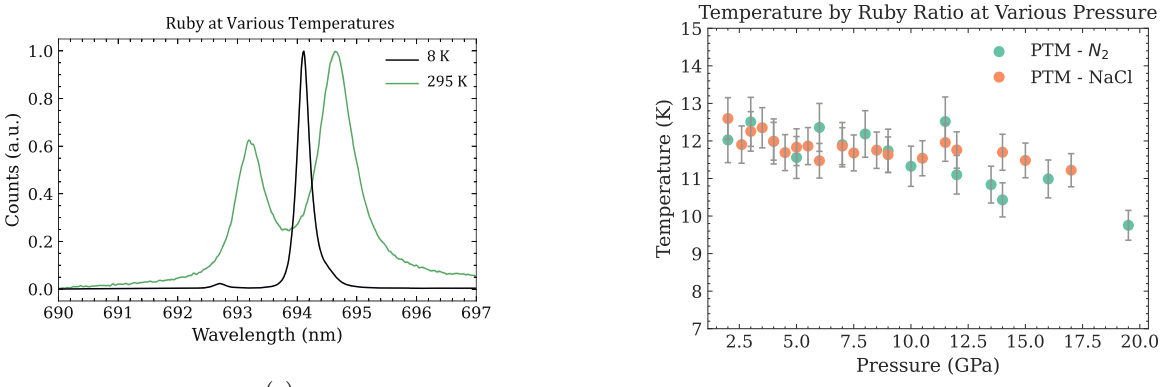

(a) (b)

Figure 4.8: The ruby photoluminescence as a low temperature sensor. a) Comparison between the ruby photoluminescence at room temperature (RT - 295 K) and the ruby at 8 K (as measured by the silicon diode). b) Temperatures measured by the R-line intensity ratio (per equation 4.3.1.1) at various pressures.

Ruby Temperature Gauge An *in-situ* gauge is preferred to a probe outside the DAC for precise temperature measurement. Therefore, a measurement from a probe in contact with the sample was used when possible. The ruby photoluminescence signal was also used for this, as the intensity ratio of the ruby doublet lines can be used as an optical thermometer. The temperature dependent population of the two levels can be seen in Figure 4.8a, leading to a dramatic reduction in the intensity of R_2 (lower λ line). At these low temperatures, the populations of the two levels can be described by Boltzmann statistics [180]:

$$I_2/I_1 = \eta e^{\Delta/k_B T} \tag{4.2}$$

$$\implies T[K] = \frac{\Delta}{k_B \times \ln(\frac{I_2/I_1}{\eta})} \tag{4.3}$$

Where k_B is the Boltzmann constant, Δ is the energy difference of R_1 and R_2, I_2/I_1 is the intensity ratio of R_1 and R_2, and η is this intensity ratio when the two levels are equally populated ($k_B T > \Delta$).

This relationship becomes inaccurate above ~100 K, but was a more accurate probe to evaluate the sample temperature than the silicon diode temperature sensor placed further away (to be described in section 4.3.2). Figure 4.8b shows the temperature derived from equation 4.3.1.1 with their uncertainties. Pressures measurements are corrected based upon those temperatures. This correction is small, however, as ruby line shifts due to temperature are minimal within this temperature region. (<0.002 nm or <0.01 GPa from 3 to 50 K).

4.3.2 Low Temperature Equipment

Cryostat A cryostat, designed to enable high-pressure measurements at low temperatures, was used for all low-temperature experiments. This is the Janis closed cycle He cryostat, model CCS-100/204, which uses a closed loop of compressed helium gas to allow for temperatures down to ~10 K. The sample holder was designed to fit a DAC inside the vacuum shroud and allow for optical measurements on a sample within a DAC thorough quartz windows. A re-entrant window was used to allow for a long working distance microscope objective (20x, NA 0.28) to focus and collect light from the sample.

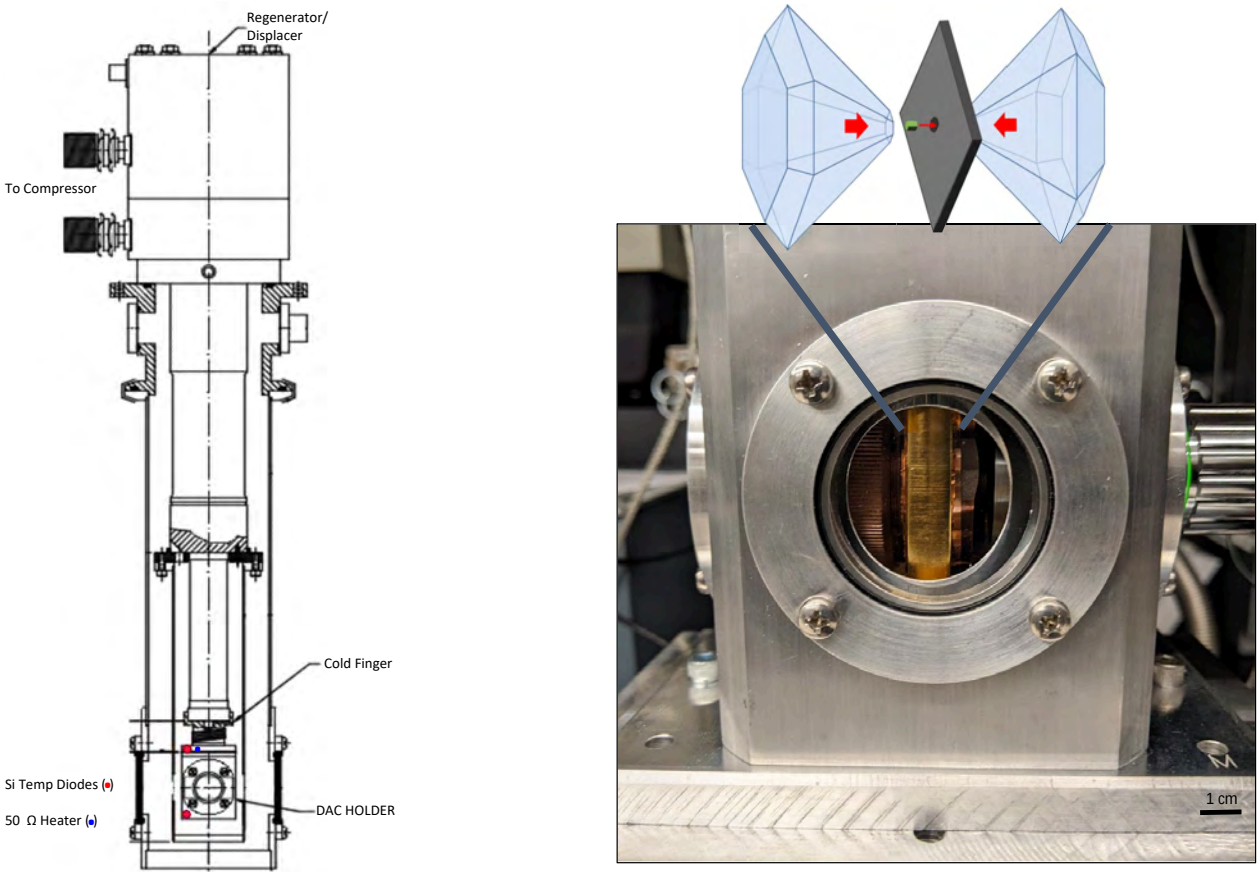

(a) (b)

Figure 4.9: Cryostat used for low temperature experiments a) Schematic diagram of the Janis CCS-100/204 cryostat designed for operation with a DAC. Adapted from Janis' instruction manual with permission. b) Photo observing the window of the cryostat, indication is given of the position of the DAC.

High Pressure Sample Holder For the low temperature studies in combination with high pressures, the low-temperature DAC (see section 4.3.1) was used to hold and compress the sample. The diamonds allowed for efficient cooling of the sample under pressure. However, if the diamonds were not in contact with the sample, the vacuum gap was found to inhibit sample cooling within a reasonable time period (no change within several hours). Therefore, low temperature experiments which occur in the DAC were monitored carefully or are initiated at an elevated pressure (>1 GPa).

Room Pressure Sample Holder To carry out measurements at low temperature near room pressure, diamond samples were placed onto a polished aluminum holder (puck) which was machined to be a similar size to the DAC. The thin diamond samples were then sandwiched between two polished copper plates, allowing for a high quality thermal contact with the diamond sample.

Temperature Sensor—Silicon Diodes Two silicon diodes were deployed for temperature monitoring and control, as seen in Figure 4.9. Since the heater was close to the bottom sensor and further from the cold head. As there was a temperature gradient across the cell, a more local measurement was deployed. For the aluminum puck, a platinum resistor (PT-100, with 100 Ω at 0°C) was attached nearby to the sample and used to determine the sample thermalization.

To control temperature, a 50 Ω heater installed on the DAC holder was employed, driven by

a Lakeshore Model 335 temperature controller. A PID loop based on the reading from the top silicon diode was used for *in-situ* control, but the local temperature sensor measurements were utilized for analysis and reporting.

Note on Cooling Sample PCD-$S2$ The procedure to study PCD-$S2$ under low temperatures followed the procedures of the high-pressure experiments as opposed to the low temperature experiments. Hence, the sample was analyzed in a DAC in a NaCl PTM, with the diamonds detached from the sample to avoid pressurization. Low temperatures were measured locally with ruby luminescence intensity ratio. As a result of this configuration, temperatures are likely to be more accurate. But, after several hours without heating, the sample did not manage to drop below 50 K. It is hypothesized that a vacuum gap was created in this temperature region due to unequal component contraction rates. Multiple captures were completed for location variation and laser power variance (see 4.3.4).

4.3.3 Samples

One major obstacle for studying diamond samples inside the DAC was the challenge of physically loading the sample into the cavity.

The cavity had dimension limitations—typically 100 μm in diameter and less than 100 μm in initial thickness, requiring the samples to be well under 50 μm thick (preferably under 20 μm). This limited sample thickness allows for the introduction of a pressure transmitting medium and for uniform compression.

As SCD is deposited on top of a seed crystal, it is difficult to obtain a thin, freestanding samples. This would require a detachment procedure, which would often be based on laser cutting with polishing to obtain the correct thickness. While these procedures have been implemented and discussed in the literature [181, 182], they are outside the scope and instrumentation of this work. For this reason, only PCD diamond samples, grown on substrates other than diamond, were selected for study here under pressure. Consequently, diamond PCD samples studied had significant intrinsic strains, which caused, for instance, Raman and luminescence line broadening. For that reason, fine spectral feature like splitting of the SiV^- peaks proved to be difficult to observe.

Four PCD thin films were studied under extreme conditions alongside a SCD diamond similar to SCD-α (section 3.4).

Properties of the PCD are summarized in Table 4.1 and a more extensive analysis is completed in Appendix A.

Sample	**PCD Dimensions**			**SiV^- Line**		
	Thickness (μm)	**Grain (μm)**	**Raman$_{FWHM}$ (cm^{-1})**	**Intensity$_{rel}$**	**FWHM (nm)**	**Wavelength (nm)**
PCD-β	570 ± 30	127.2 ± 28	3.28	12.6	4.9	738.27
PCD-α	22 ± 5	4.2 ± 1.2	3.44	154.7	4.4	738.51
PCD-$S1$	18 ± 5	7.9 ± 1.7	5.82	237.5	5.6	738.75
PCD-$S2$	15 ± 5	16.9 ± 3.2	4.68	10.3	5.2	739.06

Table 4.1: Various physical properties of the synthesized PCD films as obtained from characterization. The focus is upon the native diamond growth and the SiV^- defect PL line. Details of measurements provided in Appendix A.2.

Sample PCD-α is notable for its relative high quality of the diamond as assessed by Raman spectroscopy, combined with a relatively strong and narrow SiV^- photoluminescence signal. This led to this sample being the primary sample examined in the high-pressure studies (sections 4.4.2 and 4.4.3).

It is notable that while silicon is the primary element of the defect studied, no estimate of the silicon quantity will be provided. This is due to a non-monotonic photoluminescence and concentration signal relationship [183]. It is recommended that future work utilize Secondary Ion Mass Spectroscopy (SIMS) to quantify the concentration of silicon present in a given sample.

4.3.4 Data Acquisition

Procedures for data acquisition differed slightly depending on if the measurements were completed as a function of temperature or pressure.

One similarity shared by the two capture procedures, however, was the Raman/PL microscope used to acquire the data. The custom-built instrument presents a near-confocal optical mode used in the back scattering configuration. This Raman/PL microscope resides on a XYZ translation stage, allowing tracking of the sample during thermal contraction of the cold head inside the cryostat, and enabling 2D mapping capability. The Raman/PL microscope was also vibration isolated from the cryostat, although the compressor created additional uncompensated periodic motion of the sample mounted on the cold head.

Excitation Luminescence was excited through the use of a frequency doubled Nd:YVO_4 laser (Spectra Physics Centannia, 5 W total), giving a wavelength of 532.006 nm, with a maximum FWHM of 0.03 nm (quantified by a 0.5 m spectrometer - 2400 lines/mm grating). Measurements of the SiV^- were completed with the 1800 lines/mm grating.

Local heating on the sample has been observed due to the absorption of the exciting laser light; hence spectral acquisitions were completed at three differing laser powers, adjusted using optical density filters, to assess the level of heating. If local heating was seen to occur, a higher optical density filter was then utilized to reduce the laser light impinging onto the sample. Variance of the luminescence peak energy with the attenuated laser powers is reported as uncertainty in the measurements. This variation was performed for each measurement.

The Raman/PL microscope objective used to capture the scattered light is that of a 20× long working distance Mitutoyo objective (NA 0.28), giving a spot size of $\sim$5 μm at the sample. The light was then passed using a NA 0.22 multimode optical fibre through a 0.5 m Andor spectrograph, and recorded on either an Andor Newton cooled CCD or an Andor iDus cooled InGaAs detector array.

Low Temperature Procedure For this study, we chose to track the most intense luminescence line in the defect, which tends to be peak C (see Figure 4.2 for labelling) or the C-D portion of the doublet when there is significant convolution. Around room temperatures, a singlet with a convolved shoulder is commonly observed [184]. In this case, the main singlet peak was tracked.

At each temperature step, the sample was allowed to thermalize at the desired temperature. Determination of this thermalization was completed when the thermometers recorded a drift $<$0.01 K over the acquisition period.

High-Pressure Procedure When the Raman/PL microscope was moved across the sample at elevated pressures, variations in luminescence line shape were observed. For this reason, at

each pressure point, data from three locations were captured. These locations were determined to be the most spectrally distinct. The difference between the maximum and minimum values is reported as uncertainty. This effect is generally minimal in the more hydrostatic or lower pressure measurements.

For the capture of the SiV^- LVM, spectral signals above 750 nm were required. Unfortunately, the typically used CCD has a significant interference signal here, hence the small PSB was not distinguishable. Therefore, all data above 750 nm reported was captured with a 300 lines/mm grating on the spectrograph equipped with the Andor iDus cooled InGaAs detector array. This detector had significantly lower sensitivity (as compared to the CCD detector), therefore the full power input laser was utilized, in combination with an extended capture (60–300 seconds), to achieve good counting statistics. Additionally, due to the lower resolution of the low dispersion grating used, the finer structure was not observed in the SiV^- photoluminescence signal.

4.3.5 Data Analysis

Consistent data analysis techniques were utilized throughout the process to ensure reproducibility. Data were captured raw from the spectrometer and analyzed in purpose-written code. The different methods used are outlined here and data presented in this chapter.

Calibration A spectral calibration was completed by capturing and referencing a neon emission for each spectral range. Lorentzian line fits allowed for high accuracy spectral positions $\pm 0.01\ nm$ for 300 lines/mm diffraction grating and $\pm 0.001\ nm$ for 1800 lines/mm grating. A third-order polynomial was used to fit and convert pixel values to wavelength. Each dataset was collected with the focal plane of the Raman microscope situated to maximize the intensity of the SiV^- line.

No intensity calibration of the spectroscopic system was completed, therefore spectral efficiencies were uncompensated for. As a result, only similar datasets (with the same spectral centre and grating) were compared for intensity-related phenomena.

Peak Fitting Throughout these studies, several spectral lines were tracked and analyzed. Peak fitting was computed by using the Levenberg-Marquardt algorithm to complete a non-linear fit (χ^2 minimization) of the desired function. One standard deviation was used to represent the fitting uncertainty. Data were passed through a Savitzky-Golay filter to pre-smooth noise before fitting. When observing a solitary peak, a linear background was removed. Unless otherwise noted, Lorentzian profiles are fitted to photoluminescence and Raman spectral lines.

In several situations, such as in low temperatures with high quality diamond, four well-defined Lorentzian lines appeared as the SiV^- fluorescent signal. However, when the sample temperature increased to $\sim$80 K, these lines merged into a doublet and at room temperature, merged yet again into a singlet. In this situation, using different profiles for the fitting resulted in different central wavelengths and linewidths. This can lead to discontinuities in the results. Therefore, when a given spectral line can be questionably fit using two profiles, both profiles were tried; the uncertainty given reflects the difference in parameters in using the two profiles.

4.4 Results—Extreme Condition Studies

The results of three studies will be reported upon. The first is a temperature study, which compares samples cooled from room temperature (RT) to low temperature (10–50 K) with no applied pressure. The other two studies relate to high pressure experiments, one completed at RT (295 K) and the second done at low temperature (11 ± 1 K).

4.4.1 Low Temperature Study

To observe the SiV^- defect's fine spectral structure, low-temperature conditions are required. The features appear at different temperature conditions, affected by the level of strain within the diamond. In strain-free diamond, these four fine components (Figure 4.2) can be observed at temperatures below ∼70 K [185]. The SiV^- has previously been studied under low temperatures with high quality experimental investigations [135, 138]. This research work attempts to reproduce these established relationships and judge any deviations resulting from the samples' intrinsic strains. Linewidth and the spectral line shift are the two features of the ZPL which vary with temperature; both will be analyzed here.

Samples Three samples were studied - the first two were grown under the same conditions (240 mbar, 4.2 kW, 4% CH_4, 1000°C, with the SCD seed placed within a pocket). The PCD is named as PCD-β and SCD is denoted as SCD-β. The third sample a PCD thin film was known as PCD-$S2$.

While the SCD and PCD samples underwent similar conditions, they showed significantly different line splitting behaviour (Figure 4.10). The fine structure of the doublet was observed at three different temperatures for the three samples: 180 K for SCD, 80 K for PCD-β, and no splitting behaviour is seen for PCD-$S2$ (recall that a minimum temperature of 50 K was achieved). This behaviour is expected, as the diamond Raman linewidth (used to estimate the growth quality) correlates well to the temperature at which the line splitting is observed.

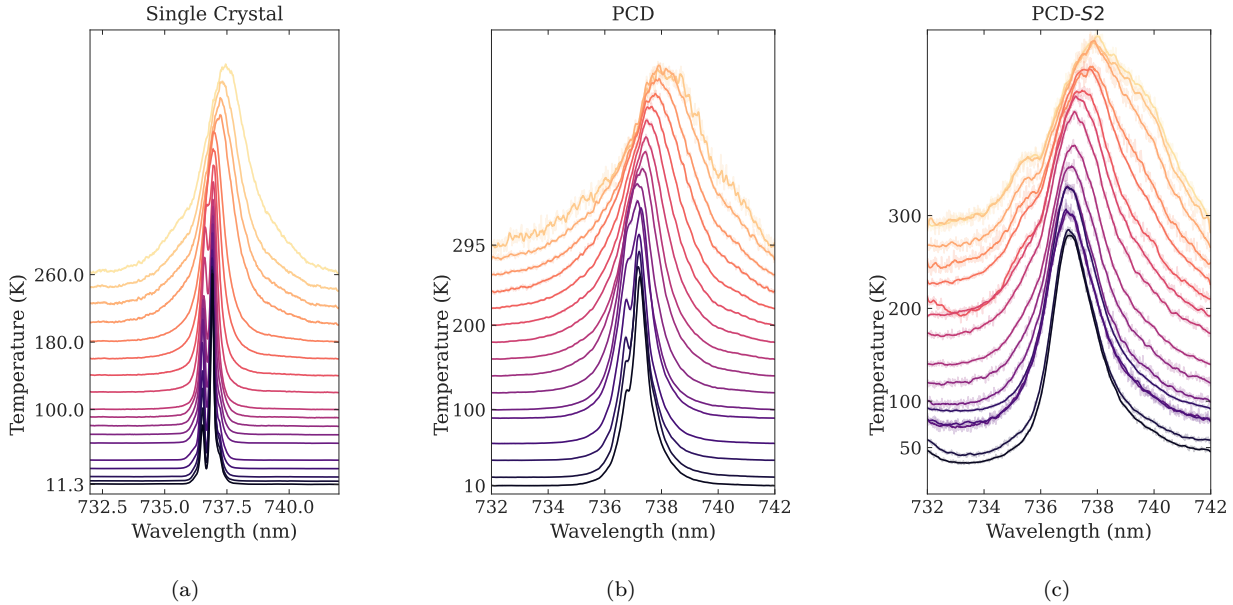

Figure 4.10: Visual comparison of SiV^- luminescence lines for several diamond samples, as they shift and split with decreasing temperature, from top to bottom. Note that the crystalline qualities directly affect the line splitting.

Data Fitting In accordance with the referenced studies [135, 138], the linewidth and line shift for each sample are fit with a cubic function. All three samples shown in Figure 4.11 appear to follow the general cubic function well for both their linewidth and line shift.

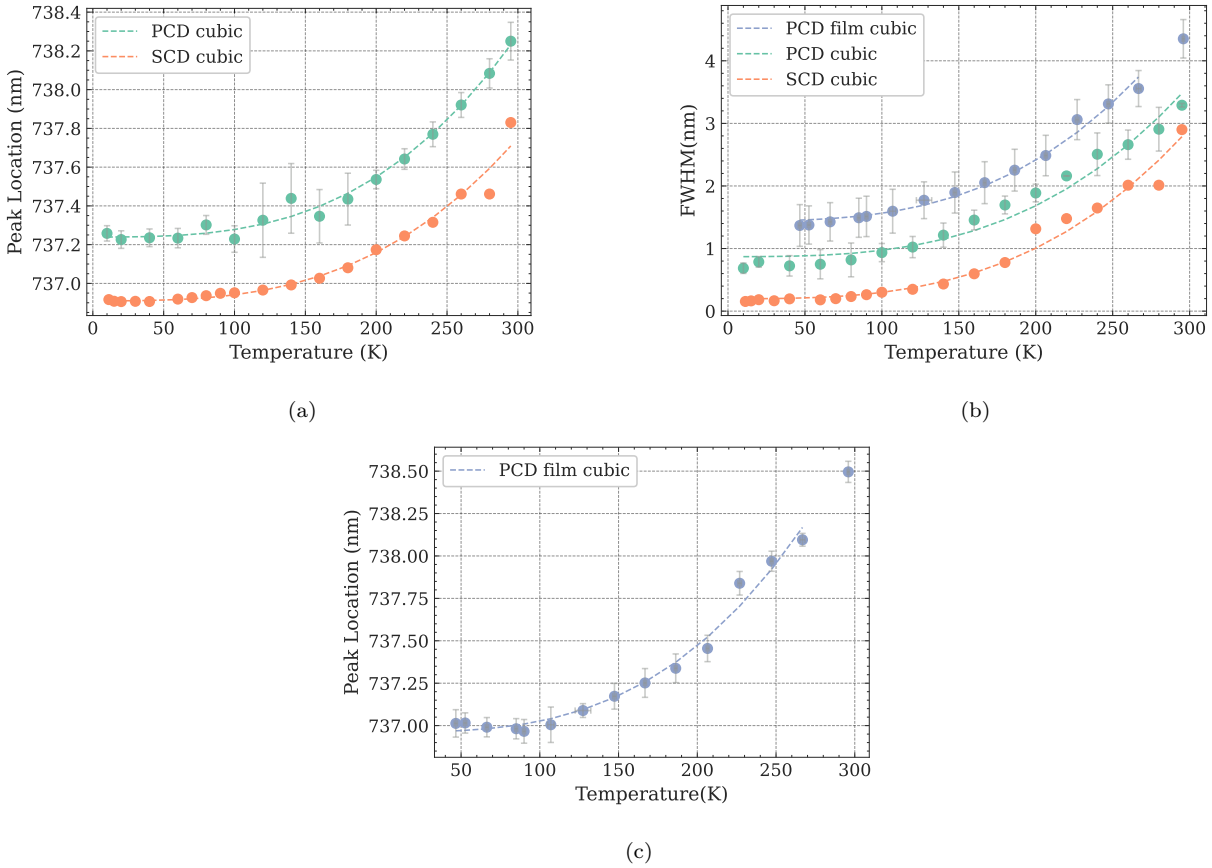

Figure 4.11: Comparison of the spectral shift and the linewidth of the photoluminescence of the SiV^- defect for three samples. The first two samples are the heteroepitaxial (PCD) and homoepitaxial diamond (SCD) grown under the same conditions. The third sample (PCD film) is the thin film PCD-$S2$, showing larger strain. a) Optical line shift as a function of temperature for the PCD and SCD samples. b) Linewidth obtained from a Lorentzian fit, comparing all three samples. c) Optical line shift of PCD-$S2$. Uncertainties for the SCD sample are below the marker size.

Line Shift While the function of $\Delta = (\lambda_0 + \alpha \times T^3)\, nm$ has been relatively well established [140, 144], the constants (λ_0, α) themselves have not been published to our knowledge.

By analyzing the graphs and data found in relevant publications, a rough determination of the fitting parameters used in the studies was completed (Table 4.2). However, note that significant differences in the data analysis techniques exist, such as the choice of line fitting profile (Gaussian/Lorentzian/Pseudo-Voigt). Despite this disparity, a reasonable level of agreement is found between the studies.

The present data can be compared against those of other published studies. The λ_o parameter is seen to vary substantially (by 1.5 nm) between the various reports. This could depend on the level of line splitting achieved.

Our data points indicate the higher quality diamond emitted at slightly higher λ_o, which corresponds to a spectral blueshift, similar to that induced by an increased pressure, as discussed in 4.4.3.

Source/Study	λ_o **(nm)**	α **(nm/K^3)** $\times 10^{-8}$	**Note**
Feng and Schwartz [159]	737.3	4.9	Thin films, 1-10μm grains
Neu *et al.* [135]	737.3	4.0	SCD diamond film
Jahnke *et al.* [138]	736.9	5.5	High quality SCD
Dragounová *et al.* [186]	738.3	4.9	PCD film
SCD (SCD-β)	737.23(1)	3.8(1)	High quality bulk SCD
PCD (PCD-β)	736.91(1)	3.1(1)	PCD grown with SCD-β
PCD film (PCD-$S2$)	736.69(3)	6.3(4)	Thin film (Table 4.1)

Table 4.2: A summary of results from different studies which investigated the SiV^- signal under low temperature conditions, compared against the parameters found in this work (bottom portion). Parameters were not provided in the respective publications and hence were determined from the published graphs.

However, it is worth nothing that our highest quality diamond (SCD-β) had the highest λ_o, while the highest quality diamond reported in the literature [138] has the lowest λ_o. This variation is relatively minor, and is possibly due to the difference in the fitting procedure used by the authors.

The α parameter (cubic term coefficient) found in our studies has a larger difference than the values presented in the literature. The high quality SCD diamond listed in Table 4.2 corresponds with the data presented by Neu *et al.* [135], while the two other samples fall outside the range of the previously presented data.

Samples PCD-β and PCD-$S2$ had high levels of strain, causing the convolution of the fine spectral structure.

Linewidth We can compare our results to the minimum linewidths of Jahnke *et al.* [138] and Neu *et al.* [135] which are 220 MHz at 10 K and 20 GHz at 5 K respectively. These convert to linewidths of 0.4 pm and 0.04 nm respectively.

Significantly larger linewidths were found in the present data. The smallest linewidths found are of 1.44(3) nm for PCD-$S2$, 0.87(6) nm for PCD-β, 0.20(4) nm for SCD-β. Our results are not surprising, as both the referenced studies are from research groups well known for the growth of high quality diamond samples.

Although the spectral narrowing measured is modest, the cubic-term coefficients are nonetheless 12.1(4), 10.2(5), and 10.1(4) $\times 10^{-8}$ nm for SCD-β, PCD-β and PCD-$S2$ respectively. This can be compared to a reported broadening coefficient of 3.46×10^{-8} nm [138]. The broadening coefficient has therefore been found to be significantly larger compared to those reported in the literature. The values are, however, consistent for all our samples.

From the graph presented in 4.11b, it can be seen that the three samples of varying qualities are clearly differentiated, with the lower-quality diamonds maintaining broader spectral lines. Note that the results from high quality diamonds reported would also appear significantly different, due to their small linewidths.

SCD-β judged to be of 'high' quality when studied based upon the diamond Raman line, but the SiV^- showed significant broadening here. This indicates that the SiV^- linewidth at low temperature was significantly more sensitive to lattice strain than the diamond Raman line. Therefore, the linewidth of the SiV^- PL emission could be a more useful indicator for judging

the quality of ultra-high-purity diamond grown in the laboratory. Conversely, it also complicates the usefulness of the SiV^- defect as a quantum platform for sensors, as any sensor would have significant sensitivity to internal diamond strain.

Discussion It was found that the SiV^- PL for the three samples studied in this work follows the previously reported temperature dependence relationship. There is, however, a large variance in the coefficients used to model the temperature dependence of the spectral features observed. This variance is likely explained by the degree of internal strain. Therefore an independent quantitative measure of internal strain would be useful to confirm the correlation. For example, in a future work, a quantitative evaluation of a sample birefringence could be a useful metric.

4.4.2 High-Pressure Study (Room Temperature)

The investigation of the pressure-induced effects upon SiV^- spectral signature has been relatively neglected; only Lyapin *et al.* [147] has reported upon the topic.

To this end, the first set of experiments were performed as a function of pressure at room temperature, and the samples were also held using the DAC to maintain consistency with the other experiments.

It is important to note that, as seen in the temperature results, the SiV^- defect is strongly affected by strain in the diamond. Therefore, the ability to study the effect of an externally applied hydrostatic pressure will be limited by and convolved with variations due to non-hydrostatic (deviatoric) stress conditions which will lead to strain.

Experiments Results of three separate experiments will be presented; the main graphs are shown in Figure 4.12. The first sample studied was PCD-$S1$ compressed in a NaCl PTM. The pressure points were taken below 15 GPa allowing the sample to remain under quasi-hydrostatic pressure conditions. Above this pressure, major non-hydrostatic effects came into play, and the gasket integrity was lost. The second experiment with PCD-α also used NaCl as a PTM. The gasket only survived up to 11 GPa. Finally, PCD-α was loaded with a N_2 PTM, and data points were taken for pressures below 15 GPa. This combination of samples and PTM allow for comparisons which distinguish the effect of sample choice from the effect of PTM choice. First, a comparison of the PTM's effect on the results will be presented proceeded by a comparison of samples. Following this, a general discussion of the SiV^- defect relationship with pressure will be completed. All comparisons will regard both the SiV^- PL line shift and linewidth.

4.4.2.1 Effect of PTM

The selection of PTM is important, as it is easy to misattribute the effects of increased strain as the effect of increased pressure.

In this section, we will compare two samples from the same growth (PCD-α) in two different PTM. These PTMs are NaCl and N_2 (discussed in section 4.3.1.1).

SiV^- Line Shift Visually, as illustrated in Figure 4.13a, it appears that the line shifts derived from pressure are similar, until a deviation at 9 GPa in the NaCl PTM. The line shifts' dependence on pressure was represented by: 1.680(1) meV + 0.93(1) meV/GPa for the N_2 PTM and 1.679(1) meV + 0.97(2) meV/GPa for the NaCl PTM.

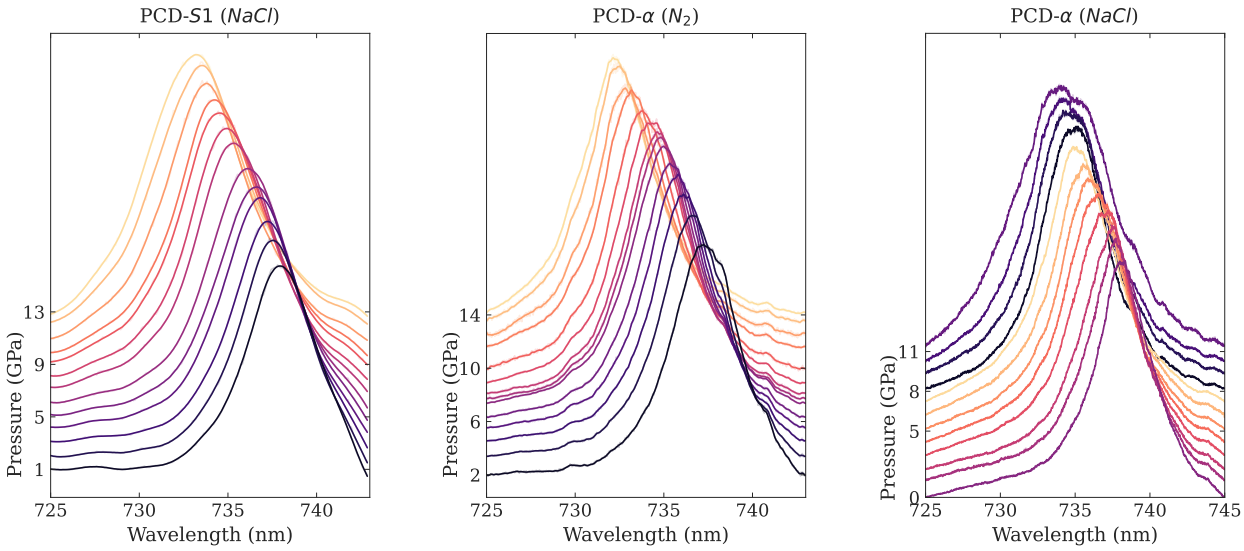

Figure 4.12: SiV^- luminescence recorded as a function of pressure at RT for three samples compressed in either NaCl or N_2 as the PTM.

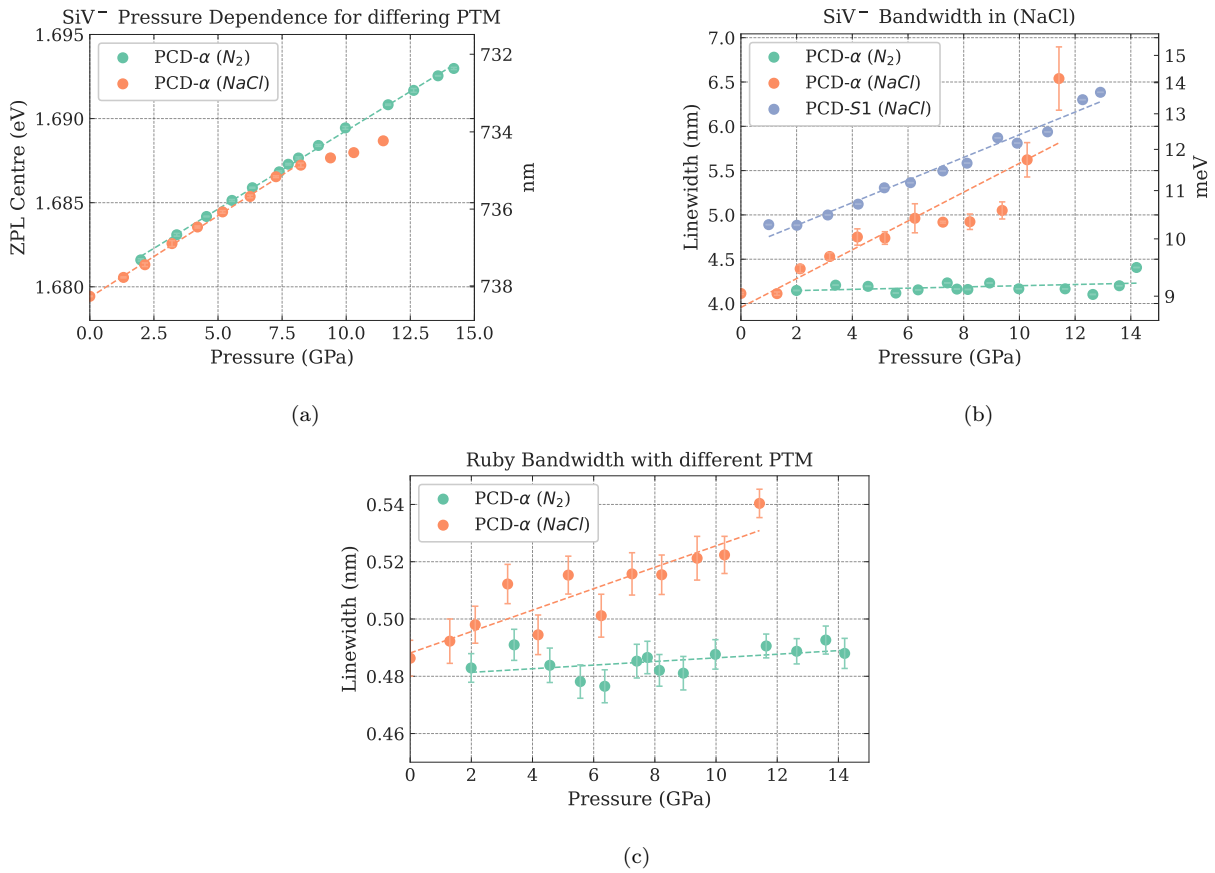

Figure 4.13: Pressure dependent ZPL PL emission for the SiV^- defect in two differing PTM - NaCl and N_2. a) Line shift of the SiV^- in differing PTM. b) Linewidth for all three samples. c) In-situ ruby linewidths of the two compressed samples in different PTM. Uncertainties below the size of the marker are not shown.

These fitting results correlate well with one another, indicating that in this range (0-9 GPa), the pressure line shift is independent of PTM.

For pressure beyond 9 GPa in a NaCl PTM, the linear relationship does not hold well. In Figure 4.12c it can be observed that line-splitting appears to occur in this region. A singlet was used to fit all data. The non-hydrostatic stress caused by the NaCl PTM is hypothesized to cause this effect.

SiV^- Linewidth The effect of pressure on the SiV^- PL spectral line width is shown in Figure 4.13b. Fitted linewidths are represented by 9.35(1) meV + 0.015(12) meV/GPa with an N_2 PTM and 9.0(4) meV + 0.37(6) meV/GPa for a NaCl PTM. The difference in these relationships as seen in Figure 4.13b is visually striking, showing a significant broadening from the use of NaCl as the PTM. The same outcome did not appear to exist when N_2 was used as the PTM.

Also included in Figure 4.13b is the other sample (PCD-$S1$) in a NaCl PTM. Its shift had a similar relation to the PCD-α in a NaCl PTM. This suggests that the PTM was the primary determinant of linewidth, which we hypothesize was due to its non-hydrostatic stresses.

Fundamentally, this indicates that there is no intrinsic relationship between purely hydrostatic pressure and line broadening, or that this effect is weak. This same effect has been shown in recent studies, where under moderate pressures (<10GPa), both tin and germanium (group IV) vacancy defects in diamond present no discernible PL line broadening and only a spectral line shift [167, 168].

This result also offers promise for this defect and similar group IV-vacancy defects, to be used, specifically as sensors in extreme conditions research.

Ruby R_1 Linewidth In extreme conditions research, the ruby R_1 linewidth is commonly used as a measure of inhomogeneity and non-hydrostatic conditions [187]. Therefore, the SiV^- line-broadening observed can be compared with the ruby R_1 line broadening. These R_1 linewidths measured alongside the PCD-α sample are: 0.48(1) nm + 0.0006(3) nm/GPa with the N_2 PTM and 0.49(1) nm + 0.0049(6) nm/GPa for the NaCl PTM.

The measured ruby R_1 linewidths reinforce the idea that the broadening observed in SiV^- is caused by inhomogeneity. Additionally, these results indicate that the SiV^- defect is more sensitive to inhomogeneity than the ruby linewidth, as a 0.04 nm ruby broadening correlates to a 1.5 nm effect in the SiV^- for the same pressure.

The SiV^- defect could be directly implemented into the small tip of the diamond anvil (culet) with relative ease. Therefore the defect could be used as a highly sensitive two-dimensional sensor to map for instance, non-hydrostatic conditions in the DAC. Previous studies along this line of study typically use arrays of ruby microspheres [187], giving results which can be erroneously affected by the uncontrolled variation of Cr^{3+} concentrations in a single ruby microsphere.

Conclusions regarding the use of various PTMs While it is clear that choice and use of a given PTM could affect the inhomogeneity in the sample chamber, it appears that the pressure dependence of the line shift should be independent of the PTM. However, it should be noted that line-splitting caused by anisotropy should be an effect to be cautiously aware of and considered.

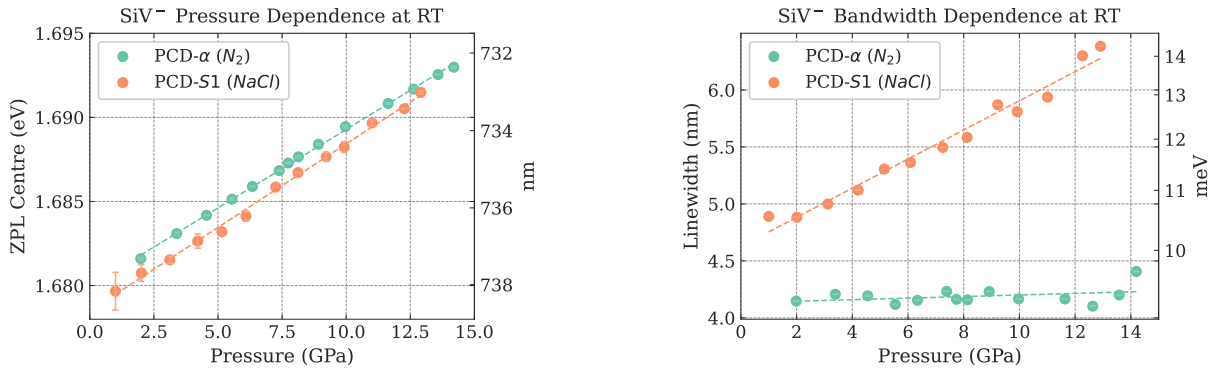

(a) (b)

Figure 4.14: Pressure Dependence of the ZPL PL emission for the SiV^- defect in two samples - PCD-α and PCD-$S1$. a) Line shift of the SiV^- PL emission at selected pressures. b) Linewidth of the two samples as a function of pressure. Uncertainties below the size of the marker are not shown.

4.4.2.2 Comparison of Differing Samples

As it appears that the PTM will not significantly affect the line shift of the SiV^- PL signal, a comparison of PCD-α and PCD-$S1$ will be completed with the highest quality data available regardless of PTM used. In effect, PCD-α in an N_2 PTM is compared with PCD-$S1$ in a NaCl PTM .

The samples studied (described in A.2) are significantly different, specifically in relation to expected silicon concentration and residual strain. For instance, PCD-$S1$ represents a lower quality sample and was grown with solid silicon pieces in the chamber during growth.

Linewidth As seen in Figure 4.14a, the major differences in the relationship between linewidth and pressure indicate that an external factor (PTM choice) influence the relationship, per section 4.4.2.1. Relevant results are presented in Table 4.3.

Line Shift Both samples present a linear spectral line shift with pressure, up to 15 GPa. The pressure shifts are 0.99(2) meV/GPa and 0.93(1) meV/GPa for PCD-$S1$ and PCD-α, respectively. These results fall slightly outside the reported value of 1.09 meV/GPa as reported by Lyapin *et al.* [147]; the shifts are nonetheless independent of PTM used or sample studied.

There is, however, no evidence of a higher order polynomial dependence on pressure; a second-order fit for instance does not significantly improve the quality of fit. A linear relationship between pressure and the line shift is thus more consistent and in line with the ab-initio calculations completed by Ekimov *et al.* [150] and with the results of other studies of group IV split-vacancy defects [167, 168].

While the linear shifting rate appears to be relatively consistent, the initial central wavelength of the PL emission appears to be significantly altered between samples. This could be attributed to different residual strains, or different concentrations of defects within a given sample. All of this is nonetheless consistent with results found in previous experimental studies as summarized in Table 4.2.

Discussion Through the comparison of the datasets from three different samples, it is fair to say that our results regarding the pressure shift of the SiV^- defect's PL emission are in agreement

with those reported by Lyapin *et al.* [147]. This work, however, does not observe a second order dependence of line shift on pressure. It is however noted that strains within the high-pressure sample container can create line-splitting events, some of which can be obscured by the broadened lines.

Additionally, this work suggests that the pressure shifting of the ZPL and hence the electron density redistribution is independent or only weakly dependent upon strain. This suggests a promising future of the SiV^- defect or other similar group IV-vacancy defects as suitable sensing systems in extreme conditions research.

4.4.3 High-Pressure/Low-Temperature Study

We now look at the influence of PL emission of the SiV^- defect with the combination of high pressure and low temperature. In this context, low temperature (LT) refers to the lowest temperatures achieved with use of the laboratory cryostat. In these studies this corresponds to 11(1) K (Figure 4.8b).

For the PL spectra recorded at LT only samples from PCD-α were used. The PL spectral emissions were captured from samples compressed using both the NaCl and N_2 as PTMs. The sample pressure increase was controlled remotely through a gas membrane system driving the DAC, using helium gas to inflate the membrane. Due to this limitation of the pneumatic system to increase the sample pressure, the lowest initial pressure was $\sim$2 GPa.

In Figure 4.15 the results of the two experiments are shown. The first notable observation is that no clear splitting of the PL line is seen without an applied pressure *i.e.*, resulting from the sole cooling of the sample. This is a major limitation of the study and results, which could only be remedied by fabricating higher quality samples. These would be either SCD thin enough to be compressed in a DAC or an optimized PCD growth.

Figure 4.15c shows the defect PL profile as the sample is cooled down. It is worth noticing that in the range of 30–100 K, the luminescence appears as a doublet, but the doublet profile wanes as the temperature decreases. This behaviour is also seen in Figure 4.10b.

For the two PL signals as a function of pressure (Figure 4.15b and 4.15b) some line-splitting is clearly observed. The recorded lines, however, are heavily convolved and become broader at higher pressures.

Sample Properties			**SiV**	
Sample	**PTM**	**Temperature**	**Lineshift ($\frac{meV}{GPa}$)**	**Linewidth (meV)**
PCD-$S1$	NaCl	295 K	0.99(2)	10.5(1) + 0.30(1) GPa^{-1}
PCD-α	NaCl	295 K	0.97(2)	9.0(4) + 0.37(6) GPa^{-1}
PCD-α	N_2	295 K	0.93(1)	9.35(1) + 0.015(12)GPa^{-1}
PCD-α	N_2	11 K	1.23(4)	-
PCD-α	NaCl	11 K	0.63(1)	-

Table 4.3: A summary of experimental conditions to measure the SiV^- PL under a high pressure and low temperature.

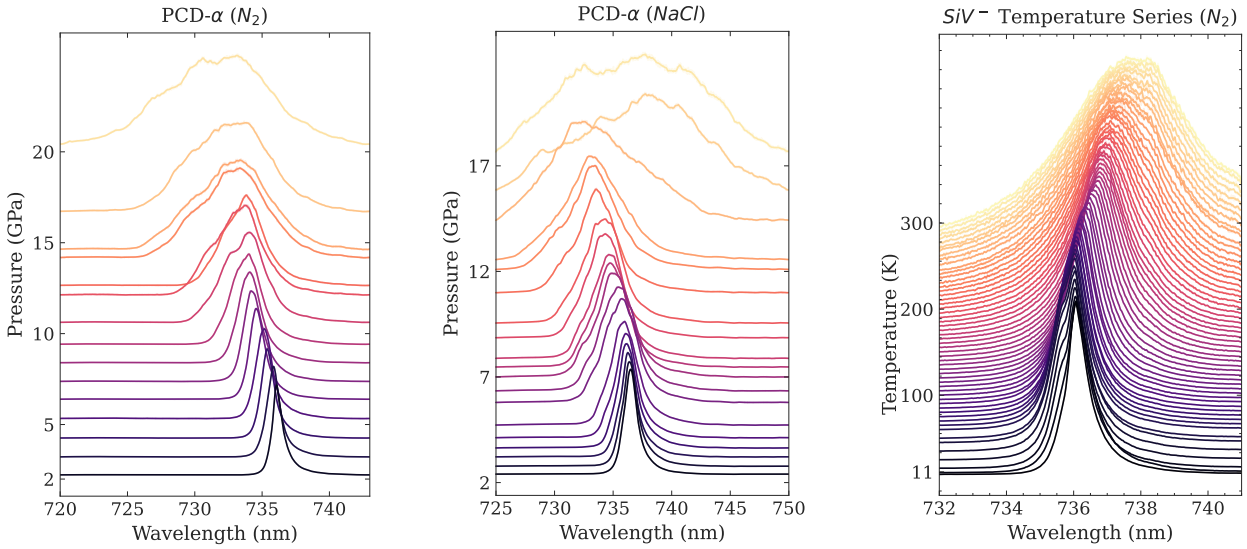

(a) (b) (c)

Figure 4.15: SiV^- luminescence from PCD-α under differing PTM as a function of pressure at temperature (11(1) K). Note that the wavelength scales are not the same in each graphs. c) A cascade plot of the PCD-α SiV^- luminescence as a function of temperature at room pressure, showing the line splitting and narrowing behaviour.

Since all low temperature, high-pressure experiments reported were most likely completed under non-hydrostatic conditions [187, 188], it will be difficult to disentangle sample initial strain from the induced strain by the application of an external pressure.

Line Shift of PCD-α in an N_2 PTM As it is clear that there are convolved lines in the PL of PCD-α compressed in N_2, these line groups are fit and the central wavelength of these convolved peaks are shown in Figure 4.16a. An example of this fitting procedure and results are shown in Figure 4.16b.

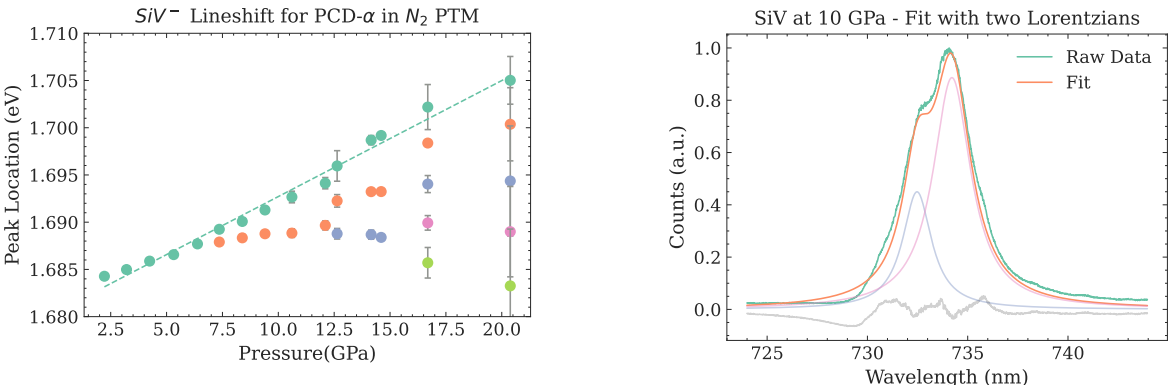

(a) (b)

Figure 4.16: Pressure Dependence of the ZPL PL for the SiV^- defect in PCD-α at 11(1) K a) Line shift of the SiV^- caused by pressure. The energy (wavelength) of each deconvolved line is plotted, colours represent the position of a 'tracked' line. b) An example of double-line fit, at 10 GPa with the resulting two peaks and residuals shown.

The line tracked in Figure 4.16a is not the most intense line; instead it is the line with the lowest wavelength. Its pressure dependence is modelled by the linear equation 1.680(1) eV +

1.23(4) meV/GPa. It is also interesting to follow the most intense line, which in this case gives 1.678(1) eV + 1.0(1) meV/GPa (shown in Figure 4.16a as the orange, or second-lowest wavelength point).

Line shift of PCD-α in a NaCl PTM A similar procedure follows for PCD-α compressed in NaCl. However, it is quickly noted that the fits are of significantly lower quality (see uncertainty ranges). Note, the lesser quality fits generally apply to the sidebands as opposed to the main peak of interest. This main peak of interest is the most intense peak in the signal. The behaviour appears to be linear and matches a fit of 1.6820(1) eV + 0.63(1) meV/GPa.

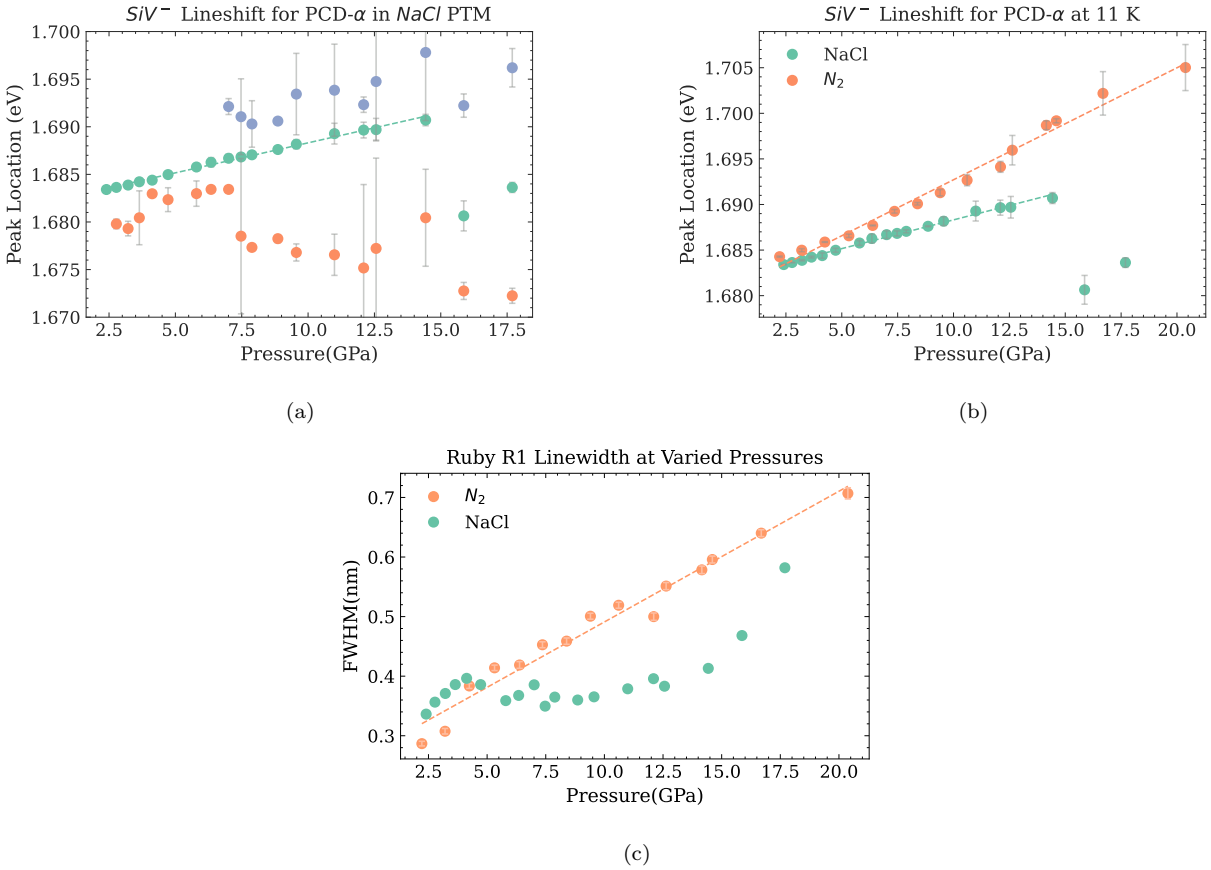

Figure 4.17: Spectral features of the SiV$^-$ defect PL as a function of pressure in different PTMs a) Lineshift at selected pressures. Each line obtained from the fit of the spectrum is displayed. b) Comparison of PL shifts for the sample compression in the two different PTM. c) Comparison of ruby R_1 linewidths as a function of pressure for the two PTM at 11(1) K.

The two linear relations observed as a function of pressure are plotted against each other in Figure 4.17b, illustrating the strong difference in the linear relationship with respect to the different PTMs used. It is hypothesized that the difference in slopes are primarily driven by deviatoric stresses induced in the NaCl PTM. These stresses would shift the lines in the opposing direction to the hydrostatic shift, therefore the two effects would compete and would result in a reduced overall linear shift. This explanation is consistent with the pressure coefficient of peak C shown in Figure 4.4 and the results reported in the studies of Meesala *et al.* [148] and Sternschulte *et al.* [170]. Verification of this hypothesis would require a tracking of inherently sharper peaks and a more accurate quantification of initial sample strain.

Also plotted in Figure 4.17c is the ruby R_1 linewidth comparing the two samples. The result is striking as it indicates that NaCl provides a better pressure transmission than N_2, as judged by the variation of the R_1 linewidth, over a significant pressure range at low temperature (11(1) K). The larger linewidth of the ruby R_1 line may be explained by the fact that the separated ruby microspheres used had a different Cr^{3+} concentration or residual strain to start with.

The linear relationship of the R_1 shift is nonetheless consistent with a high quality PTM in LT while the higher order relation seen with NaCl is consistent with lower quality PTM [188].

It is worth looking at the significant non-hydrostatic effects even where the N_2 PTM is used. Despite the fact that N_2 is known to be one of the highest quality PTMs, it is still known to develop non-hydrostatic effects at LT [187]. The broadening observed roughly matches the results presented in the literature [175].

SiV^- Line Shift Based upon Temperature It was also interesting to compare the spectral shifts recorded at low temperature to those collected for pressure measurements at RT. This is shown in Figure 4.18. As previously mentioned, the pressure change at LT was 1.23(4) meV/GPa, which can be compared to the shift at RT *i.e.* 0.93(1) meV/GPa.

It must be said, however, it is notable that beyond approximately 10 GPa, the PL spectrum becomes significantly more convolved. If we are to limit ourselves to this lower pressure regime (Figure 4.18b), a line shift of 1.681(2) eV + 1.02(3) meV/GPa is calculated.

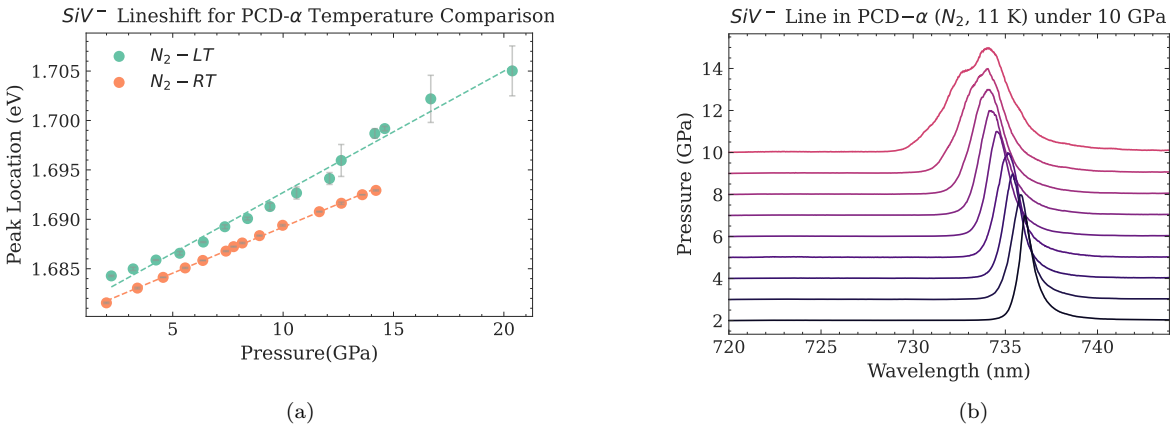

Figure 4.18: Lineshifts of the SiV^- PL at selected pressures a) Lineshift of the SiV^- PL caused at RT and LT (11(1) K). b) Cascade of PCD-α SiV^- PL spectra at selected pressures, below 10 GPa.

Discussion The pressure data at LT is significantly more difficult to interpret when compared to the data captured for the RT pressure data or temperature variation. This is caused by the unavoidable non-hydrostatic pressure effects in this realm. Despite this fact, the linear relationship for the pressure-induced line-shifting observed at RT was also found to hold at LT. This linear shift rate is of 1.1(2) meV/GPa.

However, when considering the sample compressed in NaCl at LT, a significantly different pressure coefficient was found. The finding could be attributed to strain induced line splitting, as has been mentioned by Meesala *et al.* [148] and Sternschulte *et al.* [171]. It is also possible that pressure induces a line-splitting. It is clear that further work where diamond samples of higher lattice quality are used should allow for a disentanglement of the pressure and stress effects.

4.4.4 SiV^- Local Vibrational Mode (LVM) at Low and High Temperatures

Along with the previous experiments, an additional set of spectra were captured. These data focused upon the LVM (section 4.1.2.1). This LVM in SiV^- is a small sharp peak which appears approximately 64 meV (lower) away from the ZPL [149] at room temperature and pressure.

This study will attempt to find how this mode is altered and shifted through the application of pressure. This is of large interest as it provides direct information pertaining to the curvature of the potential surfaces of the impurity centres and how it is influenced by pressure or lattice contraction [150].

To our knowledge, no experimental studies have previously reported upon this relation. However the ab-initio calculations by Ekimov *et al.* [149] have predicted a pressure shift for the LVM of 65.87 meV at 10 GPa.

The PSB is significantly less intense than the ZPL and in practice capturing it was not possible in many of the previous experiments. As a result, it was only captured in three runs, all of which used samples from PCD-α. These three runs were carried out at the following conditions, LT with N_2 as the PTM, RT using N_2, and LT with a NaCl PTM.

4.4.4.1 Local Vibrational Mode (LVM) Pressure Shift

Sample Properties			PSB	
Sample	**PTM**	**Temperature**	**LVM (meV)**	**Efficiency**
PCD-α	N_2	295 K	$62.1(4) + 0.58(5) GPa^{-1}$	$98.5(5)\ \% + 0.067(6)\ \% GPa^{-1}$
PCD-α	N_2	11 K	$64.0(2) + 0.57(2) GPa^{-1}$	$94.6(1)\ \% + 0.20(1)\ \% GPa^{-1}$
PCD-α	NaCl	11 K	$63.7(1) + 0.65(1) GPa^{-1}$	$94.0(3)\ \% + 0.27(4)\ \% GPa^{-1}$

Table 4.4: A summary of experimental conditions and results for the SiV^- LVM recorded at high pressure.

In the three series of measurements completed, both ZPL and LVM lines are seen to independently shift with pressure, but not necessarily linearly (not shown). However, when the LVM energy is calculated (difference between the two lines) its relation to pressure is remarkably linear (see Figure 4.19c). The quantitative values of these shifts are shown in Table 4.4.

With respect to the linear shift rates (Figure 4.19c), all three appear to progress at similar rates. The sample in the NaCl PTM is found to deviate the most significantly from the other two samples, likely due to the strain-related effects as discussed in section 4.4.3. Overall, we find the shift rate to be 0.60(5) meV/GPa for this sample. Other individual rates values are reported in Table 4.4.

Calculating this shift at 10 GPa gives a value of 70.0(5) meV which compares well to the theoretical prediction of 65.87 meV at 10 GPa [150]. This experimentally found shift is significantly larger than predicted and may evidence effects beyond the scope of the ab-initio calculation completed by Ekimov *et al.* [150].

It is interesting to note that the initial value of the LVM (at low pressure) appears to be shifted by 2 meV when comparing the LT and RT results. Additional measurements at various temperatures/samples would be required to explain such shifts.

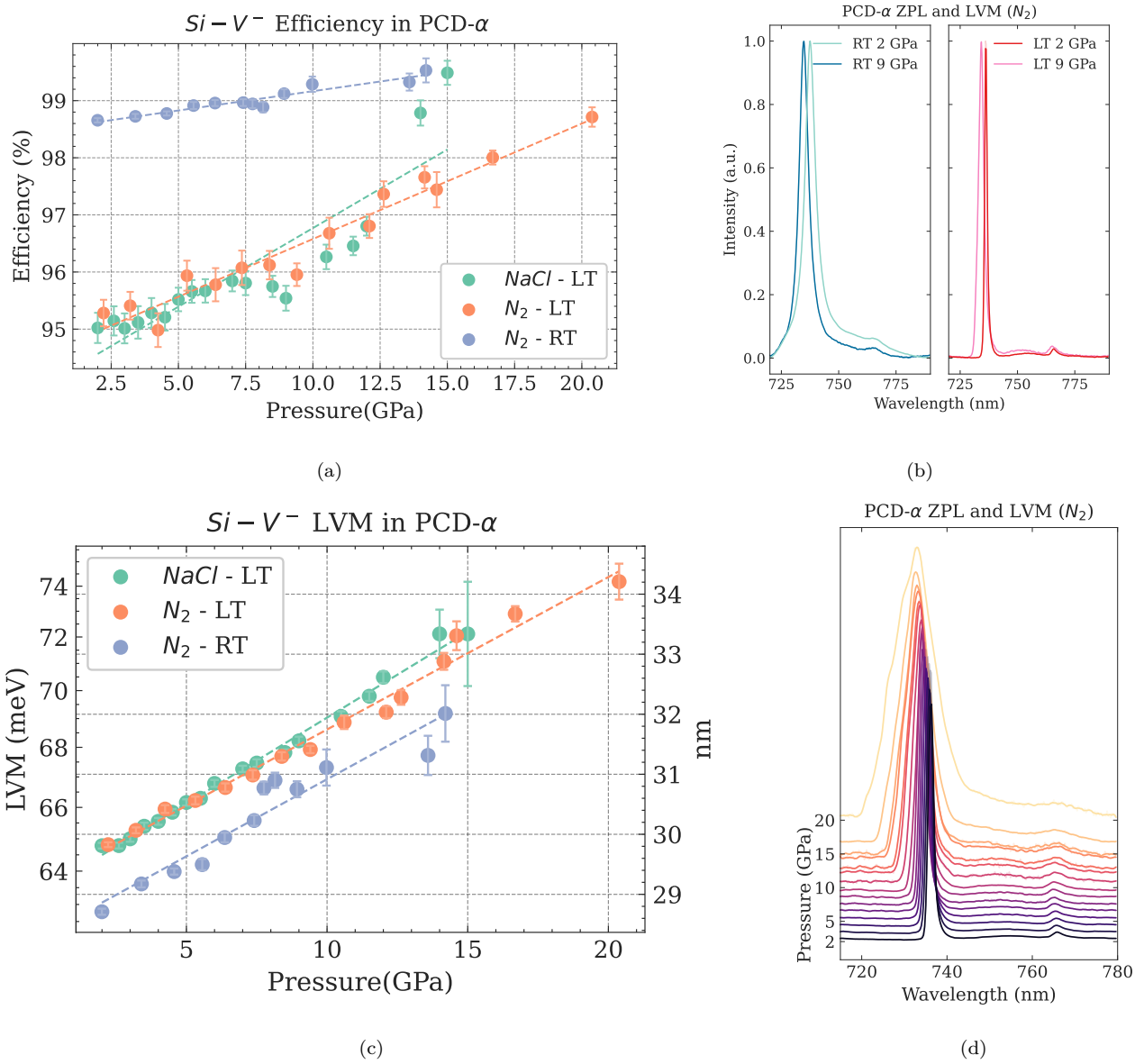

Figure 4.19: Pressure Dependance of the PSB emission for the SiV^- defect in PCD-α a) Efficiency of PL for SiV^- in all three samples. b) Visual comparison of PSB (weak) and ZPL (strong) signals at RT and LT. c) The LVM shift with pressure for all samples. d) Waterfall plot showing the ZPL and PSB at each pressure with a PTM of N_2.

Efficiency Comparison The term efficiency will be used here to quantify the relative intensity of the ZPL and LVM peaks. It will be defined here as: efficiency (%) $= 100\% - \frac{I^{int}_{PSB}}{I^{int}_{ZPL}}$, where I^{int} represents the integrated intensity of the respective peak. Note that this is not photon conversion efficiency, as only the LVM peak will be calculated here. However, at LT it was found in this study that the LVM is the most intense component of the PSB, therefore a reduction in its relative intensity is likely to correspond with an increase in overall photon conversion efficiency.

The efficiency calculated at each temperature for the sample compressed in a different PTM is shown in Figure 4.19a and are reported in Table 4.3. The efficiencies show a significant linear increase as a function of pressure. Additionally, based on this result, it is clear LVM would not emit above 20–30 GPa should the linear relationship still pertain. In any case, an investigation of efficiency in this pressure range has the potential to provide interesting results.

The decrease in intensity of the PSB has been predicted [150], but to our knowledge has not been experimentally validated.

Discussion The analysis of the LVM which is completed here provides experimental results with respect to pressure never presented before. It is found that the pressure shifts the LVM spectral position at a consistent rate, independent of the PTM used and temperature. The rate is 0.60(5) meV/GPa, which is not found to correspond well with a previous theoretical prediction.

In addition, the LVM appears to decrease in intensity with increased pressures. This indicates that the overall PSB may also follow this pattern. If this is the case it could be a major boon for group IV defects as single photon sources, as conversion efficiencies are of high importance. A well intensity calibrated capture of the PSB would allow for the firm establishment of this relationship, additionally, measurements at more elevated pressures (20–30 GPa) would provide an idea of the LVM suppression limits.

4.5 Conclusion of the SiV^- Studies

This chapter marks the end of the experimental results. Over the course of this chapter, an investigation of SiV^- under extreme conditions was presented. Particularly, the study focused on the PL of the SiV^- defect that is altered as a function of pressure and temperature. Although the PCD samples used had significant internal strain, they were useful to first verify the T^3 temperature dependence of the SiV^- defect's emission wavelength.

The samples were then used to establish a linear pressure dependence of 0.96(3) meV/GPa at room pressure and room temperature. This linear dependence is in accordance with relations found for other group IV split vacancy defects. The low temperature, high-pressure data were more difficult to interpret, but indicate that the pressure shift remains linear and is in a similar range of parameters as the room temperature study. A higher quality (lower strain) sample which is able to start with a distinctly visible fine structure could enable a significantly improved dataset.

Finally, the LVM was found to have consistent pressure-related shifts, independent of temperature or sample strain. This shift is measured to be 0.60(5) meV/GPa. Additionally, PSB reductions as a function of pressure were noted, although experimental alterations will be needed to report the photon conversion efficiency accurately.

Overall, the present experiments elucidate novel aspects of the silicon vacancy defect in diamond. Hopefully, the experimental work will serve as an experimental basis to allow for a more complete investigation and a better understanding of SiV^- and group IV defects in diamond.

Sample Properties			**SiV^-**		**PSB**	
Sample	**PTM**	**Temperature**	**Lineshift ($\frac{meV}{GPa}$)**	**Linewidth (meV)**	**LVM (meV)**	**Efficiency**
PCD-$S1$	NaCl	295 K	0.99(2)	$10.5(1) + 0.30(1)\ GPa^{-1}$	-	-
PCD-α	NaCl	295 K	0.97(2)	$9.0(4) + 0.37(6)\ GPa^{-1}$	-	-
PCD-α	N_2	295 K	0.93(1)	$9.35(1) + 0.015(12) GPa^{-1}$	$62.1(4) + 0.58(5) GPa^{-1}$	$98.5(5)\ \% + 0.067(6)\ \% GPa^{-1}$
PCD-α	N_2	11 K	1.23(4)	-	$64.0(2) + 0.57(2) GPa^{-1}$	$94.6(1)\ \% + 0.20(1)\ \% GPa^{-1}$
PCD-α	NaCl	11 K	0.63(1)	-	$63.7(1) + 0.65(1) GPa^{-1}$	$94.0(3)\ \% + 0.27(4)\ \% GPa^{-1}$

Table 4.5: A summary of all experiment conditions and results regarding the SiV^- defect as a function of pressure. This table is a culmination of Tables 4.3 and 4.4.

Chapter 5

Summary and Future Work

The work on which this thesis is based marks the start of a broader research endeavour at the Laboratoire de physique des solides denses of the University of Ottawa to synthesize diamond by the chemical vapour deposition technique in order to achieve tailored properties. Therefore, the main research objectives of the present work were two-fold. The first objective was, to find and control the necessary growth parameters for high quality diamond synthesis. This parameter choice was completed by pre- and post-growth physical characterization. The second objective was to use the grown diamond samples for quantum sensing. Specifically, this work focuses upon the silicon vacancy under extreme conditions. The results of these research objectives, as obtained in this work, are encompassed in two main sections. They are summarized as follows.

Synthesis and Characterization of High Quality Diamond Utilizing a commercial research grade CVD reactor, the practicalities of growing high quality diamond were explored. This includes learning about the CVD technique in general and, more specifically, knowing how the growth technique could be implemented in the available instrument. The work explores the entire process of diamond synthesis with the goal of finding and optimizing the CVD growth parameters. This optimization of growth required a suite of characterization techniques, which when combined gave an overall understanding of how growth parameters affect the quality of diamond. As part of this work, it was also necessary to achieve a certain level of proficiency to be able to efficiently use the different characterization techniques and the results they could provide.

The characterization of physical properties (section 3.2) combined with the adjustment of the many different parameters (section 2.2) enabled an iterative improvement of the growth process (chapter 2), eventually resulting in high-quality samples with the desired tailored characteristics (section 3.4). With this in mind, the study accomplished its goal of synthesizing high quality diamonds.

Specifically, several major milestones in regard to high quality diamond synthesis were achieved. First, a high quality ($<$2 ppm of defects) and reasonably high speed growth ($\sim$10 μm/hr) was attained, which would allow for the synthesis of reasonably large and high quality sample in future research efforts. The high quality growth was also found to be fully single crystalline - with no polycrystalline rim outgrowth. This was the result of a pocketing technique. This achievement *i.e.*, the creation of fully single-crystal diamond without post-processing significantly decreases the fabrication hurdles involved for the use of diamonds for novel research purposes.

As determined through the physical characterization process, our synthesized diamond would

be classified as IIa quality diamond and therefore could be sold commercially as such. However, these grown diamonds provide notable additional laboratory control. This could allow for further intriguing developments at LPSD - such as the creation and use of defects as quantum systems.

The creation of this growth process was a very satisfying achievement on which future work at our research group will be based. Significant work nonetheless remains to further improve diamond samples. In particular, the highest priority targets in future work would be to reduce to a minimum the source of residual nitrogen still present in the diamond samples, and to achieve a diamond surface morphology which is 'smooth'. Both these goals are achievable in the near future.

High Pressure Sensing using the SiV^- defect in diamond During the characterization process of the SCD diamond samples obtained by CVD growth, significant quantities of the SiV^- defect were detected. This defect and similar colour centres are worth studying as quantum systems in diamond that constitute promising candidates to be high sensitivity optically accessible quantum sensors, single photon sources, and qubits.

Given the defects' potential as sensors for extreme condition studies of condensed matter, several diamond samples were synthesized and studied to examine the SiV^- defect at high pressure and low temperature. Moreover, observations of its corresponding photoluminescence were studied as the samples were cooled (down to 11 K) and compressed (up to 17 GPa) in diamond anvil cells.

The experiments were successful in exploring the low temperature behaviour of the SiV^- defect's photoluminescence signal. The results obtained were seen to match roughly those found in literature (section 4.4.1).

Additionally, the SiV^- photoluminescence was recorded under high quasi-hydrostatic pressure, at both low and room temperatures. The results from the high pressure studies were found to agree well with both the computational and the experimental behaviour of similar group IV defects, as found in the literature. Finally, experiments completed under simultaneous low temperature (down to 11 K) and high pressure (up to 17 GPa) are promising to use the photoluminescence of the SiV^- defect as a sensor to monitor extreme conditions impinged on a sample in a diamond anvil cell. Thus a further refined investigation, with a better quality diamond sample is needed for further-promising-work. It is hoped that the present work has paved the way in achieving this goal in the near future. Research along that line is continuing at LPSD, the Laboratoire de physique des solides denses at the University of Ottawa.

To the best of our knowledge, this work is the first to study the behaviour of a group IV defect local vibrational mode (LVM) under high pressures. The LVM of SiV^- appears to shift linearly with pressure at a rate of 0.60(5) meV/GPa. This linear shift is consistent when samples were compressed in different PTMs or temperatures. While the pressure-related shift is found with high accuracy in our experiments, it deviates from previously published computational work [150]. Further exploration of the reason for the observed deviation is warranted. Our experiments also indicate an improved photon conversion efficiency under high pressures which, if substantiated, could prove useful to improve group IV defects as quantum sensors. This could particularly improve their usefulness as good sensors for extreme condition research. Among those are:

Future Work

- Implement slicing (laser cutting) procedures to isolate the grown diamond from the initial seed and begin polishing the diamond surfaces;
- Ensure consistency of power density throughout synthesis;

- Determine and eliminate the unintentional nitrogen source(s) in our system;
- Complete the characterization of the misorientation angle and use a non-zero angle for growth;
- Carry out quantitative birefringence measurements to monitor strain in the sample;
- Explore of addition oxygen during the growth process and control of the effect on the diamond characteristics;
- Complete simulations of the electrical field around the sample and the distribution of the plasma ion species to explore various parameters quickly and efficiently, such as any changes on reactor geometry;
- Investigate more detailed and elaborate high pressure studies of the SiV^- defect, including studies to higher pressures;
- Perform secondary ion mass spectroscopy (SIMS) to determine quantity of silicon and nitrogen in the grown diamond; and
- Pursue the growth and study of SiV^0 under extreme conditions.

In brief, the present work will ideally be used as the stepping stone to what could prove as a rich and fascinating research area in the near future.

Appendices

Appendix A

Diamond Growth with Silicon Vacancies

A.1 Introduction

In chapter 4, a study of the SiV^- defect in diamond is presented. To examine these imperfect diamonds under high pressures, samples with thicknesses below 30 μm were required. In practice, thin films of PCD were selected for this purpose. This appendix explores the synthesis conditions and physical characterization of these thin PCD films preceding their further study under low temperatures and high pressures.

The four samples under assessment were: PCD-α, PCD-β, PCD-$S1$, and PCD-$S2$. Their general properties are listed in Table 4.1 and their growth parameters in Table A.1.

A.2 Growth

The PCD samples can be divided into two groups; those synthesized alongside SCD samples (PCD-α and PCD-β), and those grown specifically to create polycrystalline diamond (PCD-$S1$ and PCD-$S2$). The samples growth processes are described as:

PCD-β This sample was nucleated upon an unpolished 99.9% molybdenum disk alongside SCD diamond. The deposition lasted for 48 hours, with 800 sccm of total gas flow, a gas mixture of 4% methane, 96% hydrogen at a pressure of 250 mbar, a microwave power of 4.5 kW and at a substrate temperature of 1100°C. This process was similar to that utilized for the synthesis of SCD-α (Section 3.4) and used the same pocket cutout in the centre of the molybdenum disk. However, the sample height was not tracked and no oxygen was included during deposition.

Sample	Length (hrs)	CH_4 (%)	Temperature	Pressure (mbar)	Power (kW)	In Chamber
PCD-β	48	4%	1100°C	250	4.5	SCD pocketed
PCD-α	24	4%	850°C	160	4.0	SCD, unpocketed
PCD-$S1$	21	2%	850°C	140	4.0	solid silicon
PCD-$S2$	21	2%	950°C	140	4.0	N/A

Table A.1: Summary of various parameters used to grow the PCD films

PCD-α The second sample fabricated alongside a SCD seed was that of PCD-α, which was synthesized alongside two unpocketed HPHT SCD samples. The deposition lasted for 24 hours, with 800 sccm of total gas flow at a 4% methane, 96% hydrogen mixture with a pressure of 160 mbar and a microwave power of 4.0 kW. Attempts were made to regulate the substrate temperature to 850°C. Due to thin film interference, the pyrometer gave erroneous readings, and the temperature had several significant fluctuations early in the growth. The PCD was grown upon a polished molybdenum disk (99.9%).

PCD-$S1$/PCD-$S2$ These two samples were deposited under similar conditions to each other. The synthesis lasted for 21 hours, with a methane percentage of 2%, hydrogen of 98%, total flow of 800 sccm, chamber pressure of 140 mbar and a power of 4.0 kW. PCD-$S1$ was synthesized at 850°C and on an unpolished molybdenum substrate (R_{RMS} = 1.6 μm), while PCD-$S2$ was grown at 950°C on a polished molybdenum substrate (R_{RMS} = 0.25 μm). Finally, while PCD-$S2$ was not intentionally doped, PCD-$S1$ had solid silicon in the chamber. The silicon pieces used were boron doped and had a resistivity of 0.001 - 0.005 Ωcm (10^{19} - 10^{20} cm^{-3}).

A.3 Physical Characterization

The PCD samples characterization follow the procedures presented in section 3.2. For these thin samples, however, not all methodologies could be used. The characterization techniques that were used are thickness determination, Raman/PL, FTIR, SEM, and optical microscopy.

Thickness Determination Thickness is the primary limiting factor which inhibits a diamond sample's use in high-pressure studies. Therefore, it is important to characterize that dimension accurately. A Mitutoyo micrometer (with a precision of ± 1 μm) was used to complete this measurement. Unfortunately, the sample height varied significantly over the substrate surface, leading to substantial variations in the measurements depending on location. For this reason, several points sourced from various areas of the film were measured and thicknesses were averaged, leading to significant uncertainties. The substrate thicknesses were: PCD-β at 570±30 μm, PCD-α at 22±5 μm, PCD-$S1$ at 18±5 μm and PCD-$S2$ at 18±5 μm. Note that PCD-β was substantially thicker than the other films, and therefore was only studied at room pressure.

A.3.1 Optical Microscopy

By allowing a measurement of many crystallites, optical microscopy allows for a convenient method to survey of grain size for a given sample. Determination of the value was completed by measuring 50 grains. These results were : PCD-β - 99 ± 42 μm, PCD-α 4.2 ± 1.2 μm, PCD-$S1$ - 7.9 ± 1.7 μm and PCD-$S2$ - 16.9 ± 3.2 μm. It is clear that the markedly thicker sample (PCD-β) allowed for significant increases in grain size, this matches expectations [80]. The differences between films are broadly related to the altering of growth parameters, such as surface temperature [189], silicon concentration [183], and gas phase nitrogen content [190].

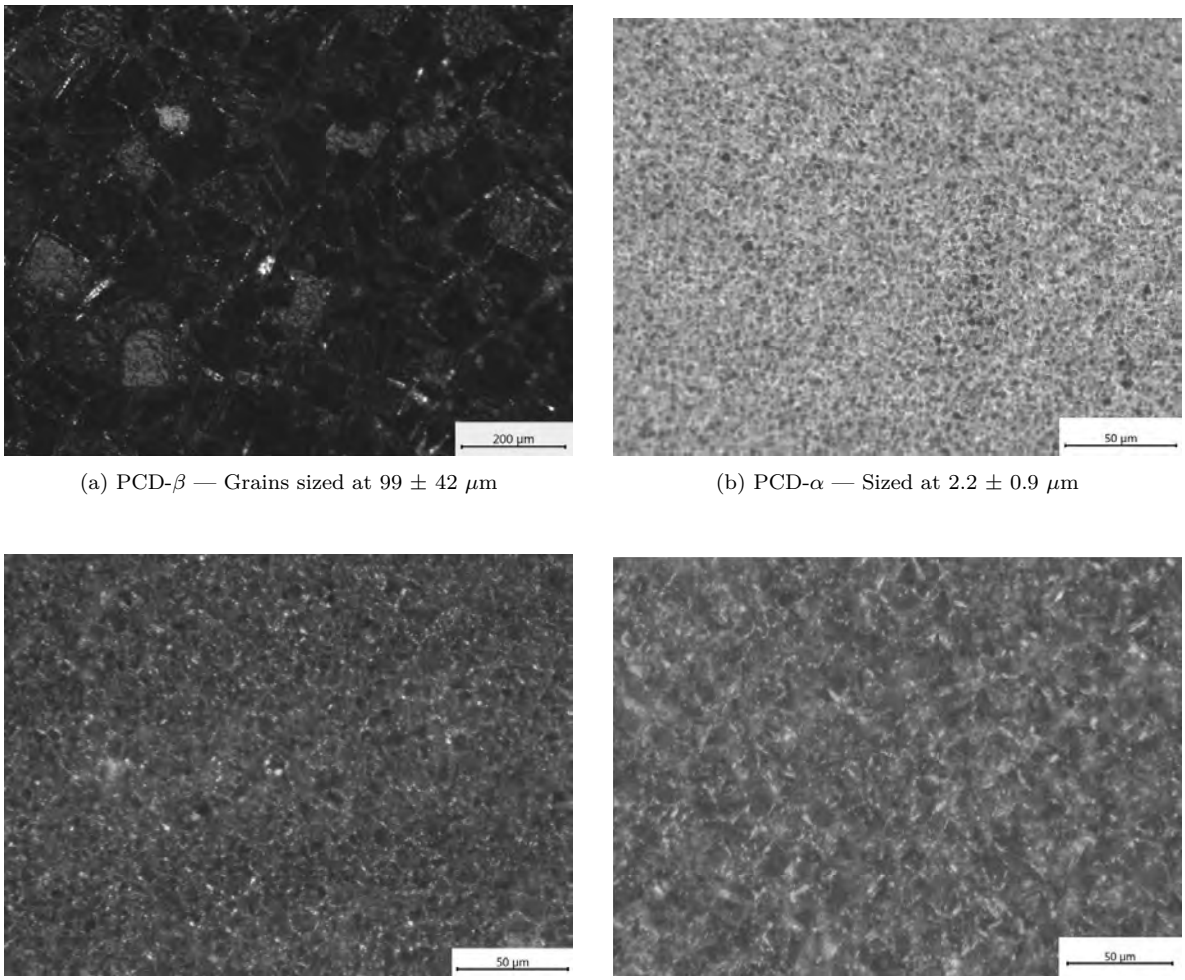

(a) PCD-β — Grains sized at 99 ± 42 μm

(b) PCD-α — Sized at 2.2 ± 0.9 μm

(c) PCD-$S1$ — Sized at 3.3 ± 1.3 μm

(d) PCD-$S2$ — Sized at 8.9 ± 3.2 μm

Figure A.1: Optical microscopy of several PCD diamond films. These photos were used primarily to estimate the grain size of the samples. Reported uncertainties are measured based upon the standard deviation of 50 grains.

A.3.2 Raman Spectroscopy / Photoluminescence

As Raman/PL signals are not significantly affected by scattering of light or by thin film interference, these corresponding spectra were the primary tools for diagnosis of the PCD samples. Additionally, as these selected samples will be used to study the SiV^- PL line, as presented in Chapter 4, the characterization of this emission is of critical importance.

Figure A.2a shows the entire spectral region of interest (550–800 nm) which was emitted from the sample, excited by a laser light at 532 nm. These spectra are scaled to the maximum intensity of the SiV^- line. It is noted that scaling with respect to the intensity of the diamond ZPL line would not have allowed for the observation of all features, as there is a large variance in SiV^- PL intensity.

There are three main areas of interest worth exploring in each of the Raman/PL spectra: the diamond first order Raman line, nitrogen defects and silicon vacancy PL emission line.

The diamond Raman line for different samples is shown in Figure A.2b. The quality of these diamonds were low, due to their PCD nature, leading to a significant Raman line broadening. PCD-β and PCD-α show narrow linewidths (3.28 cm^{-1} and 3.44 cm^{-1} respectively) when compared to

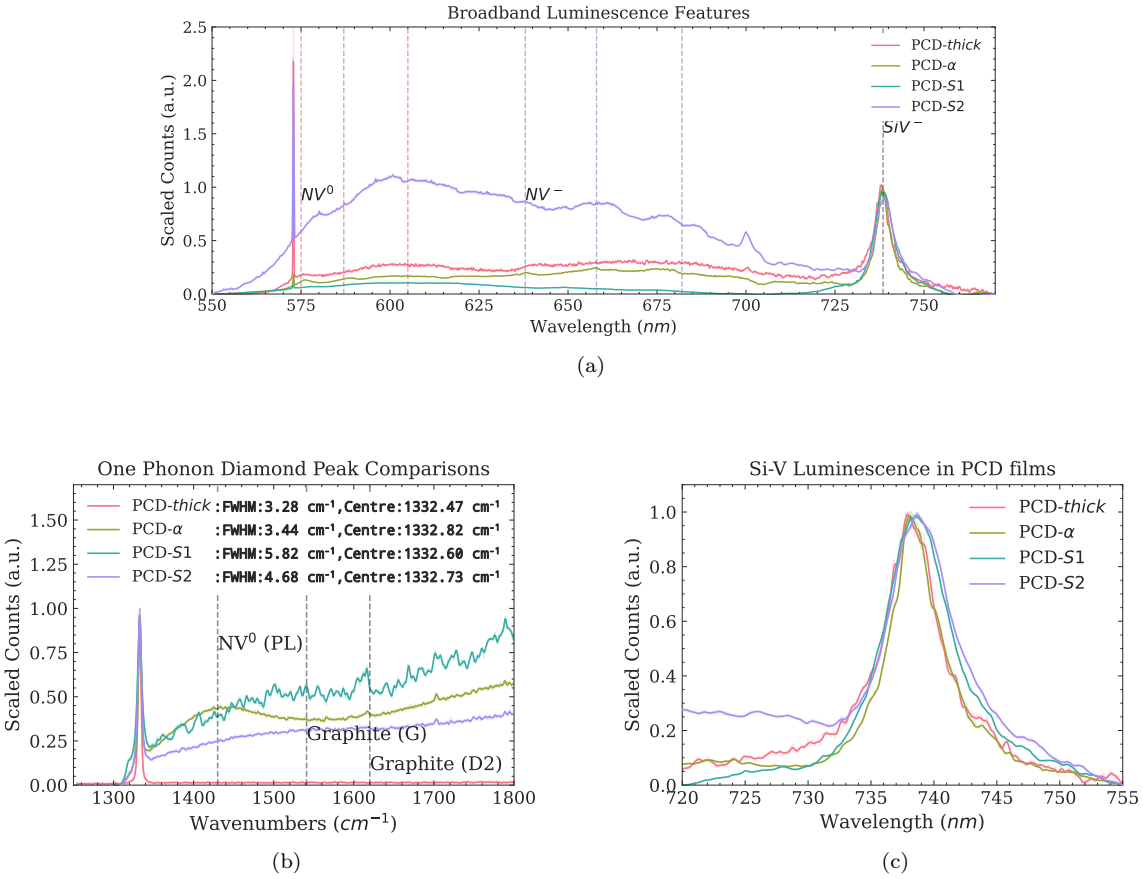

Figure A.2: Graphs showing Raman spectroscopy/photoluminescence spectra of the PCD samples as excited by a 532 nm laser. a) The entire range under study. Broad photoluminescence signals, specifically those arising from the NV^- and NV^0 defects are particularly prominent. Data are scaled to the maxima of the SiV^- PL line b) Raman scattering of the one phonon line and several known graphite signals as indicated by the dotted lines. c) The SiV^- ZPL, normalized, to emphasize the differences in linewidths among samples.

PCD-$S1$ and PCD-$S2$ (5.82 cm^{-1} and 4.68 cm^{-1}, respectively). The improvement in Raman line width indicates a significantly higher crystalline quality in PCD-β and PCD-α. This is easily explained in PCD-β by its large grain size and likely reduced residual strains. A hypothesis arising from SEM/FTIR measurements is presented below to describe the high crystalline quality in PCD-α.

The line shift for the diamond Raman line in the various samples was relatively low (0.03 - 0.3 cm^{-1}) and should be related to internal tensile strains, local heating (from laser illumination) and defect concentrations. These effects are difficult to disentangle in this case, therefore no estimate of strain will be reported.

The PL nitrogen defects in the films are illustrated in Figure A.2a. All samples showed significant quantities of nitrogen vacancy defects, given the relatively strong corresponding PL intensities. Additionally, the PL ratio of NV^0 (580 nm) to NV^- (637 nm) differed between each film. As the ZPL and PSB are overlapping, it is difficult to determine accurate ratios. PCD-$S1$ and PCD-$S2$ have larger NV^0 bands, while the opposite is true for PCD-β and PCD-α. This is an indicator of donor/acceptor abundances within the PCD [134].

The final signature considered to characterize the PCD samples was that of the PL from the

SiV^- defect. Silicon is a common impurity in CVD growth processes, and without strict control it is often incorporated in diamond [101, 191]. Our known silicon sources are the plasma etching of quartz window and the quartz shower head dome, heating of a Viton O-ring and residual silicon in the chamber from previous growths upon silicon wafers. Additionally, for sample PCD-$S1$ solid silicon was intentionally introduced into the CVD chamber during growth.

The integrated intensity of the SiV^- PL emission is normalized to diamond thickness by taking the ratio of the PL line intensity to the integrated intensity of the diamond Raman line. These data are presented in Table 4.1. Based on these results, the samples can be split into two groups. The first group relates to the high intensity lines PCD-α and PCD-$S1$ which have ratios of 154.7 and 237.5 respectively. Then in a second group are the low-intensity SiV^- samples PCD-β and PCD-$S2$ (12.6 and 10.3 respectively).

As the SiV^- PL intensity is known to vary non-monotonically with silicon quantity during deposition [183], no characterization of the defect can be completed based upon these data. It is notable that there is an intensely luminescing silicon defect in PCD-α without an intentionally introduced silicon source.

The silicon vacancy defect is particularly sensitive to strain: higher strains correlate to increased linewidths [192]. Based on that information, the least to most strained samples as per the FWHM measures are: PCD-α (4.4 nm), PCD-β (4.9 nm), PCD-$S2$ (5.2 nm), and PCD-$S1$ (5.6 nm). However, to our knowledge, a quantitative relationship between strain and linewidth has not been reported.

This characterization of the silicon vacancy shows the PCD-α sample with a remarkably intense yet narrow PL signature in comparison to the other samples. The incidence of lower strain in this sample is likely the cause of its narrow ZPL linewidth. Due to its high quality, although its growth parameters were less controlled, PCD-α is used heavily in our study presented in Chapter 4.

A.3.3 Infrared Absorption

Due to the high scattering nature of the PCD samples and the thin film interference inherent in the samples themselves, these data from the PCD samples' IR absorption are not of desired quality and hence are less useful. Particularly, the recorded IR spectra preclude the feasibility of study in the one phonon range.

As seen in Figure A.3, the diamond three-phonon spectral region (2666-4000 cm^{-1} [101, 193]) has a significantly absorbing portion (2700-3100 cm^{-1}). Our analysis focuses on these spectral features.

The first IR absorption line (2820 cm^{-1}), strong in PCD-β and PCD-$S2$ is suggestive of significant hydrogen at the diamond grain boundary [194].

The other bands visible in this range are caused by C-H bonds on non-{100} faces. Note that while there are studies linking these growth faces to absorption bands, the links have not been systematically verified. This analysis should therefore serve solely as a rough gauge of growth dynamics.

Three main bands which correlate with growth faceting are visible, these are the absorption bands at 2854 cm^{-1} relating to {100} facets, 2923 cm^{-1} for {111} facets [194] caused by sp^3-hybridized CH_2 and the doublet at 2875 cm^{-1}/ 3025 cm^{-1} for {110} facets which is induced by sp2-hybridized CH_2 [101].

It can be seen that PCD-$S1$ and PCD-α showed significant {100} related IR absorption, while

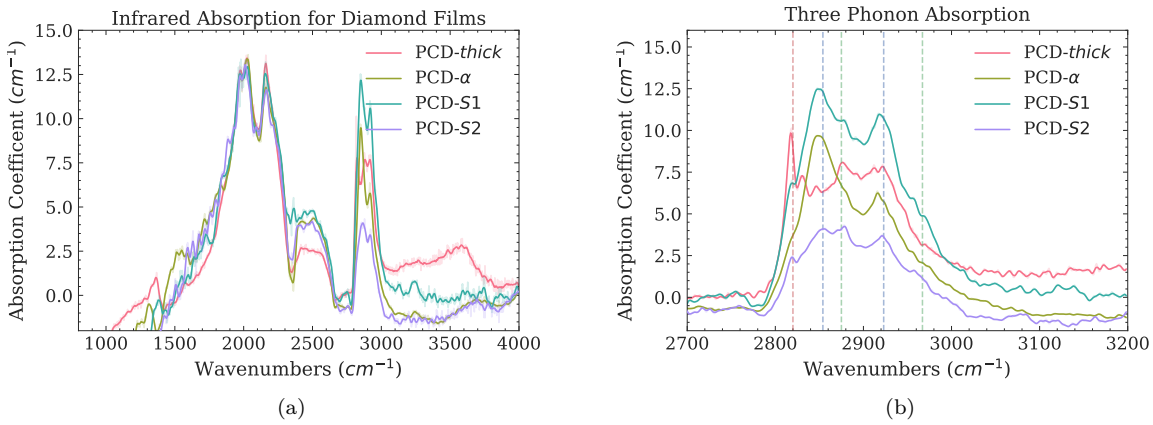

Figure A.3: Graphs showing IR absorption spectra as measured through the technique of FTIR. The one phonon region (1000-1333 cm^{-1}) is dominated by interference and noise, and hence is not reliable. a) Broad mid-IR absorption spectra for each sample. b) Three-phonon region focusing upon hydrogen termination (red), sp^3 C-H stretch on {100}/{111} (blue) and sp^2 C-H doublet on 110 (green).

PCD-β was dominated by {110}/{111} facet growth and PCD-$S2$ appears to have major contributions from all IR absorption bands. Determining the cause of this effect could be an aim for future work.

It has been noted previously that the silicon/carbon ratio plays a large role in morphology and growth rates for films [183] and this is uncontrolled for this CVD process.

Additionally, N_s^0 is undetected at 2688 cm^{-1} for all samples, bounding the concentrations of this defect under 5.4 ppm [195].

A.3.4 SEM

Use of SEM allows for qualitative evaluation of the growth morphologies. All PCD samples except PCD-$S2$ were imaged by SEM. The analysis of the grain size led to significant differences, with the measurements of PCD-α giving 7.3 $\pm$ 2.7 μm, PCD-$S1$ 12.9 $\pm$ 2.5 μm and PCD-β 140 $\pm$ 52 μm. This is a 60% larger for the small-grained films.

Additionally, the morphology of the grains was assessed. PCD-β was seen to have a cubic {100} morphology, while PCD-α appeared to have an octagonal {111} form and PCD-$S1$ had a cubo-octahedral shape [196]. Notably, the two thin films were not well faceted, possibly caused by intersection with other nearby nucleated grains. The cubo-octahedral form and lack of distinct faceting were consistent with the results of the measurements by FTIR spectroscopy. Additional work to optimize synthesis parameters would be needed to have well-defined morphologies.

It is also interesting to observe the morphology of PCD-$S1$ which showed twinned (pyramidal) growth upon the surface. This surface morphology is typically associated with a lower quality growth [47]. Further optimization of the synthesis parameters could enable higher quality films. The next step in this process would involve shifting the α parameter outside the 1 - 1.5 range (See table 2.1). The most effective route to achieve this may be increasing the substrate temperature.

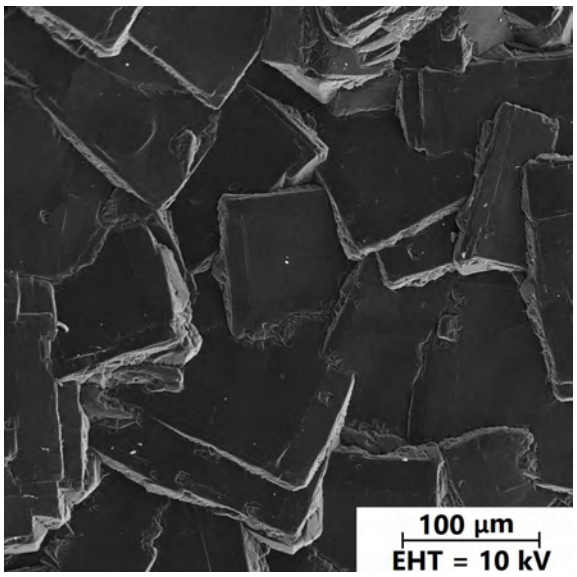

(a) PCD-β

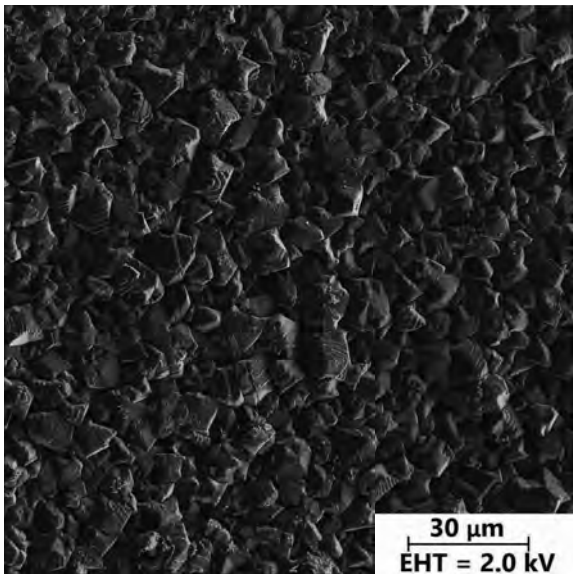

(b) PCD-α

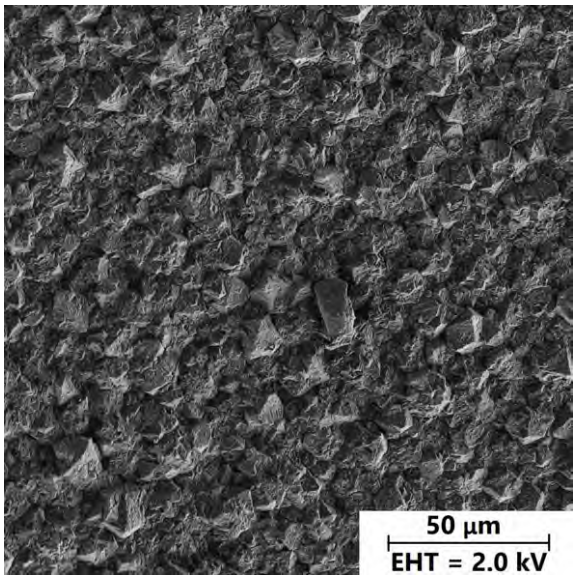

(c) PCD-$S1$

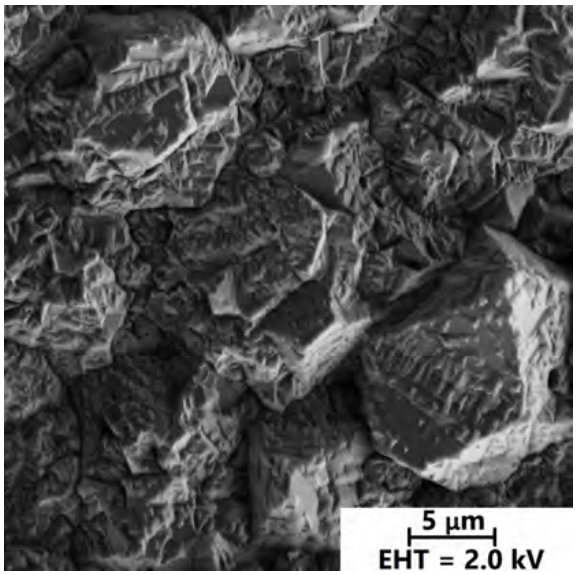

(d) PCD-$S1$ — Twinning

Figure A.4: Scanning electron microscopy images of several PCD diamond films. These photographs illustrate primarily the surface morphologies of the various films. PCD-$S2$ was not imaged.

A.4 Remarks for Future Work

To enable optimal SiV^- PL emission within the PCD thin films, a combination of high-quality diamond, intense SiV^- photoluminescence, and thin sections were required. Through the control of growth parameters and sample characterization, several viable PCD films were created. These samples have been used for further studies, as is discussed in Chapter 4. Further refinements are required to enable consistently 'high quality' growth. The optimization of growth parameters would lead for example to the reduction of twinning, increase of grain size, and a better understanding

of silicon doping.

Twinning can be eliminated through the shifting of parameters; for instance, it is recommended that a change in substrate temperature be employed to adjust this α parameter. This should enable higher quality synthesis, as the number of structural defects should be decreased (3.3).

The increase of grain size correlates to higher quality diamond, as a lower surface area leads to a lower ratio of diamond grain boundaries to solid diamond. This should be optimized through a sequence of iterative parameter selection [189].

It is essential that an optimization of parameters be studied to determine the optimal level of silicon doping for the chosen growth process, due to the non-monatomic nature of silicon doping. Also, further investigation into the relation of doping to photoemission should be completed. To enable this fine control, a gaseous source of silicon as opposed to the use of solid silicon is recommended for that purpose. Silane or tetramethylsilane could be used as sources of silicon [183].

Appendix B

Nitrogen Vacancy Observed under Pressure at 11 K

In addition to the SiV^- PL line which is analyzed in Chapter 4, other lines are tracked in the PCD-α compressed in an - N_2 PTM. In particular, NV^- PL will be presented.

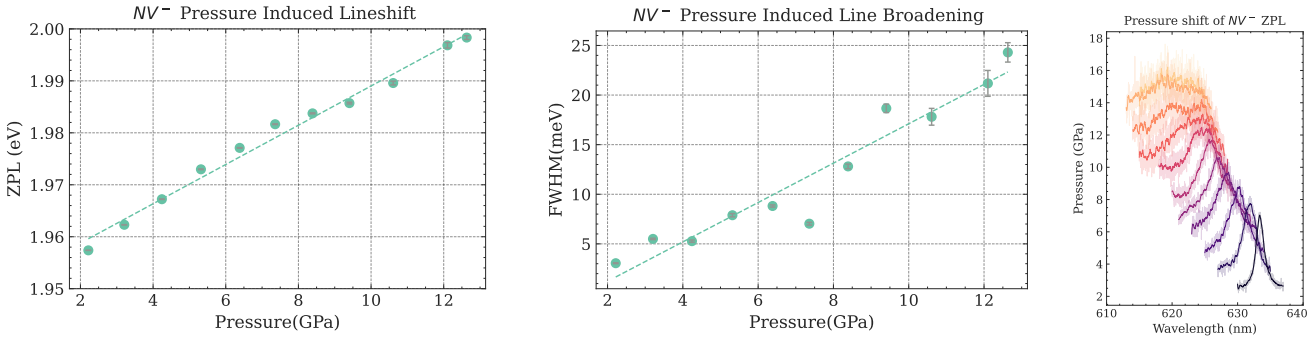

(a) (b) (c)

Figure B.1: Study of NV^- pressure dependence in PCD-α at LT with an N_2 PTM a) ZPL shift dependent on pressure. b) Line broadening related to pressure increase. c) Cascade plot showing the NV^- luminescence at various pressures.

NV^- When fit with a linear function, the relationship for the corresponding energy of the line is 1.951(1) eV + 3.78(1) meV/GPa, additionally the pressure-related broadening is given as -3(2) meV + 2.0(2) meV/GPa. This linear fit is significantly different from that reported in previous studies (5.5-5.8 meV/GPa). However, all other studies were completed at room temperature. [162–164]. A quadratic fit to the data gives 1.947(2) eV + 5.29(6) meV/GPa - 0.10(4) meV/GPa^2. This result matches well the relationship given by Lyapin *et al.* [147].

It is additionally noted that the pressure broadening of the NV^- centre PL in combination with a reduction in intensity at elevated pressure necessarily means that the spectra become noisy above ∼7 GPa. Line splitting is also observed. It is hypothesized that a significant sample strain is the primary cause of deviation from the linear relationship, as opposed to a drastic shift in pressure sensitivity.

As the NV^- signal is within the PSB of NV^0, is difficult to observe among lower quality diamond samples. In combination with the significant peak broadening (10x larger than for SiV^-) shows the deficiencies of NV^- as an optimal sensor for extreme conditions research.

As only one sample is analyzed, and effects of non-hydrostatic conditions are convolved with the high pressure effects, it is difficult to draw any clear conclusions. However, it can be stated that the limited data found here agree with those of Lyapin *et al.* [147], although the cause of the second order pressure dependence reported from their study remains at this point unknown.

Bibliography

[1]F. P. Bundy, H. T. Hall, H. M. Strong, and R. H. Wentorfjun., "Man-Made Diamonds", Nature **176**, 51–55 (1955).

[2]V. V. Danilenko, "On the history of the discovery of nanodiamond synthesis", Physics of the Solid State **46**, 595–599 (2004).

[3]M. L. Markham, J. M. Dodson, G. A. Scarsbrook, D. J. Twitchen, G. Balasubramanian, F. Jelezko, and J. Wrachtrup, "CVD diamond for spintronics", Diamond and Related Materials **20**, 134–139 (2011).

[4]K. Liu, S. Zhang, B. Liu, M. Xu, Z. Ren, P. Qiao, J. Xue, X. Zhang, G. Shu, J. Zhao, M. Sun, D. Dzmitrovich, L. Yang, J. Han, B. Dai, and J. Zhu, "Investigating the energetic band diagrams of oxygen-terminated CVD grown e6 electronic grade diamond", Carbon **169**, 440–445 (2020).

[5]C. J. H. Wort and R. S. Balmer, "Diamond as an electronic material", Materials Today **11**, 22–28 (2008).

[6]J. F. Barry, J. M. Schloss, E. Bauch, M. J. Turner, C. A. Hart, L. M. Pham, and R. L. Walsworth, "Sensitivity optimization for NV-diamond magnetometry", Reviews of Modern Physics **92**, 015004 (2020).

[7]M. Pompili, S. L. N. Hermans, S. Baier, H. K. C. Beukers, P. C. Humphreys, R. N. Schouten, R. F. L. Vermeulen, M. J. Tiggelman, L. dos Santos Martins, B. Dirkse, S. Wehner, and R. Hanson, "Realization of a multinode quantum network of remote solid-state qubits", Science **372**, 259–264 (2021).

[8]N. Savage, "Quantum diamond sensors", Nature **591**, S37–S37 (2021).

[9]B. Hoefflinger, "IRDS—International Roadmap for Devices and Systems, Rebooting Computing, S3S", in *NANO-CHIPS 2030: On-Chip AI for an Efficient Data-Driven World*, edited by B. Murmann and B. Hoefflinger, The Frontiers Collection (Springer International Publishing, Cham, 2020), pp. 9–17.

[10]I. R. Committee, *International Roadmap for Devices and Systems 2020* (IEEE, 2020).

[11]H. P. Bovenkerk, "Abrasive materials", in *Mineralogy* (Springer US, Boston, MA, 1983), pp. 1–2.

[12]M. I. Eremets, I. A. Trojan, P. Gwaze, J. Huth, R. Boehler, and V. D. Blank, "The strength of diamond", Applied Physics Letters **87**, 141902 (2005).

[13]T. Meier, T. Herzig, and J. Haase, "Moissanite anvil cell design for giga-pascal nuclear magnetic resonance", Review of Scientific Instruments **85**, 043903 (2014).

[14]N. Yang, ed., *Novel Aspects of Diamond: From Growth to Applications*, Vol. 121, Topics in Applied Physics (Springer International Publishing, Cham, 2019).

[15]G. Turri, S. Webster, Y. Chen, B. Wickham, A. Bennett, and M. Bass, "Index of refraction from the near-ultraviolet to the near-infrared from a single crystal microwave-assisted CVD diamond", Optical Materials Express **7**, 855 (2017).

[16]P. T. B. Shaffer, "Refractive Index, Dispersion, and Birefringence of Silicon Carbide Polytypes", Applied Optics **10**, 1034–1036 (1971).

[17]J. Carvill, "3 - Thermodynamics and heat transfer", in *Mechanical Engineer's Data Handbook*, edited by J. Carvill (Butterworth-Heinemann, Oxford, Jan. 1, 1993), pp. 102–145.

[18]P. Loubeyre, F. Occelli, and P. Dumas, "Synchrotron infrared spectroscopic evidence of the probable transition to metal hydrogen", Nature **577**, 631–635 (2020).

[19]C. G. Salzmann, J. S. Loveday, A. Rosu-Finsen, and C. L. Bull, "Structure and nature of ice XIX", Nature Communications **12**, 3162 (2021).

[20]E. Snider, N. Dasenbrock-Gammon, R. McBride, M. Debessai, H. Vindana, K. Vencatasamy, K. V. Lawler, A. Salamat, and R. P. Dias, "Room-temperature superconductivity in a carbonaceous sulfur hydride", Nature **586**, 373–377 (2020).

[21]R. Matsumoto, Y. Sasama, M. Fujioka, T. Irifune, M. Tanaka, T. Yamaguchi, H. Takeya, and Y. Takano, "Note: Novel diamond anvil cell for electrical measurements using boron-doped metallic diamond electrodes", Review of Scientific Instruments **87**, 076103 (2016).

[22]M. N. R. Ashfold, J. P. Goss, B. L. Green, P. W. May, M. E. Newton, and C. V. Peaker, "Nitrogen in Diamond", Chemical Reviews **120**, 5745–5794 (2020).

[23]M. W. Doherty, N. B. Manson, P. Delaney, F. Jelezko, J. Wrachtrup, and L. C. L. Hollenberg, "The nitrogen-vacancy colour centre in diamond", Physics Reports, The Nitrogen-Vacancy Colour Centre in Diamond **528**, 1–45 (2013).

[24]L. G. Steele, M. Lawson, M. Onyszczak, B. T. Bush, Z. Mei, A. P. Dioguardi, J. King, A. Parker, A. Pines, S. T. Weir, W. Evans, K. Visbeck, Y. K. Vohra, and N. J. Curro, "Optically detected magnetic resonance of nitrogen vacancies in a diamond anvil cell using designer diamond anvils", Applied Physics Letters **111**, 221903 (2017).

[25]S. Hsieh, P. Bhattacharyya, C. Zu, T. Mittiga, T. J. Smart, F. Machado, B. Kobrin, T. O. Höhn, N. Z. Rui, M. Kamrani, S. Chatterjee, S. Choi, M. Zaletel, V. V. Struzhkin, J. E. Moore, V. I. Levitas, R. Jeanloz, and N. Y. Yao, "Imaging stress and magnetism at high pressures using a nanoscale quantum sensor", Science **366**, 1349–1354 (2019).

[26]M. Lesik, T. Plisson, L. Toraille, J. Renaud, F. Occelli, M. Schmidt, O. Salord, A. Delobbe, T. Debuisschert, L. Rondin, P. Loubeyre, and J.-F. Roch, "Magnetic measurements on micrometer-sized samples under high pressure using designed NV centers", Science **366**, 1359–1362 (2019).

[27]K. Y. Yip, K. O. Ho, K. Y. Yu, Y. Chen, W. Zhang, S. Kasahara, Y. Mizukami, T. Shibauchi, Y. Matsuda, S. K. Goh, and S. Yang, "Measuring magnetic field texture in correlated electron systems under extreme conditions", Science **366**, 1355–1359 (2019).

[28]A. P. Bolshakov, V. G. Ralchenko, V. Y. Yurov, A. F. Popovich, I. A. Antonova, A. A. Khomich, E. E. Ashkinazi, S. G. Ryzhkov, A. V. Vlasov, and A. V. Khomich, "High-rate growth of single crystal diamond in microwave plasma in CH4/H2 and CH4/H2/Ar gas mixtures in presence of intensive soot formation", Diamond and Related Materials **62**, 49–57 (2016).

[29]J. Achard, A. Tallaire, R. Sussmann, F. Silva, and A. Gicquel, "The control of growth parameters in the synthesis of high-quality single crystalline diamond by CVD", Journal of Crystal Growth **284**, 396–405 (2005).

[30]A. P. Bolshakov, V. G. Ralchenko, G. Shu, B. Dai, V. Y. Yurov, E. V. Bushuev, A. A. Khomich, A. S. Altakhov, E. E. Ashkinazi, I. A. Antonova, A. V. Vlasov, V. V. Voronov, Y. Y. Sizov, S. K. Vartapetov, V. I. Konov, and J. Zhu, "Single crystal diamond growth by MPCVD at subatmospheric pressures", Materials Today Communications **25**, 101635 (2020).

[31]L. Mehmel, R. Issaoui, A. Tallaire, V. Mille, O. Brinza, L. Nicolas, G. Hétet, and J. Achard, "Self-Assembled Silica Nanoparticles for Diamond Nano-Structuration", physica status solidi (a) **215**, 1800391 (2018).

[32]K. Yao, B. Dai, J. Zhu, V. Ralchenko, G. Shu, J. Zhao, P. Wang, B. Liu, G. Gao, M. Sun, K. Liu, Z. Lv, L. Yang, and J. Han, "Diamond micropowder synthesis via graphite etching in a microwave hydrogen plasma", Powder Technology **322**, 124–130 (2017).

[33]S. Nad, A. Charris, and J. Asmussen, "MPACVD growth of single crystalline diamond substrates with PCD rimless and expanding surfaces", Applied Physics Letters **109**, 162103 (2016).

[34]A. Croot, E. J. D. Mahoney, H. Dominguez-Andrade, M. N. R. Ashfold, and N. A. Fox, "Diamond chemical vapor deposition using a zero-total gas flow environment", Diamond and Related Materials **109**, 108011 (2020).

[35]B.-C. Gallheber, M. Fischer, M. Mayr, J. Straub, and M. Schreck, "Growth, stress, and defects of heteroepitaxial diamond on Ir/YSZ/Si(111)", Journal of Applied Physics **123**, 225302 (2018).

[36]D. G. Goodwin, "Scaling laws for diamond chemical-vapor deposition. I. Diamond surface chemistry", Journal of Applied Physics **74**, 6888–6894 (1993).

[37]F. Silva, J. Achard, O. Brinza, X. Bonnin, K. Hassouni, A. Anthonis, K. De Corte, and J. Barjon, "High quality, large surface area, homoepitaxial MPACVD diamond growth", Diamond and Related Materials, Proceedings of Diamond 2008, the 19th European Conference on Diamond, Diamond-Like Materials, Carbon Nanotubes, Nitrides and Silicon Carbide **18**, 683–697 (2009).

[38]K. Hassouni, F. Silva, and A. Gicquel, "Modelling of diamond deposition microwave cavity generated plasmas", Journal of Physics D: Applied Physics **43**, 153001 (2010).

[39]J. Ma, M. N. R. Ashfold, and Y. A. Mankelevich, "Validating optical emission spectroscopy as a diagnostic of microwave activated CH4/Ar/H2 plasmas used for diamond chemical vapor deposition", Journal of Applied Physics **105**, 043302 (2009).

[40]Y. A. Mankelevich and P. W. May, "New insights into the mechanism of CVD diamond growth: Single crystal diamond in MW PECVD reactors", Diamond and Related Materials, Proceedings of Diamond 2007, the 18th European Conference on Diamond, Diamond-Like Materials, Carbon Nanotubes, Nitrides and Silicon Carbide **17**, 1021–1028 (2008).

[41]S. J. Harris and D. G. Goodwin, "Growth on the reconstructed diamond (100) surface", The Journal of Physical Chemistry **97**, 23–28 (1993).

[42]M. Kamo, Y. Sato, S. Matsumoto, and N. Setaka, "Diamond synthesis from gas phase in microwave plasma", Journal of Crystal Growth **62**, 642–644 (1983).

[43]Y. Mokuno, A. Chayahara, Y. Soda, Y. Horino, and N. Fujimori, "Synthesizing single-crystal diamond by repetition of high rate homoepitaxial growth by microwave plasma CVD", Diamond and Related Materials, Proceedings of the 10th International Conference on New Diamond Science and Technology (ICNDST-10) **14**, 1743–1746 (2005).

[44]X. Li, J. Perkins, R. Collazo, R. J. Nemanich, and Z. Sitar, "Investigation of the effect of the total pressure and methane concentration on the growth rate and quality of diamond thin films grown by MPCVD", Diamond and Related Materials, Proceedings of the Joint 11th International Conference on New Diamond Science and Technology and the 9th Applied Diamond Conference 2006 **15**, 1784–1788 (2006).

[45]A. L. Vikharev, M. A. Lobaev, A. M. Gorbachev, D. B. Radishev, V. A. Isaev, and S. A. Bogdanov, "Investigation of homoepitaxial growth by microwave plasma CVD providing high growth rate and high quality of diamond simultaneously", Materials Today Communications **22**, 100816 (2020).

[46]H. Yamada, A. Chayahara, and Y. Mokuno, "Method to increase the thickness and quality of diamond layers using plasma chemical vapor deposition under (H, C, N, O) system", Diamond and Related Materials **101**, 107652 (2020).

[47]C. Wild, R. Kohl, N. Herres, W. Müller-Sebert, and P. Koidl, "Oriented CVD diamond films: twin formation, structure and morphology", Diamond and Related Materials, Proceedings of the 4th European Conference on Diamond, Diamond-like and Related Materials **3**, 373–381 (1994).

[48]F. Silva, X. Bonnin, J. Achard, O. Brinza, A. Michau, and A. Gicquel, "Geometric modeling of homoepitaxial CVD diamond growth: I. The {100}{111}{110}{113} system", Journal of Crystal Growth **310**, 187–203 (2008).

[49]F. Silva, J. Achard, X. Bonnin, A. Michau, A. Tallaire, O. Brinza, and A. Gicquel, "3D crystal growth model for understanding the role of plasma pre-treatment on CVD diamond crystal shape", physica status solidi (a) **203**, 3049–3055 (2006).

[50]A. Tallaire, J. Achard, F. Silva, O. Brinza, and A. Gicquel, "Growth of large size diamond single crystals by plasma assisted chemical vapour deposition: Recent achievements and remaining challenges", Comptes Rendus Physique, Crystal Growth / Croissance Cristalline **14**, 169–184 (2013).

[51]C. J. Widmann, W. Müller-Sebert, N. Lang, and C. E. Nebel, "Homoepitaxial growth of single crystalline CVD-diamond", Diamond and Related Materials **64**, 1–7 (2016).

[52]R. A. Khmelnitskiy, "Prospects for the synthesis of large single-crystal diamonds", Physics-Uspekhi **58**, 134 (2015).

[53]J. Maes, K. Iakoubovskii, M. Hayne, A. Stesmans, and V. V. Moshchalkov, "Diamond as a magnetic field calibration probe", Journal of Physics D: Applied Physics **37**, 1102–1106 (2004).

[54]O. Brinza, J. Achard, F. Silva, X. Bonnin, P. Barroy, K. D. Corte, and A. Gicquel, "Dependence of CVD diamond growth rate on substrate orientation as a function of process parameters in the high microwave power density regime", physica status solidi (a) **205**, 2114–2120 (2008).

[55]A. Charris, "Toward the rapid growth of high-quality, polycrystalline rimless, and large area single crystal diamond substrates" (Michigan State University, 2017).

[56]N. Lee and A. Badzian, "A study on surface morphologies of (001) homoepitaxial diamond films", Diamond and Related Materials **6**, 130–145 (1997).

[57]A. Tallaire, J. Achard, F. Silva, R. S. Sussmann, A. Gicquel, and E. Rzepka, "Oxygen plasma pretreatments for high quality homoepitaxial CVD diamond deposition", physica status solidi (a) **201**, 2419–2424 (2004).

[58]A. Tallaire, V. Mille, O. Brinza, T. N. Tran Thi, J. M. Brom, Y. Loguinov, A. Katrusha, A. Koliadin, and J. Achard, "Thick CVD diamond films grown on high-quality type IIa HPHT diamond substrates from New Diamond Technology", Diamond and Related Materials **77**, 146–152 (2017).

[59]J. Achard, V. Jacques, and A. Tallaire, "Chemical vapour deposition diamond single crystals with nitrogen-vacancy centres: a review of material synthesis and technology for quantum sensing applications", Journal of Physics D: Applied Physics **53**, 313001 (2020).

[60]E. V. Bushuev, V. Y. Yurov, A. P. Bolshakov, V. G. Ralchenko, E. E. Ashkinazi, A. V. Ryabova, I. A. Antonova, P. V. Volkov, A. V. Goryunov, and A. Y. Luk'yanov, "Synthesis of single crystal diamond by microwave plasma assisted chemical vapor deposition with in situ low-coherence interferometric control of growth rate", Diamond and Related Materials **66**, 83–89 (2016).

[61]M. Yuasa, O. Arakaki, J. S. Ma, A. Hiraki, and H. Kawarada, "Low temperature diamond film fabrication using magneto-active plasma CVD", Diamond and Related Materials **1**, 168–174 (1992).

[62]C.-s. Yan, Y. K. Vohra, H.-k. Mao, and R. J. Hemley, "Very high growth rate chemical vapor deposition of single-crystal diamond", Proceedings of the National Academy of Sciences of the United States of America **99**, 12523–12525 (2002).

[63]J. Asmussen and D. Reinhard, *Diamond films handbook* (CRC Press, 2002).

[64]J. Lu, Y. Gu, T. A. Grotjohn, T. Schuelke, and J. Asmussen, "Experimentally defining the safe and efficient, high pressure microwave plasma assisted CVD operating regime for single crystal diamond synthesis", Diamond and Related Materials **37**, 17–28 (2013).

[65]Y. Mokuno, A. Chayahara, Y. Soda, H. Yamada, Y. Horino, and N. Fujimori, "High rate homoepitaxial growth of diamond by microwave plasma CVD with nitrogen addition", Diamond and Related Materials, Diamond 2005 **15**, 455–459 (2006).

[66]T. Teraji, "Chemical vapor deposition of homoepitaxial diamond films", physica status solidi (a) **203**, 3324–3357 (2006).

[67]T. Teraji and T. Ito, "Homoepitaxial diamond growth by high-power microwave-plasma chemical vapor deposition", Journal of Crystal Growth **271**, 409–419 (2004).

[68]Y.-f. Meng, C.-s. Yan, S. Krasnicki, Q. Liang, J. Lai, H. Shu, T. Yu, A. Steele, H.-k. Mao, and R. J. Hemley, "High optical quality multicarat single crystal diamond produced by chemical vapor deposition", physica status solidi (a) **209**, 101–104 (2012).

[69]M. Muehle, J. Asmussen, M. F. Becker, and T. Schuelke, "Extending microwave plasma assisted CVD SCD growth to pressures of 400Torr", Diamond and Related Materials **79**, 150–163 (2017).

[70]V. Ralchenko, I. Sychov, I. Vlasov, A. Vlasov, V. Konov, A. Khomich, and S. Voronina, "Quality of diamond wafers grown by microwave plasma CVD: effects of gas flow rate", Diamond and Related Materials **8**, 189–193 (1999).

[71]J. Su, Y. Li, Y. Liu, M. Ding, and W. Tang, "Revisiting the gas flow rate effect on diamond films deposition with a new dome-shaped cavity type microwave plasma CVD reactor", Diamond and Related Materials, 10th International Conference on New Diamond and Nano Carbons – NDNC 2016 **73**, 99–104 (2017).

[72]F. G. Celii, D. White, and A. J. Purdes, "Deposition of smooth, oriented diamond films using microwave plasma chemical vapor deposition", Thin Solid Films, Special Issue: Diamond Films and Related Materials **212**, 140–149 (1992).

[73]A. Tallaire, A. T. Collins, D. Charles, J. Achard, R. Sussmann, A. Gicquel, M. E. Newton, A. M. Edmonds, and R. J. Cruddace, "Characterisation of high-quality thick single-crystal diamond grown by CVD with a low nitrogen addition", Diamond and Related Materials **15**, 1700–1707 (2006).

[74]H. Yamada, A. Chayahara, and Y. Mokuno, "Effects of intentionally introduced nitrogen and substrate temperature on growth of diamond bulk single crystals", Japanese Journal of Applied Physics **55**, 01AC07 (2015).

[75]G. A. Scarsbrook, P. M. Martineau, B. S. C. Dorn, M. A. Cooper, J. L. Collins, A. J. Whitehead, D. J. Twitchen, and R. S. Sussman, "Thick single crystal diamond layer method for making it and gemstones produced from the layer", U.S. pat. 7887628B2 (Element Six Technologies Pty Ltd, Feb. 15, 2011).

[76]J. Achard, F. Silva, A. Tallaire, X. Bonnin, G. Lombardi, K. Hassouni, and A. Gicquel, "High quality MPACVD diamond single crystal growth: high microwave power density regime", Journal of Physics D: Applied Physics **40**, 6175–6188 (2007).

[77]P. K. Bachmann, D. Leers, and H. Lydtin, "Towards a general concept of diamond chemical vapour deposition", Diamond and Related Materials **1**, 1–12 (1991).

[78]Y. Liou, A. Inspektor, R. Weimer, D. Knight, and R. Messier, "The effect of oxygen in diamond deposition by microwave plasma enhanced chemical vapor deposition", Journal of Materials Research **5**, 2305–2312 (1990).

[79]T. Kawato and K.-i. Kondo, "Effects of Oxygen on CVD Diamond Synthesis", Japanese Journal of Applied Physics **26**, 1429 (1987).

[80]J. J. Gracio, Q. H. Fan, and J. C. Madaleno, "Diamond growth by chemical vapour deposition", Journal of Physics D: Applied Physics **43**, 374017 (2010).

[81]T. Teraji, "High-quality and high-purity homoepitaxial diamond (100) film growth under high oxygen concentration condition", Journal of Applied Physics **118**, 115304 (2015).

[82]R. Issaoui, J. Achard, F. Silva, A. Tallaire, V. Mille, and A. Gicquel, "Influence of oxygen addition on the crystal shape of CVD boron doped diamond", physica status solidi (a) **208**, 2023–2027 (2011).

[83]M. A. Lobaev, S. A. Bogdanov, D. B. Radishev, A. L. Vikharev, and A. M. Gorbachev, "Method of power density determination in microwave discharge, sustained in hydrogen–methane gas mixture", Diamond and Related Materials **66**, 177–182 (2016).

[84]H. Yamada, A. Chayahara, Y. Mokuno, Y. Horino, and S. Shikata, "Simulation of microwave plasmas concentrated on the top surface of a diamond substrate with finite thickness", Diamond and Related Materials **15**, 1383–1388 (2006).

[85]S. Nad, Y. Gu, and J. Asmussen, "Growth strategies for large and high quality single crystal diamond substrates", Diamond and Related Materials **60**, 26–34 (2015).

[86]G. Wu, M. .-. Chen, and J. Liao, "The influence of recess depth and crystallographic orientation of seed sides on homoepitaxial growth of CVD single crystal diamonds", Diamond and Related Materials, Special Issue "26th International Conference on Diamond and Carbon Materials – DCM 2015" **65**, 144–151 (2016).

[87]A. Charris, S. Nad, and J. Asmussen, "Exploring constant substrate temperature and constant high pressure SCD growth using variable pocket holder depths", Diamond and Related Materials **76**, 58–67 (2017).

[88]K. W. Hemawan and R. J. Hemley, "Optical emission diagnostics of plasmas in chemical vapor deposition of single-crystal diamond", Journal of Vacuum Science & Technology A **33**, 061302 (2015).

[89]S. Abdelli-Messaci, T. Kerdja, A. Bendib, and S. Malek, "CN emission spectroscopy study of carbon plasma in nitrogen environment", Spectrochimica Acta Part B: Atomic Spectroscopy, Laser Induced Plasma Spectroscopy and Applications (LIBS 2004) Third International Conference **60**, 955–959 (2005).

[90]C.-S. Yan and Y. K. Vohra, "Multiple twinning and nitrogen defect center in chemical vapor deposited homoepitaxial diamond", Diamond and Related Materials **8**, 2022–2031 (1999).

[91]T. Vandevelde, M. Nesladek, C. Quaeyhaegens, and L. Stals, "Optical emission spectroscopy of the plasma during CVD diamond growth with nitrogen addition", Thin Solid Films, Papers Presented at the 23rd International Conference on Metallurgical Coatings and Thin Films **290–291**, 143–147 (1996).

[92]V. Y. Yurov, E. E. Ashkinazi, E. V. Zavedeev, A. K. Martyanov, I. A. Antonova, and V. G. Ralchenko, "Optical diagnostics of microwave plasma in process of micro/nanocrystalline diamond deposition on hard alloy tools", Materials Today: Proceedings, International Conference on Modern Trends in Manufacturing Technologies and Equipment 2020 (ICMTMTE 2020) **38**, 1736–1739 (2021).

[93]G. Bradski, "The OpenCV library", Dr. Dobb's Journal of Software Tools (2000).

[94]M. L. Huber and A. H. Harvey, "Thermal conductivity of gases", CRC Handbook of Chemistry and Physics **92** (2011).

[95]A. Purohit and A. A. Purohit, "Process for refining diamonds", U.S. pat. 5133792A (Anshal Inc, July 28, 1992).

[96]S. J. Cobb, F. H. J. Laidlaw, G. West, G. Wood, M. E. Newton, R. Beanland, and J. V. Macpherson, "Assessment of acid and thermal oxidation treatments for removing sp2 bonded carbon from the surface of boron doped diamond", Carbon **167**, 1–10 (2020).

[97]K. J. Brown, E. Chartier, E. M. Sweet, D. A. Hopper, and L. C. Bassett, "Cleaning diamond surfaces using boiling acid treatment in a standard laboratory chemical hood", Journal of Chemical Health & Safety **26**, 40–44 (2019).

[98]O. A. Kozmenko, S. V. Chigrin, and V. G. Vins, "Diamond cleaning method", pat. WO2008123801A1 (WO) ('new Diamonds Of Siberia, Ltd.', Oct. 16, 2008).

[99]B. H. Stuart, *Infrared spectroscopy: fundamentals and applications* (John Wiley & Sons, 2004).

[100]E. Roueff, H. Abgrall, P. Czachorowski, K. Pachucki, M. Puchalski, and J. Komasa, "The full infrared spectrum of molecular hydrogen", Astronomy & Astrophysics **630**, A58 (2019).

[101]A. M. Zaitsev, *Optical Properties of Diamond: A Data Handbook* (Springer-Verlag, Berlin Heidelberg, 2001).

[102]"4 - Key technologies for device fabrications and materials characterizations", in *Power Electronics Device Applications of Diamond Semiconductors*, edited by S. Koizumi, H. Umezawa, J. Pernot, and M. Suzuki, Woodhead Publishing Series in Electronic and Optical Materials (Woodhead Publishing, Jan. 1, 2018), pp. 219–294.

[103]C. Liu and R. W. Berg, "Determining the Spectral Resolution of a Charge-Coupled Device (CCD) Raman Instrument", Applied Spectroscopy **66**, 1034–1043 (2012).

[104]T. Váczi, "A New, Simple Approximation for the Deconvolution of Instrumental Broadening in Spectroscopic Band Profiles", Applied Spectroscopy **68**, 1274–1278 (2014).

[105]N. V. Surovtsev and I. N. Kupriyanov, "Temperature dependence of the Raman line width in diamond: Revisited", Journal of Raman Spectroscopy **46**, 171–176 (2015).

[106]G. R. Eaton, S. S. Eaton, D. P. Barr, and R. T. Weber, *Quantitative EPR* (Springer Vienna, Vienna, 2010).

[107]S. Stoll and A. Schweiger, "EasySpin, a comprehensive software package for spectral simulation and analysis in EPR", Journal of Magnetic Resonance **178**, 42–55 (2006).

[108]A. M. Edmonds, M. E. Newton, P. M. Martineau, D. J. Twitchen, and S. D. Williams, "Electron paramagnetic resonance studies of silicon-related defects in diamond", Physical Review B **77**, 245205 (2008).

[109]S. Liggins, "Identification of point defects in treated single crystal diamond", PhD thesis (University of Warwick, Sept. 2010).

[110]T. Bauer, M. Schreck, J. Härtwig, X. H. Liu, S. P. Wong, and B. Stritzker, "Structural defects in homoepitaxial diamond layers grown on off-axis Ib HPHT substrates", physica status solidi (a) **203**, 3056–3062 (2006).

[111]I. A. Dobrinets, *HPHT-Treated Diamonds : Diamonds Forever*, Springer Series in Materials Science (Springer, Berlin, 2013).

[112]I. Friel, S. L. Clewes, H. K. Dhillon, N. Perkins, D. J. Twitchen, and G. A. Scarsbrook, "Control of surface and bulk crystalline quality in single crystal diamond grown by chemical vapour deposition", Diamond and Related Materials, Proceedings of Diamond 2008, the 19th European Conference on Diamond, Diamond-Like Materials, Carbon Nanotubes, Nitrides and Silicon Carbide **18**, 808–815 (2009).

[113]Y. Mokuno, Y. Kato, N. Tsubouchi, A. Chayahara, H. Yamada, and S. Shikata, "A nitrogen doped low-dislocation density free-standing single crystal diamond plate fabricated by a lift-off process", Applied Physics Letters **104**, 252109 (2014).

[114]L. Tolstoy, *Anna Karenina*, trans. by R. Bartlett, 2nd ed., Oxford World's Classics (Oxford University Press, New York, NY, 2016), 847 pp.

[115]G. S. Woods, J. A. V. Wyk, and A. T. Collins, "The nitrogen content of type Ib synthetic diamond", Philosophical Magazine B **62**, 589–595 (1990).

[116]J. H. N. Loubser and J. A. van Wyk, "Electron spin resonance in the study of diamond", Reports on Progress in Physics **41**, 1201–1248 (1978).

[117]R. Chapman and T. Plakhotnik, "Quantitative luminescence microscopy on Nitrogen-Vacancy Centres in diamond: Saturation effects under pulsed excitation", Chemical Physics Letters **507**, 190–194 (2011).

[118]C. Santori, P. E. Barclay, K.-M. C. Fu, and R. G. Beausoleil, "Vertical distribution of nitrogen-vacancy centers in diamond formed by ion implantation and annealing", Physical Review B **79**, 125313 (2009).

[119]M. S. Barson, E. Krausz, N. B. Manson, and M. W. Doherty, "The fine structure of the neutral nitrogen-vacancy center in diamond", Nanophotonics **8**, 1985–1991 (2019).

[120]V. Y. Osipov, F. Treussart, S. A. Zargaleh, K. Takai, F. M. Shakhov, B. T. Hogan, and A. Baldycheva, "Photoluminescence from NV- Centres in 5 nm Detonation Nanodiamonds: Identification and High Sensitivity to Magnetic Field", Nanoscale Research Letters **14**, 279 (2019).

[121]G. A. Scarsbrook, P. M. Martineau, and D. J. Twitchen, "Single crystal diamond", U.S. pat. 9816202B2 (Element Six Technologies Ltd, Nov. 14, 2017).

[122]Wang, Duan, Cao, Liu, Wang, Peng, and Hu, "Homoepitaxy Growth of Single Crystal Diamond under 300 torr Pressure in the MPCVD System", Materials **12**, 3953 (2019).

[123]Q. Liang, C. Y. Chin, J. Lai, C.-s. Yan, Y. Meng, H.-k. Mao, and R. J. Hemley, "Enhanced growth of high quality single crystal diamond by microwave plasma assisted chemical vapor deposition at high gas pressures", Applied Physics Letters **94**, 024103 (2009).

[124]Y. Zhao, Y. Guo, L. Lin, Y. Zheng, L. Hei, J. Liu, J. Wei, L. Chen, and C. Li, "Relationship between Birefringence and Surface Morphology in Single-Crystal Diamonds Grown by MPCVD", Crystal Research and Technology **53**, 1800055 (2018).

[125]T. Bauer, M. Schreck, and B. Stritzker, "Homoepitaxial diamond layers on off-axis Ib HPHT substrates: Growth of thick films and characterisation by high-resolution X-ray diffraction", Diamond and Related Materials, Diamond 2005 **15**, 472–478 (2006).

[126]T. Bauer, M. Schreck, H. Sternschulte, and B. Stritzker, "High growth rate homoepitaxial diamond deposition on off-axis substrates", Diamond and Related Materials, Proceedings of Diamond 2004, the 15th European Conference on Diamond, Diamond-Like Materials, Carbon Nanotubes, Nitrides and Silicon Carbide **14**, 266–271 (2005).

[127]D. Kirillov and G. J. Reynolds, "Linewidths of phonon lines of natural and synthetic diamonds", Applied Physics Letters **65**, 1641–1643 (1994).

[128]S. C. Lawson, D. Fisher, D. C. Hunt, and M. E. Newton, "On the existence of positively charged single-substitutional nitrogen in diamond", Journal of Physics: Condensed Matter **10**, 6171–6180 (1998).

[129]D. Howell, C. O'Neill, K. Grant, W. Griffin, N. Pearson, and S. O'Reilly, "μ-FTIR mapping: Distribution of impurities in different types of diamond growth", Diamond and Related Materials **29**, 29–36 (2012).

[130]K. M. McNamara, B. E. Williams, K. K. Gleason, and B. E. Scruggs, "Identification of defects and impurities in chemical-vapor-deposited diamond through infrared spectroscopy", Journal of Applied Physics **76**, 2466–2472 (1994).

[131]B. L. Cann, "Magnetic resonance studies of point defects in diamond" (University of Warwick, July 2009).

[132]C. D. Clark, H. Kanda, I. Kiflawi, and G. Sittas, "Silicon defects in diamond", Physical Review B **51**, 16681–16688 (1995).

[133]E. Neu, D. Steinmetz, J. Riedrich-Möller, S. Gsell, M. Fischer, M. Schreck, and C. Becher, "Single photon emission from silicon-vacancy colour centres in chemical vapour deposition nano-diamonds on iridium", New Journal of Physics **13**, 025012 (2011).

[134]U. F. S. D'Haenens-Johansson, A. M. Edmonds, B. L. Green, M. E. Newton, G. Davies, P. M. Martineau, R. U. A. Khan, and D. J. Twitchen, "Optical properties of the neutral silicon split-vacancy center in diamond", Physical Review B **84**, 245208 (2011).

[135]E. Neu, C. Hepp, M. Hauschild, S. Gsell, M. Fischer, H. Sternschulte, D. Steinmüller-Nethl, M. Schreck, and C. Becher, "Low-temperature investigations of single silicon vacancy colour centres in diamond", New Journal of Physics **15**, 043005 (2013).

[136]C. Hepp, "Electronic structure of the silicon vacancy color center in diamond" (Universität Des Saarlandes, 2014).

[137]T. Müller, C. Hepp, B. Pingault, E. Neu, S. Gsell, M. Schreck, H. Sternschulte, D. Steinmüller-Nethl, C. Becher, and M. Atatüre, "Optical signatures of silicon-vacancy spins in diamond", Nature Communications **5**, 3328 (2014).

[138]K. D. Jahnke, A. Sipahigil, J. M. Binder, M. W. Doherty, M. Metsch, L. J. Rogers, N. B. Manson, M. D. Lukin, and F. Jelezko, "Electron–phonon processes of the silicon-vacancy centre in diamond", New Journal of Physics **17**, 043011 (2015).

[139]S. A. Grudinkin, N. A. Feoktistov, M. A. Baranov, A. N. Smirnov, V. Y. Davydov, and V. G. Golubev, "Low-strain heteroepitaxial nanodiamonds: fabrication and photoluminescence of silicon-vacancy colour centres", Nanotechnology **27**, 395606 (2016).

[140]J. N. Becker and E. Neu, "Chapter Seven - The silicon vacancy center in diamond", in *Semiconductors and Semimetals*, Vol. 103, edited by C. E. Nebel, I. Aharonovich, N. Mizuochi, and M. Hatano, Diamond for Quantum Applications Part 1 (Elsevier, Jan. 1, 2020), pp. 201–235.

[141]T. Iwasaki, F. Ishibashi, Y. Miyamoto, Y. Doi, S. Kobayashi, T. Miyazaki, K. Tahara, K. D. Jahnke, L. J. Rogers, B. Naydenov, F. Jelezko, S. Yamasaki, S. Nagamachi, T. Inubushi, N. Mizuochi, and M. Hatano, "Germanium-Vacancy Single Color Centers in Diamond", Scientific Reports **5**, 12882 (2015).

[142]S. D. Tchernij, T. Herzig, J. Forneris, J. Kupper, S. Pezzagna, P. Traina, E. Moreva, I. P. Degiovanni, G. Brida, N. Skukan, M. Genovese, M. Jakšić, J. Meijer, and P. Olivero, "Single-Photon-Emitting Optical Centers in Diamond Fabricated upon Sn Implantation", ACS Photonics **4**, 2580–2586 (2017).

[143]S. Ditalia Tchernij, T. Lühmann, T. Herzig, J. Küpper, A. Damin, S. Santonocito, M. Signorile, P. Traina, E. Moreva, F. Celegato, S. Pezzagna, I. P. Degiovanni, P. Olivero, M. Jakšić, J. Meijer, P. M. Genovese, and J. Forneris, "Single-Photon Emitters in Lead-Implanted Single-Crystal Diamond", ACS Photonics **5**, 4864–4871 (2018).

[144]G. Thiering and A. Gali, "Chapter One - Color centers in diamond for quantum applications", in *Semiconductors and Semimetals*, Vol. 103, edited by C. E. Nebel, I. Aharonovich, N. Mizuochi, and M. Hatano, Diamond for Quantum Applications Part 1 (Elsevier, Jan. 1, 2020), pp. 1–36.

[145]B. Machielse, S. Bogdanovic, S. Meesala, S. Gauthier, M. J. Burek, G. Joe, M. Chalupnik, Y. I. Sohn, J. Holzgrafe, R. E. Evans, C. Chia, H. Atikian, M. K. Bhaskar, D. D. Sukachev, L. Shao, S. Maity, M. D. Lukin, and M. Lončar, "Quantum Interference of Electromechanically Stabilized Emitters in Nanophotonic Devices", Physical Review X **9**, 031022 (2019).

[146]L. J. Rogers, K. D. Jahnke, T. Teraji, L. Marseglia, C. Müller, B. Naydenov, H. Schauffert, C. Kranz, J. Isoya, L. P. McGuinness, and F. Jelezko, "Multiple intrinsically identical single-photon emitters in the solid state", Nature Communications **5**, 4739 (2014).

[147]S. Lyapin, I. Ilichev, A. Novikov, V. Davydov, and V. Agafonov, "Study of optical properties of the NV and SiV centres in diamond at high pressures", Nanosystems: Physics, Chemistry, Mathematics, 55–57 (2018).

[148]S. Meesala, Y.-I. Sohn, B. Pingault, L. Shao, H. A. Atikian, J. Holzgrafe, M. Gundogan, C. Stavrakas, A. Sipahigil, C. Chia, M. J. Burek, M. Zhang, L. Wu, J. L. Pacheco, J. Abraham, E. Bielejec, M. D. Lukin, M. Atature, and M. Loncar, "Strain engineering of the silicon-vacancy center in diamond", Physical Review B **97**, 205444 (2018).

[149]E. A. Ekimov, P. S. Sherin, V. S. Krivobok, S. G. Lyapin, V. A. Gavva, and M. V. Kondrin, "Photoluminescence excitation study of split-vacancy centers in diamond", Physical Review B **97**, 045206 (2018).

[150]E. A. Ekimov, S. G. Lyapin, A. A. Razgulov, and M. V. Kondrin, "Ab initio Calculation of Impurity–Vacancy Complexes in Diamond at High Pressure", Journal of Experimental and Theoretical Physics **129**, 855–862 (2019).

[151]C. Bradac, W. Gao, J. Forneris, M. E. Trusheim, and I. Aharonovich, "Quantum nanophotonics with group IV defects in diamond", Nature Communications **10**, 5625 (2019).

[152]B. C. Rose, D. Huang, Z.-H. Zhang, A. M. Tyryshkin, S. Sangtawesin, S. Srinivasan, L. Loudin, M. L. Markham, A. M. Edmonds, D. J. Twitchen, S. A. Lyon, and N. P. de Leon, "Observation of an environmentally insensitive solid state spin defect in diamond", Science **361**, 60–63 (2018).

[153]Z.-H. Zhang, P. Stevenson, G. Thiering, B. C. Rose, D. Huang, A. M. Edmonds, M. L. Markham, S. A. Lyon, A. Gali, and N. P. de Leon, "Optically Detected Magnetic Resonance in Neutral Silicon Vacancy Centers in Diamond via Bound Exciton States", Physical Review Letters **125**, 237402 (2020).

[154]B. L. Green, M. W. Doherty, E. Nako, N. B. Manson, U. F. S. D'Haenens-Johansson, S. D. Williams, D. J. Twitchen, and M. E. Newton, "Electronic structure of the neutral silicon-vacancy center in diamond", Physical Review B **99**, 161112 (2019).

[155]C. M. Breeding and W. Wang, "Occurrence of the Si–V defect center in natural colorless gem diamonds", Diamond and Related Materials **17**, 1335–1344 (2008).

[156]C. D. Clark and C. B. Dickerson, "The 1.681 eV centre in polycrystalline diamond", Surface and Coatings Technology **47**, 336–343 (1991).

[157]J. Barjon, E. Rzepka, F. Jomard, J.-M. Laroche, D. Ballutaud, T. Kociniewski, and J. Chevallier, "Silicon incorporation in CVD diamond layers", physica status solidi (a) **202**, 2177–2181 (2005).

[158]A. Bolshakov, V. Ralchenko, V. Sedov, A. Khomich, I. Vlasov, A. Khomich, N. Trofimov, V. Krivobok, S. Nikolaev, R. Khmelnitskii, and V. Saraykin, "Photoluminescence of SiV centers in single crystal CVD diamond in situ doped with Si from silane", physica status solidi (a) **212**, 2525–2532 (2015).

[159]T. Feng and B. D. Schwartz, "Characteristics and origin of the 1.681 eV luminescence center in chemical-vapor-deposited diamond films", Journal of Applied Physics **73**, 1415–1425 (1993).

[160]M. Zaghrioui, V. N. Agafonov, and V. A. Davydov, "Nitrogen and group-IV (Si, Ge) vacancy color centres in nano-diamonds: photoluminescence study at high temperature (25 °C–600 °C)", Materials Research Express **7**, 015043 (2020).

[161]S. Lagomarsino, F. Gorelli, M. Santoro, N. Fabbri, A. Hajeb, S. Sciortino, L. Palla, C. Czelusniak, M. Massi, F. Taccetti, L. Giuntini, N. Gelli, D. Y. Fedyanin, F. S. Cataliotti, C. Toninelli, and M. Agio, "Robust luminescence of the silicon-vacancy center in diamond at high temperatures", AIP Advances **5**, 127117 (2015).

[162]M. Kobayashi and Y. Nisida, "High Pressure Effects on Photoluminescence Spectra of Color Centers in Diamond", Japanese Journal of Applied Physics **32**, 279 (1993).

[163]M. W. Doherty, V. V. Struzhkin, D. A. Simpson, L. P. McGuinness, Y. Meng, A. Stacey, T. J. Karle, R. J. Hemley, N. B. Manson, L. C. L. Hollenberg, and S. Prawer, "Electronic Properties and Metrology Applications of the Diamond NV- Center under Pressure", Physical Review Letters **112**, 047601 (2014).

[164]B. Deng, R. Q. Zhang, and X. Q. Shi, "New insight into the spin-conserving excitation of the negatively charged nitrogen-vacancy center in diamond", Scientific Reports **4**, 5144 (2014).

[165]V. Ivády, T. Simon, J. R. Maze, I. A. Abrikosov, and A. Gali, "Pressure and temperature dependence of the zero-field splitting in the ground state of NV centers in diamond: A first-principles study", Physical Review B **90**, 235205 (2014).

[166]K. O. Ho, M. Y. Leung, Y. Jiang, K. P. Ao, W. Zhang, K. Y. Yip, Y. Y. Pang, K. C. Wong, S. K. Goh, and S. Yang, "Probing Local Pressure Environment in Anvil Cells with Nitrogen-Vacancy (NV-) Centers in Diamond", Physical Review Applied **13**, 024041 (2020).

[167]A. A. Razgulov, S. G. Lyapin, A. P. Novikov, and E. A. Ekimov, "Low-temperature photoluminescence study of SnV centers in HPHT diamond", Diamond and Related Materials **116**, 108379 (2021).

[168]A. A. Razgulov, S. G. Lyapin, A. P. Novikov, and E. A. Ekimov, "Low-temperature photoluminescence study of GeV centres in HPHT diamond", Journal of Luminescence **242**, 118556 (2022).

[169]A. Dietrich, K. D. Jahnke, J. M. Binder, T. Teraji, J. Isoya, L. J. Rogers, and F. Jelezko, "Isotopically varying spectral features of silicon-vacancy in diamond", New Journal of Physics **16**, 113019 (2014).

[170]H. Sternschulte, K. Thonke, R. Sauer, P. C. Münzinger, and P. Michler, "1.681-eV luminescence center in chemical-vapor-deposited homoepitaxial diamond films", Physical Review B **50**, 14554–14560 (1994).

[171]H. Sternschulte, K. Thonke, J. Gerster, W. Limmer, R. Sauer, J. Spitzer, and P. C. Münzinger, "Uniaxial stress and Zeeman splitting of the 1.681 eV optical center in a homoepitaxial CVD diamond film", Diamond and Related Materials **4**, 1189–1192 (1995).

[172]Y.-I. Sohn, S. Meesala, B. Pingault, H. A. Atikian, J. Holzgrafe, M. Gündoğan, C. Stavrakas, M. J. Stanley, A. Sipahigil, J. Choi, M. Zhang, J. L. Pacheco, J. Abraham, E. Bielejec, M. D. Lukin, M. Atatüre, and M. Lončar, "Controlling the coherence of a diamond spin qubit through its strain environment", Nature Communications **9**, 2012 (2018).

[173]S. Klotz, J.-C. Chervin, P. Munsch, and G. Le Marchand, "Hydrostatic limits of 11 pressure transmitting media", Journal of Physics D: Applied Physics **42**, 075413 (2009).

[174]A. Celeste, F. Borondics, and F. Capitani, "Hydrostaticity of pressure-transmitting media for high pressure infrared spectroscopy", High Pressure Research **39**, 608–618 (2019).

[175]N. Tateiwa and Y. Haga, "Appropriate pressure-transmitting media for cryogenic experiment in the diamond anvil cell up to 10 GPa", **215**, 012178 (2010).

[176]"Nitrogen Phase Change Data", in *NIST Chemistry WebBook, NIST Standard Reference Database Number 69*, edited by P. Linstrom and W. Mallard, Thermodynamics Source Database (National Institute of Standards and Technology, Gaithersburg MD, 2022).

[177]M. Rivers, V. B. Prakapenka, A. Kubo, C. Pullins, C. M. Holl, and S. D. Jacobsen, "The COMPRES / GSECARS gas-loading system for diamond anvil cells at the Advanced Photon Source", High Pressure Research **28**, 273–292 (2008).

[178]A. Dewaele, M. Torrent, P. Loubeyre, and M. Mezouar, "Compression curves of transition metals in the Mbar range: Experiments and projector augmented-wave calculations", Physical Review B **78**, 104102 (2008).

[179]D. E. McCumber and M. D. Sturge, "Linewidth and Temperature Shift of the R Lines in Ruby", Journal of Applied Physics **34**, 1682–1684 (1963).

[180]B. A. Weinstein, "Ruby thermometer for cryobaric diamond-anvil cell", Review of Scientific Instruments **57**, 910–913 (1986).

[181]Bernold Richerzhagen, Muneharu Kutsuna, Haruhiku Okada, and Takeshi Ikeda, "Water-jet-guided laser processing", in , Vol. 4830 (Feb. 19, 2003).

[182]H. Hirai, H. Hidai, S. Matsusaka, A. Chiba, Y. Mokuno, M. Yamaguchi, and N. Morita, "Diamond slicing using ultrashort laser-induced graphitization and additional nanosecond laser illumination", Diamond and Related Materials **96**, 126–133 (2019).

[183]B. Yang, J. Li, L. Guo, N. Huang, L. Liu, Z. Zhai, W. Long, and X. Jiang, "Fabrication of silicon-vacancy color centers in diamond films: tetramethylsilane as a new dopant source", CrystEngComm **20**, 1158–1167 (2018).

[184]S. Choi, V. N. Agafonov, V. A. Davydov, and T. Plakhotnik, "Ultrasensitive All-Optical Thermometry Using Nanodiamonds with a High Concentration of Silicon-Vacancy Centers and Multiparametric Data Analysis", ACS Photonics **6**, 1387–1392 (2019).

[185]K. D. Jahnke, "Low temperature spectroscopy of single colour centres in diamond - the silicon-vacancy centre in diamond" (Universität Ulm, 2015).

[186]K. Dragounová, Z. Potůček, Š. Potocký, Z. Bryknar, and A. Kromka, "Determination of temperature dependent parameters of zero-phonon line in photo-luminescence spectrum of silicon-vacancy centre in CVD diamond thin films", Journal of Electrical Engineering **68**, 74–78 (2017).

[187]Y. Feng, R. Jaramillo, J. Wang, Y. Ren, and T. F. Rosenbaum, "Invited Article: High-pressure techniques for condensed matter physics at low temperature", Review of Scientific Instruments **81**, 041301 (2010).

[188]N. Tateiwa and Y. Haga, "Evaluations of pressure-transmitting media for cryogenic experiments with diamond anvil cell", Review of Scientific Instruments **80**, 123901 (2009).

[189]P. W. May and Y. A. Mankelevich, "From Ultrananocrystalline Diamond to Single Crystal Diamond Growth in Hot Filament and Microwave Plasma-Enhanced CVD Reactors: a Unified Model for Growth Rates and Grain Sizes", The Journal of Physical Chemistry C **112**, 12432–12441 (2008).

[190]M. Ficek, K. J. Sankaran, J. Ryl, R. Bogdanowicz, I.-N. Lin, K. Haenen, and K. Darowicki, "Ellipsometric investigation of nitrogen doped diamond thin films grown in microwave CH4/H2/N2 plasma enhanced chemical vapor deposition", Applied Physics Letters **108**, 241906 (2016).

[191]W. Wang, T. Moses, R. C. Linares, J. E. Shigley, M. Hall, and J. E. Butler, "Gem-Quality Synthetic Diamonds Grown by a Chemical Vapor Deposition (CVD) Method", Gems & Gemology **39**, 268–283 (2003).

[192]C. Arend, J. N. Becker, H. Sternschulte, D. Steinmüller-Nethl, and C. Becher, "Photoluminescence excitation and spectral hole burning spectroscopy of silicon vacancy centers in diamond", Physical Review B **94**, 045203 (2016).

[193]R. P. Mildren, "Intrinsic Optical Properties of Diamond", in *Optical Engineering of Diamond*, edited by R. P. Mildren and J. R. Rabeau (Wiley-VCH Verlag GmbH & Co. KGaA, Weinheim, Germany, Mar. 28, 2013), pp. 1–34.

[194]S. V. Nistor, M. Stefan, V. Ralchenko, A. Khomich, and D. Schoemaker, "Nitrogen and hydrogen in thick diamond films grown by microwave plasma enhanced chemical vapor deposition at variable H2 flow rates", Journal of Applied Physics **87**, 8741–8746 (2000).

[195]T. Hainschwang, E. Fritsch, L. Massi, B. Rondeau, and F. Notari, "The C center isolated nitrogen-related infrared absorption at 2688 cm–1: perfect harmony in diamond", Journal of Applied Spectroscopy **79**, 737–743 (2012).

[196]E. K. Neu, "Silicon vacancy color centers in chemical vapor deposition diamond : new insights into promising solid state single photon sources", PhD thesis (Saarland University, Saarbrucken, 2012), 196 pp.